

AN ABSTRACT OF THE DISSERTATION OF

Nicolai Thum for the degree of Doctor of Philosophy in Atmospheric Sciences
presented on September 13, 2006.

Title: Atmospheric Boundary Layer Coupling to Midlatitude
Mesoscale Sea Surface Temperature Anomalies

Abstract approved: _____

Steven K. Esbensen

This thesis examines the mechanisms that couple the monthly-averaged atmospheric boundary layer (ABL) to open-ocean sea surface temperature (SST) perturbations on scales of 50-500 km. The observed positive correlation between surface wind speed anomalies and SST anomalies is successfully simulated using the Weather Research and Forecasting (WRF) model.

In numerical experiments with idealized SST fronts, the cross-frontal surface wind acceleration in the cold-to-warm case and deceleration in the warm-to-cold case are found over narrow transition zones co-located with the narrow regions of large frontal SST changes. In the transition zone, horizontal momentum is redistributed vertically in the ABL by turbulence and convection. The largest pressure adjustments, on the other hand, take place over a much broader region downstream from the SST front. In the cold-to-warm transition zone the model simulates an unstable thermal internal boundary layer (TIBL) in the lower part of the ABL. As the TIBL grows, higher velocity air aloft is incorporated into the TIBL, accelerating the flow. Over the warm-to-cold transition zone, the

momentum boundary layer collapses, and vertical mixing of momentum by turbulence and convection ceases in the upper part of the ABL.

The WRF model is also applied to open-ocean ABL flow across idealized sinusoidal SST anomalies having scales similar to those observed in the Agulhas return current region. The simulated horizontal pressure gradient force anomalies are crucial to the response over the entire domain, and the vertically integrated momentum budget is found to be approximately linear. A linear diagnostic model is therefore developed which successfully predicts the observed phase and amplitude of the ABL wind, pressure and temperature response to the SST anomalies, with largest quantitative discrepancies found in the perturbation wind component perpendicular to the mean wind direction. By using the divergence and vorticity budgets, the diagnostic model shows that differences in the vertical structure of the perturbation wind components down and across the mean wind can explain the differences in the coupling coefficients for the divergence and curl as functions of downwind and crosswind SST gradients, and as functions of the angle between the SST gradient and the mean wind.

©Copyright by Nicolai Thum

September 13, 2006

All Rights Reserved

Atmospheric Boundary Layer Coupling to Midlatitude Mesoscale Sea Surface
Temperature Anomalies

by

Nicolai Thum

A DISSERTATION

submitted to

Oregon State University

in partial fulfillment of
the requirements for the
degree of

Doctor of Philosophy

Presented September 13, 2006
Commencement June 2007

Doctor of Philosophy dissertation of Nicolai Thum presented on
September 13, 2006

APPROVED:

Major Professor, representing Atmospheric Sciences

Dean of the College of Oceanic and Atmospheric Sciences

Dean of the Graduate School

I understand that my dissertation will become part of the permanent collection of Oregon State University libraries. My signature below authorizes release of my dissertation to any reader upon request.

Nicolai Thum, Author

ACKNOWLEDGMENT

Foremost, I would like to express my gratitude to my advisor Steve Esbensen for providing me the opportunity to become his student after I participated in an exchange program between Oregon State University and the University of Karlsruhe. His profound scientific knowledge, time for many meetings and discussions and editorial advice are invaluable for this dissertation.

I would like to thank Dudley Chelton for all his help and inspiring enthusiasm for the period of my graduate studies.

I also would like to acknowledge Eric Maloney for providing the aqua-planet boundary conditions, Eric Skyllingstad for granting access to the high-performance computing facilities and Larry O'Neill for providing QuikSCAT and AMSR satellite data and performing related calculations.

This material is based upon work supported by the National Science Foundation under Grand No. 0002322-ATM.

The non-scientific support was equally important during the time of this dissertation. I am grateful for my parents Margret and Herbert Thum for their love, trust and support. I thank my sister Corina for sending good thought across the ocean and all my friends for the good times, outside activities, many laughs and company.

I am deeply grateful for my wife Annette for all her love, support and her believe in me.

TABLE OF CONTENTS

	<u>Page</u>
1 INTRODUCTION	1
2 WRF SIMULATION OF SURFACE WIND RESPONSE TO AGULHAS CURRENT SST ANOMALIES	7
2.1 WRF-model description and boundary layer parameterization.....	8
2.1.1 Special consideration of turbulence and entrainment	13
2.2 Comparison of simulated and observed wind response.....	16
2.2.1 Conclusion	20
3 ABL RESPONSE TO MIDLATITUDE SST FRONTS	30
3.1 Simulations with idealized SST fronts.....	34
3.1.1 Methodology	38
3.1.2 Analysis of the simulated momentum budget	43
3.2 Results from cold-to-warm SST front experiment (P4)	44
3.2.1 Equilibrium and quasi-equilibrium region (P4)	45
3.2.2 Non-equilibrium transition region (P4)	47
3.2.3 ABL average and surface momentum budget (P4)	48
3.3 Results from warm-to-cold SST front experiment (M4).....	50
3.3.1 Equilibrium and quasi-equilibrium region (M4)	50
3.3.2 Non-equilibrium advection region (M4)	52
3.3.3 ABL average and surface momentum budget (M4)	53
3.4 Comparison of the responses between P4 and M4.....	54
3.5 Discussion.....	55
4 ABL RESPONSE TO IDEALIZED MESOSCALE MIDLATITUDE SST ANOMALIES.....	90

TABLE OF CONTENTS (Continued)

	<u>Page</u>
4.1 Model description and initial fields	91
4.1.1 SST Forcing	92
4.1.2 Results	93
4.2 Discussion	99
 5 A LINEAR DIAGNOSTIC MODEL OF ABL RESPONSE TO MESOSCALE SST ANOMALIES	 111
5.1 A Linearized ABL-averaged diagnostic model	111
5.2 Discussion	118
 6 SUMMARY	 131
 BIBLIOGRAPHY	 134
 APPENDICES	 139
APPENDIX A WRF-model η -levels and nominal heights	140
APPENDIX B Solution to the Diagnostic Model Appendix	141

LIST OF FIGURES

<u>Figure</u>		<u>Page</u>
2.1	Map of averaged July 2002 AMSR SST. Shaded SST contours are shown in 2°C intervals. Gray rectangles denote the boundaries of the WRF simulation. Missing SST data around islands are masked white and interpolated for the aqua-planet simulation. SST contours are used as overlays in subsequent map figures.	22
2.2	Comparison between WRF simulation (top) and QuikSCAT observation (bottom) averaged over the month of July 2002. Maps show inner WRF domain simulations and corresponding QuikSCAT observations of wind speed perturbations. Contours of SST perturbation are overlaid. The contour interval is 1°C.	23
2.3	As in Fig. 2.2, except for zonal wind. SST contour interval is 2°C. . .	24
2.4	As in Fig. 2.2, except for meridional wind. SST contour interval is 2°C.	25
2.5	Binned scatterplots of the relationships between the perturbation divergence and the perturbation downwind SST gradient: (top) perturbation divergence of WRF-model and (bottom) perturbation divergence of QuikSCAT observation. The points are the means within each bin computed from 28 consecutive days, and the error bars are ± 1 std dev of the means within each bin. The lines through the points represent least square fits of the binned overall means to straight lines.	26
2.6	As in Fig. 2.5, except for the perturbation curl and the perturbation crosswind SST gradient.	27
2.7	Binned scatterplots of the angular relationships between the wind and the SST field. Top panel shows WRF perturbation wind divergence as a function of the angle between crosswind and downwind SST gradient. Bottom panel shows QuikSCAT perturbation wind divergence as function of the angle between crosswind and downwind SST gradient. The points are the means within each bin computed from 28 consecutive days, and the error bars are ± 1 std dev of the means within each bin. The lines through the points represent least square fits of the binned overall means to a cosine curve.	28
2.8	As in Fig. 2.7, except for the WRF perturbation curl (top) and the QuikSCAT perturbation curl as a function of the angle between crosswind and downwind SST gradient. The lines through the points represent least square fits of the binned overall means to sine.	29

LIST OF FIGURES (Continued)

<u>Figure</u>	<u>Page</u>
3.1 Maps of background SST in the region of the Agulhas return current. Shaded SST is shown in 2°C contour intervals. Gray rectangles denote the boundaries of the 3 nested WRF domains. Inside the WRF domains the SST is increased by 4 K within a narrow north-south frontal region.	59
3.2 Bin-averaged distribution of normalized momentum boundary layer depth as function of longitude in the upstream region. Each vertical profile is a distribution at a given longitude. A thick line denotes the ABL depth that occurred most often. Top panel is derived from the P4 experiment and the bottom panel from the M4 experiment. The vertical bin size for each distribution is 50m. Shown is the region upstream of the SST front where the momentum boundary layer depth is not influenced by the SST front.	60
3.3 Longitude-height cross-section of the potential temperature θ . Top panel shows results from P4 and bottom panel results from M4. The solid line in each panel denotes the momentum boundary layer depth; the thick dashed line in the upper panel is a measure of the internal boundary layer depth. See text for the definitions of the boundary layer depths.	61
3.4 Sea surface temperature at 43° S as function of longitude. Dots represents model gridpoint locations. Latitudinal dependence of SST is approximately a cosine function of the latitude.	62
3.5 Top: Near-surface advection as a function of longitude. Bottom: Co-located sea surface temperature distribution as function of longitude.	63
3.6 Schematic description of the cold-to-warm experiment.	64
3.7 As in Fig. 3.3, except for the zonal (top) and meridional (bottom) velocity of the P4 experiment.	65
3.8 As in Fig. 3.3, except for the zonal (top) and meridional (bottom) turbulent stress convergence of the P4 experiment.	66
3.9 As in Fig. 3.3, except for the zonal (top) and meridional (bottom) turbulent stress of the P4 experiment.	67
3.10 As in Fig. 3.3, except for the zonal (top) and meridional (bottom) advection of the P4 experiment.	68

LIST OF FIGURES (Continued)

<u>Figure</u>	<u>Page</u>
3.11 As in Fig. 3.3, except for the zonal (top) and meridional (bottom) pressure gradient force of the P4 experiment.	69
3.12 As in Fig. 3.3, except for the turbulent kinetic energy of the P4 experiment.	70
3.13 As in Fig. 3.3, except for the buoyancy production of turbulent kinetic energy of the P4 experiment.	71
3.14 Ratio of surface stress to momentum boundary layer depth as function of longitude. Solid line denotes the magnitude τ_s/H , dashed the zonal component τ_x/H and dotted the meridional component τ_y/H	72
3.15 Momentum boundary layer average zonal (top) and meridional (bottom) momentum budget as function of longitude. The zonal and the meridional residual is denoted by X, Y, respectively.	73
3.16 Zonal (top) and meridional (bottom) momentum balance at near surface model level (12m) as function of longitude. Shown are advection (solid), coriolis (thick dash-dotted), pressure gradient (dashed) and turbulent stress convergence (thick dotted).	74
3.17 Vertically staggered vector representation of the momentum budget from P4. Northward vectors are pointing up and eastward vectors point to the right. Top panel vectors represent Coriolis (orange), advection (blue), turbulent stress convergence (“ τ ”, black), and pressure gradient force (“PGF”, green). Additionally wind direction (“Wind”) is overlaid in gray. Bottom panel shows selection of top panel magnified with colored vectors for advection (blue) and turbulent stress convergence (black), other vectors are repeated for completeness, but grayed-out for clarity. Note that not all grid locations are showed. . .	75
3.18 Top: Near-surface advection as a function of longitude. Bottom: Co-located sea surface temperature distribution as function of longitude.	76
3.19 As in Fig. 3.3, except for the zonal (top) and meridional (bottom) velocity for the M4 experiment.	77
3.20 As in Fig. 3.3, except for the zonal (top) and meridional (bottom) turbulent stress convergence of the M4 experiment.	78
3.21 As in Fig. 3.3, except for the zonal (top) and meridional (bottom) turbulent stress of the M4 experiment.	79

LIST OF FIGURES (Continued)

<u>Figure</u>	<u>Page</u>
3.22 As in Fig. 3.3, except for the zonal (top) and meridional (bottom) advection of the M4 experiment.	80
3.23 As in Fig. 3.3, except for the zonal (top) and meridional (bottom) pressure gradient force of the M4 experiment.	81
3.24 As in Fig. 3.3, except for the turbulent kinetic energy of the M4 experiment.	82
3.25 Ratio of surface stress to ABL depth as function of longitude. The solid line denotes the magnitude τ_s/H , dashed the zonal component τ_x/H and dotted the meridional component τ_y/H	83
3.26 Momentum boundary layer average zonal (top) and meridional (bottom) momentum budget as function of longitude. The zonal and the meridional residual is denoted by X, Y, respectively.	84
3.27 Zonal (top) and meridional (bottom) Momentum Balance at near surface model level (12m) as function of Longitude. Shown are Advection (solid), Coriolis (thick dash-dotted), Pressure gradient (dashed) and turbulent stress convergence (thick dotted).	85
3.28 Vertically staggered vector representation of the momentum budget from M4. Northward vectors are pointing up and eastward vectors point to the right. Top panel vectors represent Coriolis (orange), advection (blue), turbulent stress convergence (“ τ ”, black), and pressure gradient force (“PGF”, green). Additionally wind direction (“Wind”) is overlaid in gray. Bottom panel shows selection of top panel magnified with colored vectors for advection (blue) and turbulent stress convergence (black), other vectors are repeated for completeness, but grayed-out for clarity. Note that not all grid locations are shown. . . .	86
3.29 Longitude-height cross section of 1) zonal turbulent flux convergence from P4 and M4 added and zonal mean removed (top) and 2) zonal advection from P4 and M4 added and zonal mean removed (bottom). . . .	87
3.30 Vertical profile of the zonal (top) and meridional (bottom) momentum budget from P4 at three locations. Shown from left to right are the upstream, transition and downstream region relative to the SST front. Note the order-1 difference of scales of zonal and meridional budgets. . . .	88

LIST OF FIGURES (Continued)

Figure	Page
3.31 Vertical profile of the zonal (top) and meridional (bottom) momentum budget from M4 at three locations. Shown from left to right are the upstream, transition and downstream region relative to the SST front. Note the order-1 difference of scales of zonal and meridional budgets.	89
4.1 Maps of background SST in the region of the Agulhas return current. Shaded SST is shown in 2°C contour intervals. Gray rectangles denote the boundaries of the 2 nested WRF domains. Contour interval for the WRF domains is 1°C , outside contour interval 2°C	101
4.2 Map of near-surface zonal (top) and meridional (bottom) wind speed perturbations with SST contour and mean wind speed vector overlay.	102
4.3 Composites of boundary layer variables as function of longitude: SST perturbation and boundary layer depth (top panel) near the location of maximum boundary layer depth variation. Perturbation of advection and turbulent stress convergence (second panel). Ratio of perturbation surface stress and boundary layer depth (" τ/H "), Coriolis force ("Coriolis") and pressure gradient force ("PGF") (third panel). Longitude-height cross section (bottom panel) of meridional turbulent stress convergence (shaded) with zonal velocity (black) and boundary layer depth (gray) contours overlaid.	103
4.4 Composites of boundary layer variables as function of longitude: SST perturbation and boundary layer depth (top panel) near the location of maximum boundary layer depth variation. Perturbation of advection and turbulent stress convergence (second panel). Coriolis force ("Coriolis") and pressure gradient force ("PGF") (third panel). Longitude-height cross section (bottom panel) of meridional turbulent stress convergence (shaded) with meridional velocity (black) and boundary layer depth (gray) contours overlaid.	104
4.5 Composites of surface pressure gradient force and SST. Top panel shows zonal and bottom panel meridional maps of shaded "PGF" and contour SST overlaid. Zero contour lines are omitted for clarity.	105
4.6 Composites of surface pressure gradient force and SST. Top panel shows modeled PGF from the WRF simulation and bottom panel PGF estimates based on the horizontal change of potential temperature θ (Eqn. 4.3). Contours of SST are overlaid. Zero contour lines are omitted for clarity.	106

LIST OF FIGURES (Continued)

<u>Figure</u>	<u>Page</u>
4.7 Boundary layer integral of zonal PGF and SST. The composite of the top row is identical to the bottom row shifted by one-half wavelength to show the spatial structure. Note that some additional smoothing has been applied to remove very high wavenumber noise of unknown origin.	107
4.8 As in (Fig. 4.7, except for the zonal stress.	108
4.9 As in (Fig. 4.7, except for the zonal advection.	109
4.10 As in (Fig. 4.7, except for the zonal momentum budget.	110
5.1 Latitude-height cross section of estimated pressure gradient force with ABL depth (bottom panel) and SST (top panel). Estimate of “PGF” is shaded with contour of ABL depth (gray) as overlay.	123
5.2 Map of 1-layer diagnostic model zonal velocity (top) and WRF-model averaged zonal surface velocity (repeated for comparison, bottom). SST contours are shown as overlays with contour interval of .5°C. Zero contour of SST is omitted for clarity.	124
5.3 Map of 1-layer diagnostic model meridional velocity (top) and WRF-model averaged meridional surface velocity (repeated for comparison, bottom). SST contours are shown as overlays with contour interval of .5°C. Zero contour of SST is omitted for clarity.	125
5.4 Map of surface to vertically integrated meridional velocity ratio derived from WRF-model simulation. Top panel shows zonal velocity ratio, bottom panel shows meridional velocity ratio. Locations with vertically integrated velocities of less than 0.05 m/s have been masked. SST contours are shown as overlays with contour interval of .5°C. Positive values of SST is shown as solid and negative SST as dashed contours, the zero contour of SST is omitted for clarity.	126
5.5 Map of 1-layer diagnostic model divergence and SST perturbations. . .	127
5.6 Map of 1-layer diagnostic model curl and SST perturbations.	128
5.7 Binned scatterplots of the relationships between the SST and wind velocity fields calculated from the diagnostic solution of the 1-layer model. Top panel shows perturbation wind divergence as a function of downwind SST gradient and bottom panel shows perturbation wind curl plotted as a function of crosswind SST gradient.	129

LIST OF FIGURES (Continued)

<u>Figure</u>	<u>Page</u>
5.8	Binned scatterplots of the angular relationships between the wind and the SST field. Top panel shows perturbation wind divergence as a function of the angle between down and crosswind SST gradient and bottom panel shows perturbation wind curl plotted as a function of the angle between down and crosswind SST gradient. 130

LIST OF TABLES

<u>Table</u>		<u>Page</u>
5.1	Parameters for the 1-layer linear perturbation model. The first 11 parameters were pre-determined by the experimental design and physics. The last three values represent model parameters with a range of physically correct values (see text for details). For these three values the optimal value within the physical range were chosen. The sensitivity of the model is indicated and the influence effect is given.	122

Atmospheric Boundary Layer Coupling to Midlatitude Mesoscale Sea Surface Temperature Anomalies

1. INTRODUCTION

This dissertation focuses on monthly-averaged atmospheric boundary layer (ABL) response to midlatitude sea surface temperature (SST) anomalies on scales of 50-500 km. The oceanic mesoscale corresponds roughly to the atmospheric mesoscale β and the designation β will be dropped for simplicity. Near-surface wind speed anomalies on these scales have been observed to be co-located with SST anomalies. These correlations have only recently been revealed thanks to the advances in microwave satellite technology which have enabled high resolution surface wind stress and SST observations in virtually all-weather conditions.

Important processes that affect the near-surface winds on the scale of the SST anomalies include turbulent vertical mixing, horizontal momentum advection, turbulent entrainment, and the horizontal surface pressure gradient force. In general, all of these processes play a role in the ABL response. There has been, however, much speculation about the specific mechanism coupling the wind stress to the SST.

The quantitative theories proposed to date may be grouped into three categories:

- response of ABL wind to thermally induced changes in pressure gradient forcing (e. g. Deser 1993; Small et al. 2005)

- downward turbulent mixing of momentum with relatively constant pressure gradient forcing (e. g. de Szoeke and Bretherton 2004).
- changes in surface stress due to variations in boundary layer depth under relatively constant pressure gradient forcing (e. g. Samelson et al. 2006).

Here we perform mesoscale ABL model simulations with the necessary horizontal and vertical resolution to resolve important boundary layer processes. A detailed analysis of the simulated momentum budget is used to identify scale dependent mechanisms of the ABL adjustment and to determine which theory comes closest to explaining the observations over the midlatitude open oceans.

The numerical model is validated by comparison of the simulated near-surface winds and satellite near-surface wind observations over SST anomalies of the Agulhas current system. We then carry out numerical experiments on the ABL response to idealized SST-fronts and mesoscale SST anomalies similar in magnitude and scale to the observed SST anomalies of the Agulhas region (Fig. 3.4, Fig. 3.18, and Fig. 4.1).

A more complete literature review will be presented in the following chapters, but it is useful to mention the seminal ideas at this point that have guided much of the work on mesoscale coupling mechanisms. Suggestions regarding the importance of thermodynamic processes can be traced to the work of Lindzen and Nigam (1987). They suggest that surface heat flux over the warm tropical SST increases the lower-tropospheric air temperature. Hydrostatic adjustment then leads to surface pressure gradients with patterns of wind convergence over the warm SST and divergence over cool SST. The wind response is strongest over the strongest SST gradient. On the mesoscale, Small et al. (2005) argue that temperature advection shifts the strongest surface heat fluxes downstream of the

SST-front, for example on the north side cold of the tongue in the eastern equatorial Pacific. The shift of increased air temperature corresponds to increased surface pressure gradients downstream of the SST-front. The pressure gradient is therefore not centered over the front but shifted downstream and surface wind acceleration occurs on the warm downstream side of the SST-front. Note that the horizontal wind stress plays a passive role in the thermodynamic mechanism. The stress convergence and coriolis effects are just what is needed to balance the thermodynamically driven pressure gradients in the momentum budget.

The second class of mechanisms proposes that SST anomalies induce changes in the turbulent momentum fluxes and drive the adjustment mechanism. These ideas can be traced to the observational work of Sweet et al. (1981) and Wallace et al. (1989). They suggest that the SST induced changes of ABL stability alter the turbulent vertical mixing of momentum to the surface. Over cold SST the boundary layer tends to be more stable and the turbulent momentum flux to the surface is reduced; over warm SST mixing reduces the vertical shear and leads to increased surface wind. The quasi-Lagrangian large eddy simulations of the eastern tropical Pacific with prescribed pressure gradient force by de Szoeke and Bretherton (2005) support the hypothesized importance of the turbulent mixing effect, but were unable sort out the relative importance of wind stress convergence and pressure adjustment as ABL response mechanisms.

The potential importance of ABL depth in determining the equilibrium ABL response was recently demonstrated by Samelson et al. (2006) using an idealized quasi 2-dimensional 2-layer model. The modeled horizontal pressure gradient was held constant in time and space while the depth of the momentum boundary layer was allowed to change across the SST-front. Under these conditions, a deeper boundary layer over warm water can sustain larger surface stress than a

shallow ABL over cooler water. The ratio of ABL depth and surface stress must remain constant across the SST-front and the surface stress in this 2-layer model is founded to be independent of the momentum distribution within the boundary layer.

In this thesis we will analyze numerical simulations of the ABL adjustment to SST-fronts and mesoscale SST anomalies to sort out the relevant mechanism on meso- to synoptic scales. In Chapter 2 we will test the ability of the Weather Research and Forecasting (WRF) model, including the Grenier and Bretherton (2001, hereafter GB01) moist PBL-scheme, to simulate the observed wind-SST coupling. The WRF-model is a modern, fully modularized mesoscale numerical weather prediction system and is becoming the successor of the widely adopted Pennsylvania State University/National Center for Atmospheric Research mesoscale model (known as MM5). We show that the WRF-model can simulate the correct location and the correct strength of the divergence and convergence pattern relative to the SST gradients. Momentum advection is shown to play an important role in the adjustment of the boundary layer and is fundamental to reproducing the SST-divergence pattern accurately. The method of Chelton et al. (2001) is used to calculate coupling coefficients for wind divergence perturbation as a function of SST gradient perturbations (see also Chelton et al. 2004; O'Neill et al. 2003; 2005). These results are used to quantify the relationship of the model divergence to SST gradients and to compare the simulated ABL response with satellite observations. Chapter 2 also provides an introduction to the GB01 moist PBL-scheme and discusses the general WRF-model setup and provide. A literature review focuses on the modeling aspect of previous studies.

In Chapter 3 the WRF-GB01 model is used to simulate the response of the boundary layer to idealized step-like SST fronts. The chapter provides a more

detailed literature review on the suggested mechanisms of ABL adjustment. The design of the SST-front experiments were inspired by the analogy to the method of determining the response of a linear system to step-like excitation. Although the finite difference scheme of the WRF-model does not allow for true step-like SST changes, the imposed SST gradient is comparable to large observed SST gradients in the open ocean (de Szoeke et al. 2005). Two independent model runs were performed to simulate the boundary layer response to a positive SST jump and a negative SST jump in the direction of the mean background wind, thereby simulating a warm-to-cold and a cold-to-warm transition. The strongest model responses were found on small scales of less than 200 km which give rise to the co-located pattern of surface wind divergence and SST-gradient. The responses from cold-to-warm and from warm-to-cold are not symmetric, i. e., not strictly linear, and by means of the momentum budget and the internal structure of the boundary layer we discuss and isolate the dominant physical mechanisms in the case of warm and cold frontal transitions.

In Chapter 4 we apply our understanding of the boundary layer response from Chapter 3 to simulations of wind response to simplified SST anomalies that are more characteristic of the open ocean. In the Agulhas region, the monthly averaged SST pattern (O'Neill et al. 2005) appears to be a quasi-periodic series of warm and cold anomalies with spatial scales on the the order of 200-500 km giving ABL horizontal advective timescales of ~ 6 hours. These scales suggest that the ABL must continually adjust to changing SST over the entire Agulhas region. The perturbations of the pressure gradient and Coriolis force are found to be important on the mesoscale and we speculate about ABL adjustment mechanisms as a function of scale.

Chapter 5 presents a simple 1-layer diagnostic ABL model for mesoscale perturbations of purely zonal mean flow. The 1-layer model results are in good agreement with the vertically averaged WRF-GB01 results in Chapter 4 and allow for prediction of phase shifts and magnitude of the perturbation wind and wind stress in terms of SST phase and magnitude. The coupling coefficients first used by Chelton et al. (2001) to quantify the relation between SST and surface wind stress are well predicted by the 1-layer model and it shows that the driving force for the ABL-averaged flow is the pressure gradient term.

2. WRF SIMULATION OF SURFACE WIND RESPONSE TO AGULHAS CURRENT SST ANOMALIES

Advances in microwave satellite technology allow an unobstructed view of the world's ocean because clouds are virtually transparent in the microwave band except during periods of heavy precipitation. Newly available high resolution satellite observation of near-surface wind and sea surface temperature (SST) have increased the knowledge about boundary layer adjustments over changing SST. The coupling of the divergence and the curl of the wind field to the gradient of SST is well established. However, the two dimensional satellite observations at the ocean surface alone only allow speculations about the manifestation of surface properties throughout the atmospheric boundary layer (ABL). The lack of detailed three dimensional observations over most of the global ocean makes numerical models an attractive tool for the study of air-sea interactions. Previous numerical simulations, however, have not lead to any consensus on the mechanism that connects mesoscale SST anomalies with the low-level winds.

The primary goal of this chapter is to introduce and validate the Weather Research and Forecast (WRF) model for our purposes and to explain the basic experimental setup for a realistic ABL simulation over the Agulhas region. The chapter will also be used to describe the initial and background state of the idealized experiments of Chapter 3.

This chapter will first provide an introduction to the WRF-model and the boundary layer scheme we have implemented in WRF to improve the quality and physical interpretation of the simulations. The WRF-model is applied in a realistic simulation of the boundary layer response over Agulhas return current where high resolution satellite observations of SST and near surface winds allow quantitative comparison with observations.

2.1. WRF-model description and boundary layer parameterization

We use the Weather Research and Forecasting (WRF) modeling system version 2 (Skamarock et al. 2005) with a state-of-the-art moist planetary boundary layer scheme (Grenier and Bretherton 2001, hereafter GB01). The key component of the WRF-model is the Advanced Research WRF (ARW) dynamic solver (Wang et al. 2006). The solver provides the solutions to the fully compressible nonhydrostatic equations on a mass-based terrain-following coordinate system. The WRF-model provides two-way nesting capabilities and full physics options for land-surface, boundary layer, radiation, microphysics and cumulus parameterization.

In this section we briefly describe all components of the model. The WRF software framework provides the modular infrastructure for ease in combining various representations of physical processes in the atmosphere. It is a practical impossibility to test all available model configurations. Whenever possible we choose physics options that performed well in previous studies or are the defaults for fifth generation Pennsylvania State University–NCAR mesoscale model (MM5) and the NCEP Eta-model. The microphysics includes resolved water vapor, cloud, and precipitation processes. In this study the simple WRF Single-Moment 3-class (WSM3) scheme is used and is carried out at the end of the time step. This guarantees that the final saturation balance is accurate for the updated temperature and moisture (Skamarock et al. 2005). Atmospheric radiative heating and radiative flux divergence were calculated using the Rapid Radiative Transfer Model Longwave parameterization (Mlawer et al. 1997) and the Eta Geophysical Fluid Dynamics Laboratory Shortwave parameterization (Lacis and Hansen 1974). The radiation physics package is only called every 4th time step (12 min.) to reduce the

computation. Radiation does not change significantly in this time. The modified version of the Kain-Fritsch scheme (Kain and Fritsch 1990; Kain 2004) is used to represent sub-grid-scale effects of convection and shallow clouds. In terms of cumulus physics, the grid size of 8.3 km is fine enough to resolve some features of the largest convective eddies, however, the convective eddies are not entirely resolved and the cumulus parameterization scheme must represent the remaining effects of cumulus convection on smaller spatial scales (Skamarock et al. 2005), such as releasing latent heat in the convective column. In addition this scheme provides the heating and moistening effects from shallow cumulus. In internally stratified boundary layers the effects of shallow clouds become important for the ABL parameterization because of their effects on the turbulent kinetic energy budget and hence the mixing coefficients. The surface layer scheme provides surface exchange coefficients for heat, moisture, and momentum. It does not calculate any tendencies, but only provides stability-dependent information to the land-surface and the ABL scheme. We chose the similarity-theory-based MM5 scheme which uses a Charnock relation to relate roughness length to friction velocity over the ocean. The calculation of a complex surface energy budget is not necessary because we prescribe the SST and thus we were able to use a simple thermal diffusion land-surface scheme. It provides sensible and latent heat flux to the ABL scheme. We completed the implementation by McCaa (personal communication) of the GB01 moist ABL parameterization. The details of the GB01 ABL scheme are discussed below.

A time-splitting integration scheme is used to solve the Euler equations. The basic set of equation is given below in their flux-forms:

$$\partial_t U + (\nabla \cdot \mathbf{V}u)_\eta - \partial_x(p\phi_\eta) + \partial_x(p\phi_x) = F_U \quad (2.1)$$

$$\partial_t V + (\nabla \cdot \mathbf{V}v)_\eta - \partial_y(p\phi_\eta) + \partial_y(p\phi_y) = F_V \quad (2.2)$$

$$\partial_t W + (\nabla \cdot \mathbf{V}w)_\eta - g(\partial_y p - \eta) = F_W \quad (2.3)$$

$$\partial_t \Theta + (\nabla \cdot \mathbf{V}\theta)_\eta = F_\Theta \quad (2.4)$$

$$\partial_t \mu + (\nabla \cdot \mathbf{V})_\eta = 0 \quad (2.5)$$

$$\partial_t \phi + \mu^{-1} \left[(\mathbf{V} \cdot \nabla \phi)_\eta - gW \right] = 0 \quad (2.6)$$

with the vertical coordinate μ and the flux form variables defined as

$$\mu = (p_h - p_{ht})/\mu \quad \text{where} \quad \mu = p_{hs} - p_{ht} \quad (2.7)$$

$$\mathbf{V} = \mu \mathbf{v} = (U, V, W), \quad \mathbf{v} = (u, v, w), \quad \Theta = \mu \theta \quad (2.8)$$

These are the three momentum equations (2.1 – 2.3) for the zonal velocity u , the meridional velocity v and the vertical velocity w ; the thermodynamic equation (2.4) for the potential temperature θ ; the mass conservation equation (2.5) and the equation for the non-conserved geopotential (2.6). Density can be diagnosed from:

$$\partial_\eta \phi = -\alpha \mu. \quad (2.9)$$

and pressure from the equation of state:

$$p = p_0 (R_d \theta / p_0 \alpha)^\gamma, \quad (2.10)$$

where $\gamma = c_p/c_v = 1.4$ is the ratio of the heat capacities and R_d is the gas constant for dry air.

Moisture is included into (2.1–2.6) by introducing mass mixing ratios and conservation equations for hydro meteors rather than introducing source terms in the mass conservation equation (2.5). The coupling to the dry air mass μ_d is retained. The moist Euler equations become:

$$\partial_t U + (\nabla \cdot \mathbf{V}u)_\eta + \mu_d \alpha \partial_x p + (\alpha/\alpha_d) \partial_\eta p \partial_x \phi = F_U \quad (2.11)$$

$$\partial_t V + (\nabla \cdot \mathbf{V}v)_\eta + \mu_d \alpha \partial_y p + (\alpha/\alpha_d) \partial_\eta p \partial_y \phi = F_V \quad (2.12)$$

$$\partial_t W + (\nabla \cdot \mathbf{V}w)_\eta - g [(\alpha/\alpha_d) \partial_\eta p - \mu_d] = F_W \quad (2.13)$$

$$\partial_t \Theta + (\nabla \cdot \mathbf{V}\theta)_\eta = F_\Theta \quad (2.14)$$

$$\partial_t \mu_d + (\nabla \cdot \mathbf{V})_\eta = 0 \quad (2.15)$$

$$\partial_t \phi + \mu_d^{-1} [(\mathbf{V} \cdot \nabla \phi)_\eta - gW] = 0 \quad (2.16)$$

$$\partial_t Q_v + (\nabla \cdot \mathbf{V}q_v)_\eta = F_{Q_v} \quad (2.17)$$

$$\partial_t Q_c + (\nabla \cdot \mathbf{V}q_c)_\eta = F_{Q_c} \quad (2.18)$$

$$\partial_t Q_r + (\nabla \cdot \mathbf{V}q_r)_\eta = F_{Q_r} \quad (2.19)$$

$$\partial_t Q_i + (\nabla \cdot \mathbf{V}q_i)_\eta = F_{Q_i}. \quad (2.20)$$

$Q_{v,c,r,i}$ are the mass-coupled mixing ratios for water vapor, cloud, rain and ice. The moist potential temperature is approximated by $\theta_m = \theta(1 + 1.61q_v)$ and the diagnostic relations for the full pressure and the inverse density are:

$$p = p_0 (R_d \theta_m / p_0 \alpha_d)^\gamma, \quad (2.21)$$

$$\partial_\eta \phi = -\alpha_d \mu_d. \quad (2.22)$$

The full parcel density α^{-1} is calculated as the sum over all mixing ratios times the dry density:

$$\alpha = \alpha_d (1 + q_v + q_c + q_r + q_i)^{-1} \quad (2.23)$$

where q_η are the uncoupled mixing ratios.

Removing the hydrostatically balanced part of the pressure gradient yields a set of equations which are spatially discretized on a Arakawa C-grid. The temporal discretization separates low-frequency from high-frequency acoustic modes. The low-frequency modes are integrated with a third-order Runge-Kutta (RK3)

scheme. The efficiency of the solver is increased because the high-frequency modes are calculated on shorter time steps at each RK3 integration while the low-frequency modes are held constant. The acoustic time step and the choice of the accuracy of the flux divergence (2^{nd} to 6^{th} order) determine the stable Courant number. In this study we used 5^{th} order accuracy and the theoretical Courant number is $Cr_{theory} = 1.42$ (Skamarock et al. 2005). This large number comes at the expense of 3 calculations (plus acoustic mode) per time step. For a three-dimensional experiment, the time step should satisfy:

$$\Delta t_{max} < \frac{Cr_{theory}}{\sqrt{3}} \cdot \frac{\Delta x}{u_{max}} \quad (2.24)$$

The maximum time step with $\Delta x = 8333\text{m}$ and $u_{max} = 100\text{ms}^{-1}$ is approximately 70 s. The acoustic step however uses a forward-backward time integration with a different Courant number. The maximum allowed time step is $Cr_{max} = c_s \Delta \tau / \Delta x < 1/\sqrt{2}$ but a more conservative estimate for the acoustic step is:

$$\Delta \tau < \frac{\Delta x}{2 \cdot c_s}. \quad (2.25)$$

With the sound speed $c_s = 300\text{ms}^{-1}$ and $\Delta x = 8333\text{m}$, the acoustic time step is approximately 14 s. For the WRF simulations we have specified a time step of 60 s and a 1:6 ratio of RK3 time step to the acoustic time step. The acoustic time step is therefore 10 s and satisfies the conservative estimate of the Courant number.

To resolve the boundary layer accurately we use 69 vertical levels on a stretched vertical grid with 35 levels below 1500 m. (The model sigma levels are listed in APPENDIX A). The model is either run in a 2 or 3 domain configuration. The 2-domain (1 nest) configuration is used for the validation of the model while

the 3-domain (2 nests) is used to achieve higher horizontal resolution. Time step and grid size ratios are chosen to satisfy the Courant number constraints shown above.

2.1.1. Special consideration of turbulence and entrainment

The boundary layer scheme and the WRF-model itself are relatively new developments and have not been used very widely. The GB01 has performed well in the tropics and subtropics (McCaa and Bretherton 2004) but it has not been tested in combination with the WRF-model. The GB01 offers some advantages over other boundary layer schemes. It attempts to simulate the tight coupling between cloud formation, convective turbulence, radiative and surface fluxes and it can handle the internal stratification of a cloud topped boundary layer (Grenier and Bretherton 2001), meaning that it is able to resolve several convective layers within the ABL.

This analysis focuses on the boundary layer and it is therefore worthwhile to examine its numerical representation. The boundary layer model is based on Grenier and Bretherton 2001 and uses a 1.5 order turbulence closure. The original numerical implementation was provided by McCaa (McCaa 2001, personal communication). Turbulent flux divergence, namely $\frac{\partial}{\partial z}\langle u'w' \rangle$ and $\frac{\partial}{\partial z}\langle v'w' \rangle$, is discretized vertically by:

$$\langle w'X'_{h,m} \rangle = K_{h,m}\rho g \frac{\delta X}{\delta p} \quad (2.26)$$

where δX is a generalized vertical difference operator. The eddy diffusivities of K_h for conserved thermodynamic variables and the eddy viscosity K_m are related to the turbulent kinetic energy e , a master length scale l and stability functions $S_{h,m}$:

$$K_{h,m} = l\sqrt{e}S_{h,m} \quad (2.27)$$

The length scale l is based on the concept that in a turbulent environment a vertically displaced air parcel will transport its perturbation velocity u' a characteristic distance l and then creates a fluctuation in the turbulence. The specification of the stability function $S_{h,m}$ follows the definition of Galperin et al.(1988).

In the case of convective and stable ABLs, the master length scale is specified after Blackader (1962):

$$l = kz/(1 + kz/\lambda) \quad (2.28)$$

with the asymptotic length scale $\lambda = \eta_l z_i$, $\eta_l = 0.1$. In the case of a decoupled ABL the parcel length scale l_p is more appropriate. The parcel length scale l_p consists of an upward and downward length scale l_u and l_d , and is calculated based on the buoyancy of the parcel at the point where it would reach zero velocity. The upward and downward length scales are limited by the distances from the parcel to the ABL top and the surface, respectively.

$$l_p = \eta_l(l_u + l_d) \quad (2.29)$$

The parcel length scale is incorporated into the definition of the master length scale:

$$l = kz/(1 + kz/l_p) \quad (2.30)$$

The relationship to the Blackadar length scale is obvious for a single convective layer when the parcel length scale l_p is identically $l_p = \eta_l z_i = \lambda$.

The model is closed by specifying an entrainment velocity w_e at the base of the ABL inversion (subscript i). The Turner-Deardorff closure approach (Turner

1973) relates w_e to an eddy length scale L and a velocity scale U , the entrainment efficiency A and the buoyancy jump $\Delta_i b$ across the inversion :

$$w_e = AU^3/(L\Delta_i b) \quad (2.31)$$

With the local entrainment closure approach (GB01), the eddy size and velocity scales are taken from just below the inversion and set to $L = l_i$ and $U = \sqrt{e_i}$.

Thus w_e becomes

$$w_e = A \frac{e_i \sqrt{e_i}}{l_i \Delta_i b} \quad (2.32)$$

In (2.32) the entrainment efficiency A is chosen following GB01. The convective ABL is assumed to be topped with an infinitely thin inversion (GB01) at some grid point i at the inversion height. The turbulent fluxes of X at this height are parameterized following (Lilly 1968):

$$\langle w'X' \rangle_i = -w_e \Delta_i X \quad (2.33)$$

The ABL model uses the the so-called 'restricted inversion' (GB01) method to calculate the inversion jump $\Delta_i X$ of variable X across the inversion. In this method, the inversion is restricted to lie on a flux level of the model. The layer which contains the inversion is therefore composed of a mix of ABL properties from below the inversion and free atmospheric properties from above. Grenier and Bretherton (GB01) refer to this layer as the 'ambiguous layer'. This method is computationally simple and allows deepening of the boundary layer implicitly through entrainment. Entrainment acts to reduce the difference between the ambiguous layer and the well mixed ABL properties, thereby reducing the stratification until ultimately the inversion is diagnosed to lie one grid level above the previous inversion.

2.2. Comparison of simulated and observed wind response

The WRF-model and the GB01 parameterization are relatively new and we feel that it is necessary to quantify the performance of the WRF-model/GB01 combination. Therefore, the new WRF-model-GB01 version of the model is tested in a realistic simulation over the Agulhas return current. South-east of the Republic of South Africa, the Agulhas return current meanders with quasi-stationary troughs and crests that separate the cold Southern Ocean from the warmer Indian Ocean (O'Neill et al. 2005). The accompanying SST distribution contains sharp mesoscale SST gradients (Fig. 2.1) and the large-scale SST gradient is to the north, perpendicular to the mean zonal wind. The land influence is minimal. In combination with the availability of satellite observations of both SST and wind speed, the Agulhas region is an ideal environment for model validation and in particular to test the performance of the boundary layer scheme over the open ocean.

The SST data is obtained from the Advanced Microwave Scanning Radiometer (AMSR) onboard the Earth Observing System (EOS)-Aqua system (Chelton and Wentz 2005). The AMSR measures polarized brightness temperatures at six microwave frequencies. The resolution of the derived SST product is about 58 km and all available locations for the month of July 2002 were averaged onto a 0.25° grid. The rms accuracy for a single observation is on the order of 0.5° C but the random error is much smaller for the 30 day average considered in this study.

The initial fields and boundary condition for the 30 day WRF-model simulation is obtained from NCEP's Global Data Assimilation System (GDAS). The Global Final Analyses data sets consist of simulations over the entire globe on a

$1.0^\circ \times 1.0^\circ$ grid of the spectral Medium Range Forecast model. Spectral modes are interpolated on pressure levels and are available every 6 hours.

The period of July 2002 was motivated by the observed annual cycle of coupling coefficients (O'Neill et al. 2005) with largest coupling coefficients during austral winter. The bottom boundary consists of averaged AMSR SST and is held constant throughout the simulation. The analyzed results from the WRF simulation are averaged over the last 28 days to allow spin-up time of 2 days at the beginning of the simulation.

The WRF-model near-surface wind that is used in the comparison is the 10m wind product from the model. The model 10m wind product and the wind speed of the lowest model level are virtually identical because the lowest model level lies on average at 12m. The QuikSCAT wind product is a 10m equivalent neutral wind derived from surface roughness. Over the worlds ocean the near-surface stratification is usually slightly unstable and on average 10m anemometer measurement are about 0.2ms^{-1} lower than scatterometer 10m estimates (Mears et al. 2001). The accuracy for QuikSCAT wind vectors has been estimated to be about 1.7ms^{-1} in wind speed and about 14° in direction (Chelton and Freilich 2005).

The agreement between the WRF-model simulation and the satellite observation of 10 m wind is remarkable. Maps of high-pass filtered wind speed and high-pass filtered SST (Fig. 2.2) emphasize the very good agreement for the purpose of this dissertation. Higher wind speed is simulated over relatively warm SST and lower wind speed over relatively cool SST. The model zonal wind (Fig. 2.3) in the eastern part of the domain is slightly smaller than the observed QuikSCAT zonal wind. The observed and modeled zonal wind speed in the western part of the domain agree fairly well. The relationship between the meridional component

and SST can also be seen in Fig. 2.4 but is less obvious. This is in part due to the generally lower meridional wind speed magnitudes which reduces the magnitude of the wind response. The zonal and meridional components of the WRF-model show generally less high wavenumber details than the QuikSCAT observations, which indicates that the effective resolution of the WRF-model is less than the QuikSCAT observation, potentially because the SST forcing had to be interpolated onto WRF-model grid and is therefore smoother than the SST that underlies the QuikSCAT observations. On the other hand, there is no guarantee that the high wavenumber details in QuikSCAT are reliable. The 30° longitude by 10° latitude spatial high-pass 2-D loess-filter (Cleveland and Devlin 1988; Schlax et al. 2001) removes the slow varying background field and therefore, large scale biases between model and observations are not obvious in the comparison.

The relation between surface winds and SST can be quantified in terms of wind divergence and curl as functions of downwind and crosswind SST gradients, respectively (Chelton et al. 2001; 2004; O'Neill et al. 2003; 2005). The prime symbol in Eqn. 2.34 and Eqn. 2.35 denote the high-pass filtered part of the variable and is the same 30° longitude by 10° latitude loess-filter used by O'Neill (2003 and discussion therein).

$$\nabla \cdot \mathbf{u}'_{\mathbf{o}} = s_1 \cdot (\nabla T \cdot \hat{\mathbf{u}}_{\mathbf{o}})' \quad (2.34)$$

$$\nabla \times \mathbf{u}'_{\mathbf{o}} = -s_2 \cdot (\nabla T \times \hat{\mathbf{u}}_{\mathbf{o}})' \quad (2.35)$$

The derivative wind fields of QuikSCAT were computed using in-swath results which are averaged over the month of July 2002. Note that O'Neill (2005) used surface wind stress to compute the coefficients while here surface wind speed is used, which effects the magnitude of the coefficients. The methods used here are otherwise identical. The derivative fields of WRF-model were computed from daily

vector averages of the wind and then averaged for the month of July 2002. Each coefficient $s_{1,2}$ characterizes the wind-SST relation for the entire region of interest and can be used to compare WRF simulations and QuikSCAT observations in a quantitative way. For this comparison, the divergence and curl as well as the down and crosswind SST gradients have been calculated by Larry O'Neill (Oregon State University) to ensure consistency with previous studies. The binned scatterplots of divergence and curl as functions of SST gradient are shown in Fig. 2.5 and Fig. 2.6, respectively. The very good agreement found for the zonal and meridional wind components (Fig. 2.3 and Fig. 2.4) is quantified by the similarity of the coefficient s_1 for WRF-model and QuikSCAT surface wind divergence (Fig. 2.5) as well as the agreement for the surface wind curl coefficient s_2 (Fig. 2.6). The difference between the coefficient for the divergence s_1 and the curl s_2 has been observed by Chelton et al. (2001; 2004) and O'Neill et al. (2003; 2005). One potential mechanism for different coupling coefficients may be the difference in vertical shear between the zonal and meridional wind component and we will discuss this mechanism further in Chapter 4 and 5. The current chapter, however, only focuses on the comparison between the WRF-model simulation and satellite observations.

The perturbation crosswind and downwind components of the SST gradient may be expressed similarly as:

$$\nabla T \cdot \mathbf{u}'_{\mathbf{o}} = |\nabla T| \cdot \sin \theta' \quad (2.36)$$

$$\nabla T \times \mathbf{u}'_{\mathbf{o}} = |\nabla T| \cdot \cos \theta' \quad (2.37)$$

where the counterclockwise angle θ' is defined as:

$$\theta' = \tan^{-1} \left[\frac{\nabla T \times \mathbf{u}'_{\mathbf{o}}}{\nabla T \cdot \mathbf{u}'_{\mathbf{o}}} \right] \quad (2.38)$$

(Chelton et al. 2001; O'Neill et al. 2005).

These relations provide an additional method for quantifying the coupling between

surface wind response and SST gradient. The binned scatterplots of divergence and curl as function of counterclockwise angle θ' are shown in Fig. 2.7 and Fig. 2.8, respectively. The simulated curl and the observed curl agree very well. However the simulated response of the divergence is almost two times larger than the observed. This quantitative discrepancy is surprising given the otherwise good quantitative agreement between simulation and observation.

2.2.1. Conclusion

The WRF-model successfully reproduces the QuikSCAT satellite observations of the wind response to observed mesoscale SST anomalies. The location of local wind maxima relative to local SST maxima is in very good agreement with the observations. The quantitative relationship between the wind and SST perturbations is expressed in terms of downwind and crosswind divergence and curl and is used to summarize the performance of the WRF-model. The agreement with the QuikSCAT wind divergence and curl as functions of down and crosswind SST gradients is remarkable. The largest quantitative difference is found between for divergence as a function of counterclockwise angle θ' , while a good agreement is found for the curl as function of θ' . The overall good agreement provides confidence for using the WRF-model to investigate the atmospheric boundary layer response to midlatitude SST variability. The bias between the surface wind estimate from QuikSCAT and the model surface wind might be due in part to the differences in stability and resolution between the neutral 10m wind estimates from QuikSCAT and the simulated 10m winds from the WRF-model. On average, the marine boundary layer is slightly unstable and therefore 10m anemometer measurement are about 0.2ms^{-1} lower than scatterometer 10m neutral estimates

(Mears et al. 2001), which is in agreement with the observed differences between WRF-model and QuikSCAT in this comparison study (Fig. 2.3). The WRF-model contains less high wavenumber details than the QuikSCAT observations which indicates that the effective resolution of the WRF-model is less than the QuikSCAT observations. The mean difference does not effect the coupling coefficients since they are calculated based on perturbation winds alone.

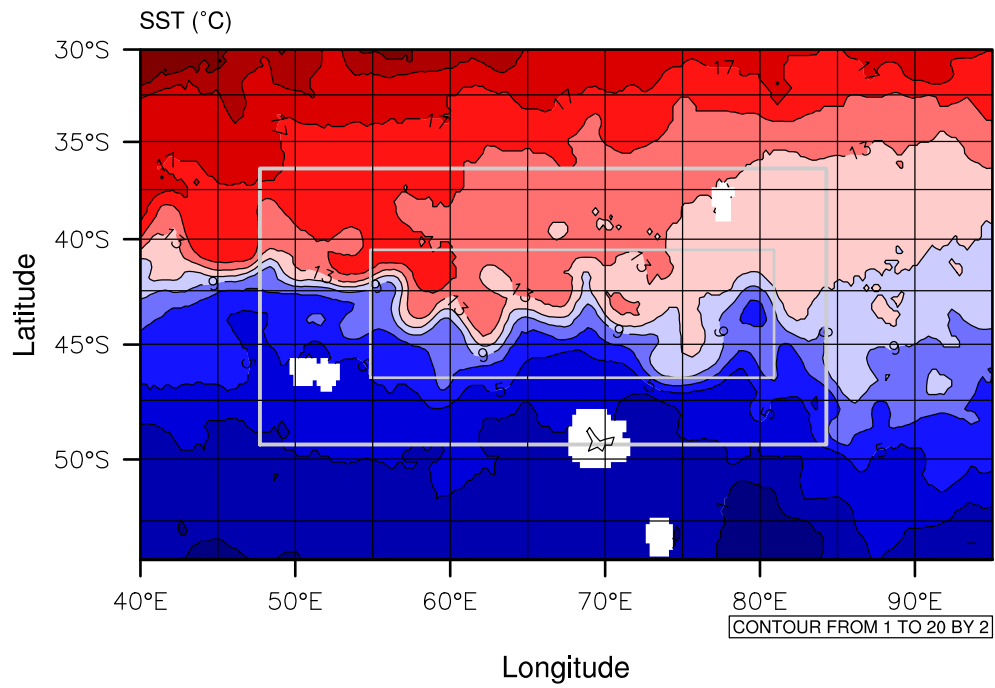


FIGURE 2.1. Map of averaged July 2002 AMSR SST. Shaded SST contours are shown in 2°C intervals. Gray rectangles denote the boundaries of the WRF simulation. Missing SST data around islands are masked white and interpolated for the aqua-planet simulation. SST contours are used as overlays in subsequent map figures.

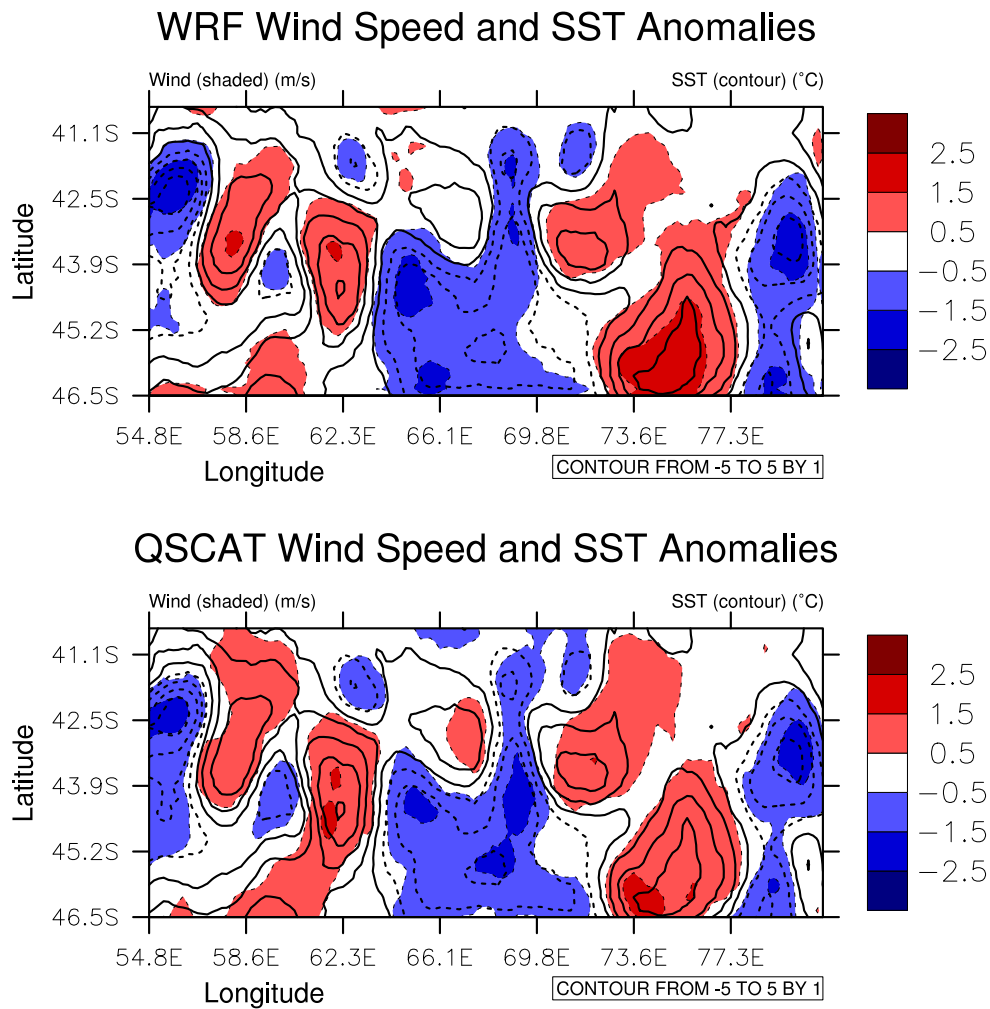


FIGURE 2.2. Comparison between WRF simulation (top) and QuikSCAT observation (bottom) averaged over the month of July 2002. Maps show inner WRF domain simulations and corresponding QuikSCAT observations of wind speed perturbations. Contours of SST perturbation are overlaid. The contour interval is 1°C.

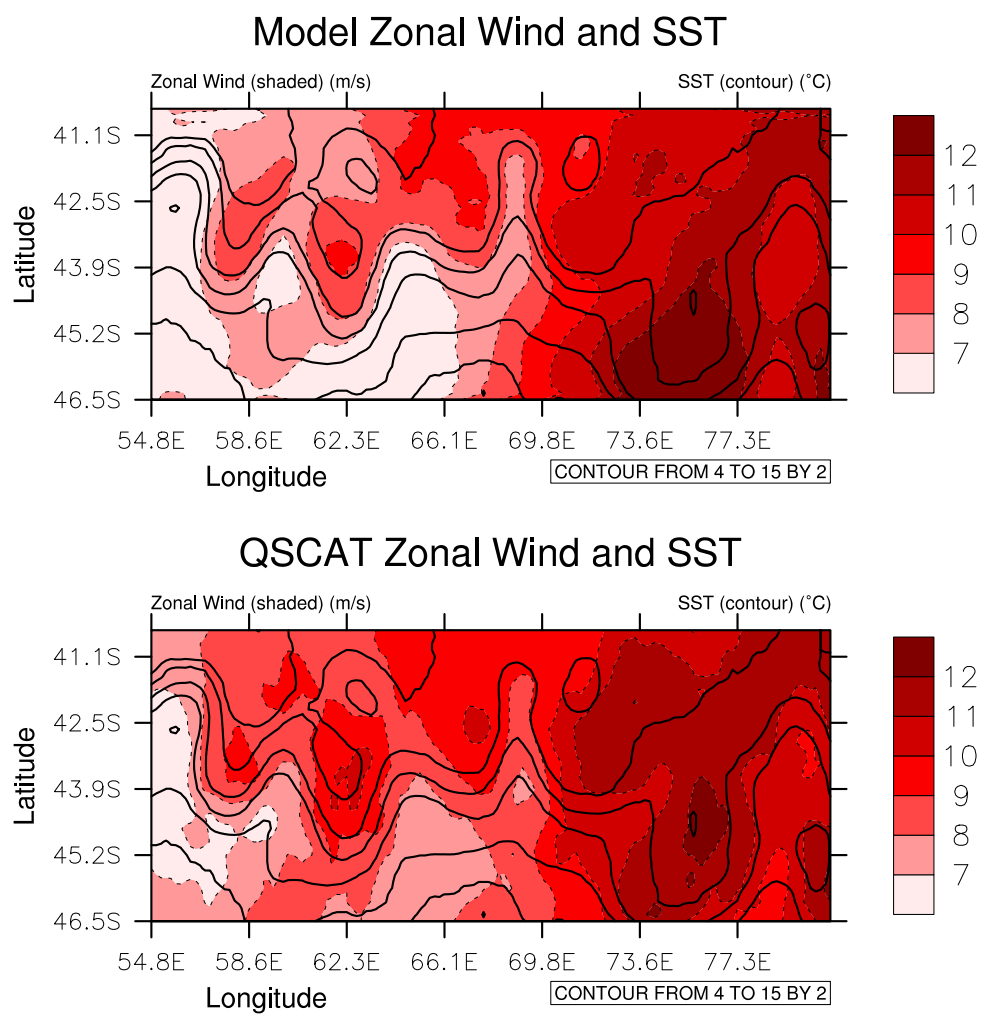


FIGURE 2.3. As in Fig. 2.2, except for zonal wind. SST contour interval is 2°C.

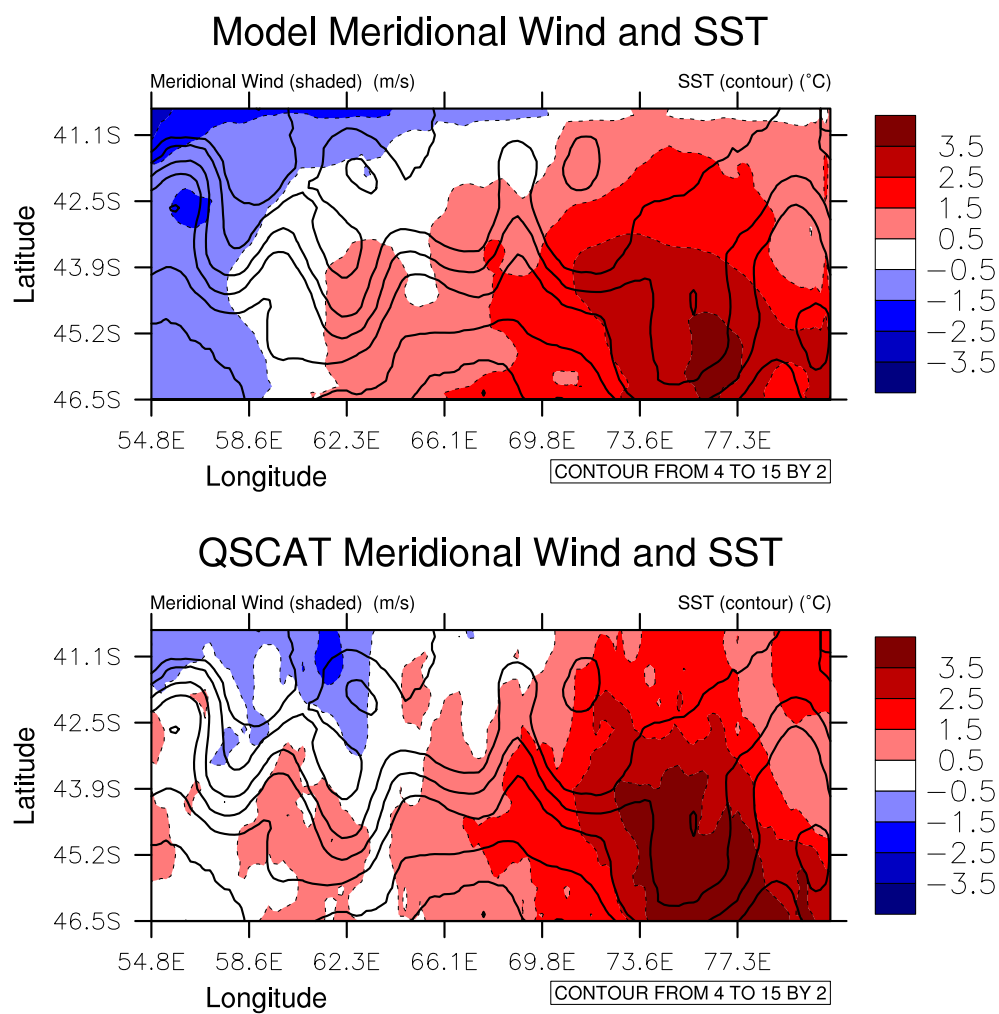


FIGURE 2.4. As in Fig. 2.2, except for meridional wind. SST contour interval is 2°C.

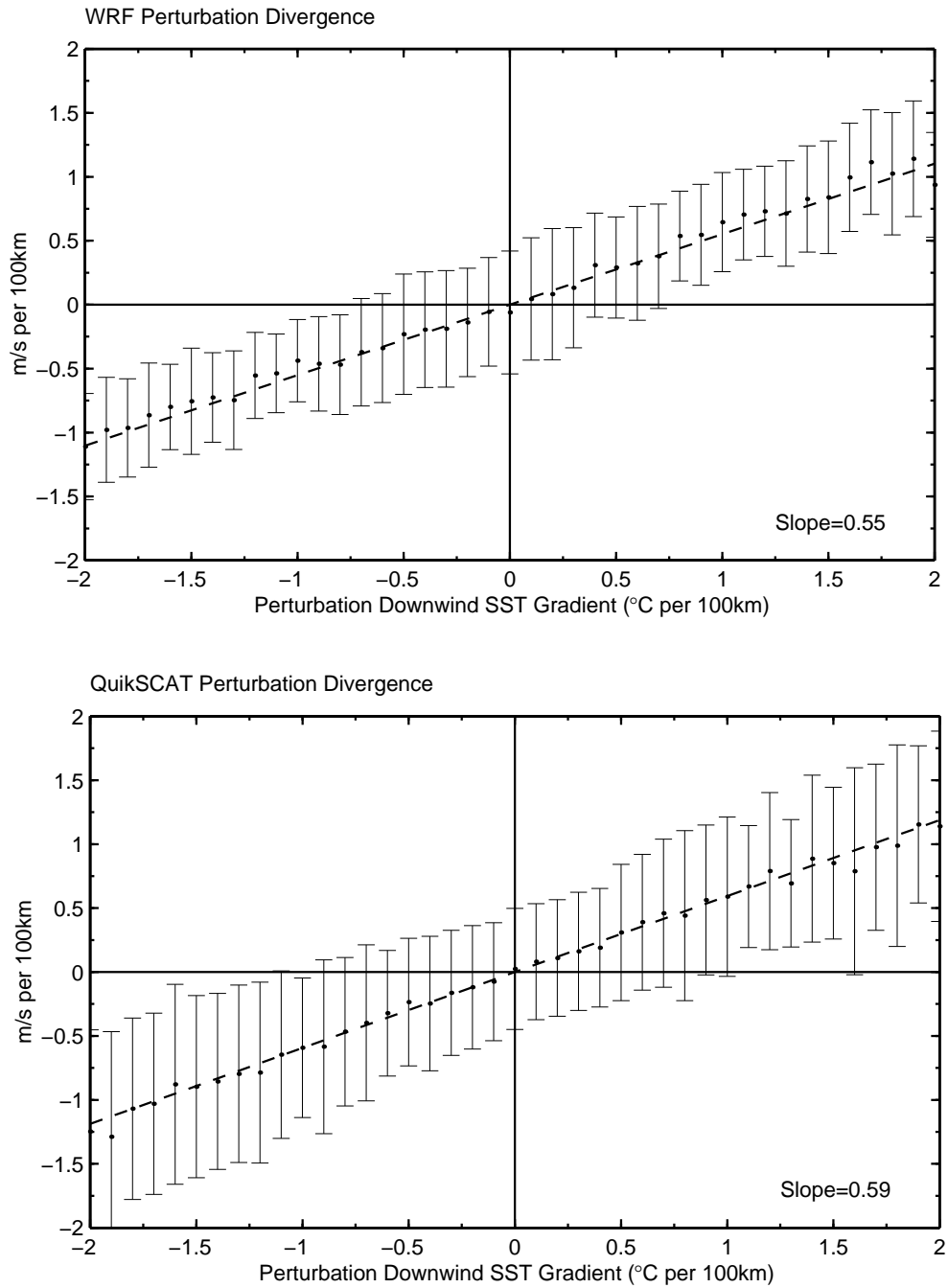


FIGURE 2.5. Binned scatterplots of the relationships between the perturbation divergence and the perturbation downwind SST gradient: (top) perturbation divergence of WRF-model and (bottom) perturbation divergence of QuikSCAT observation. The points are the means within each bin computed from 28 consecutive days, and the error bars are ± 1 std dev of the means within each bin. The lines through the points represent least square fits of the binned overall means to straight lines.

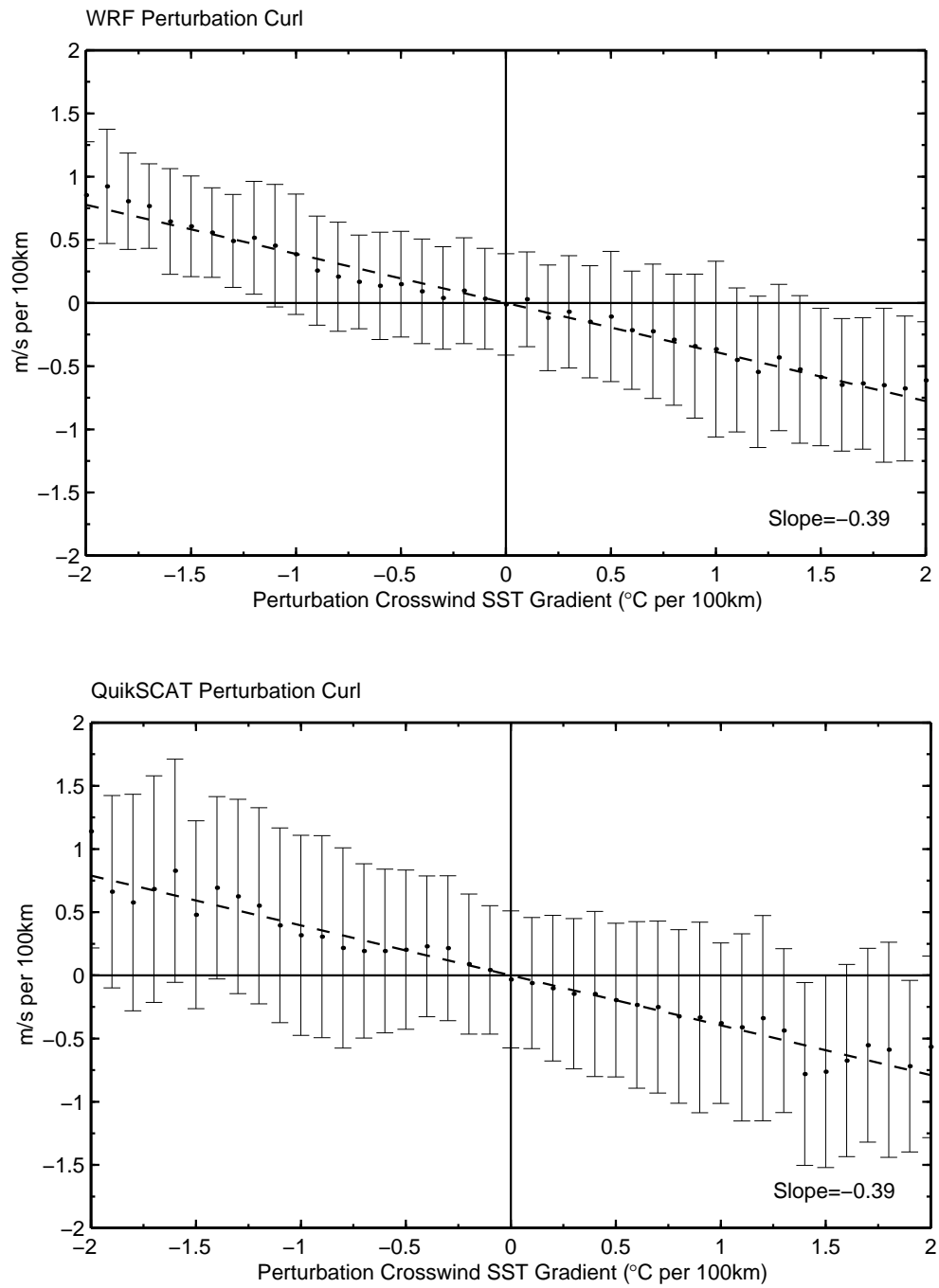


FIGURE 2.6. As in Fig. 2.5, except for the perturbation curl and the perturbation crosswind SST gradient.

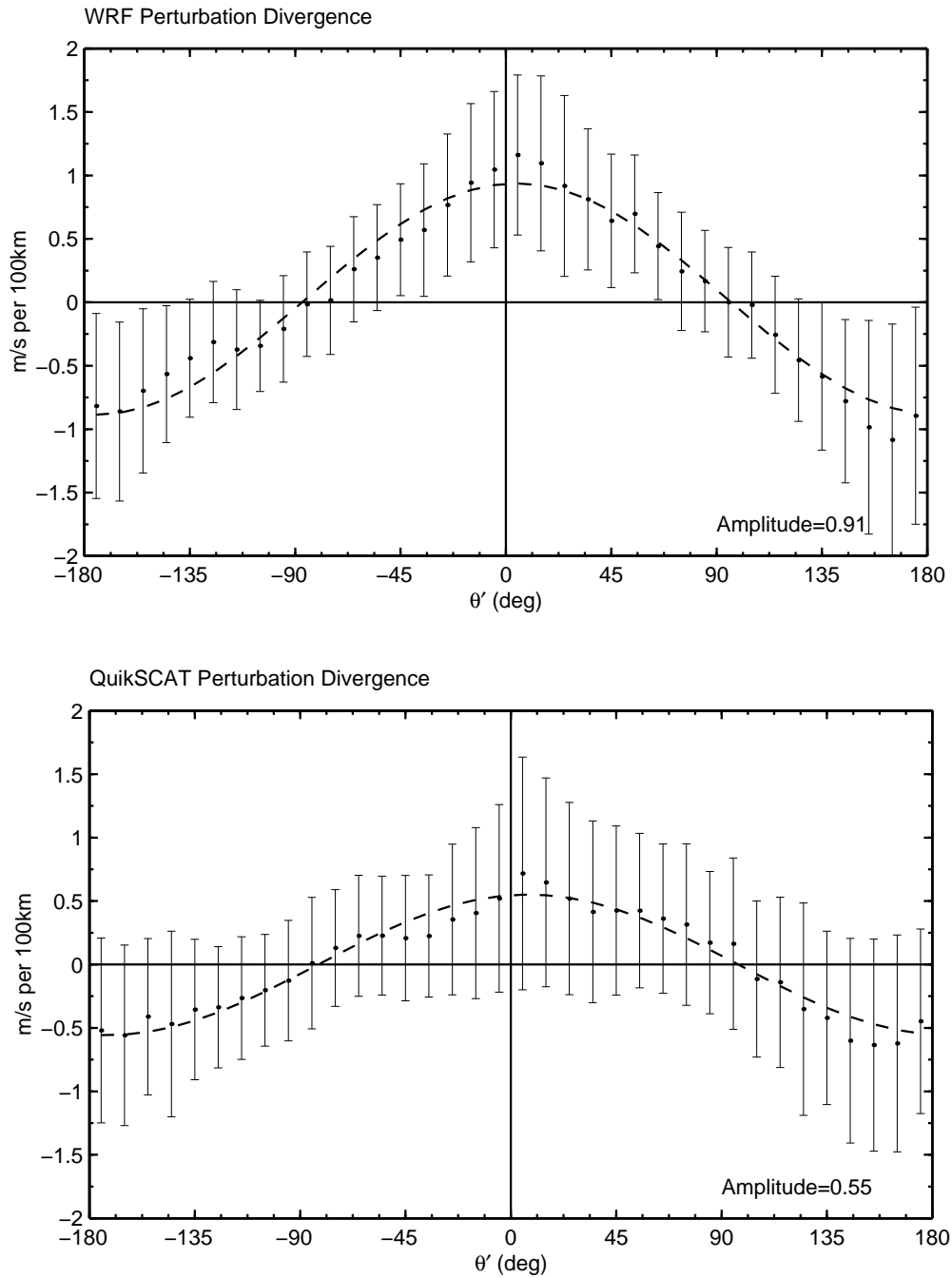


FIGURE 2.7. Binned scatterplots of the angular relationships between the wind and the SST field. Top panel shows WRF perturbation wind divergence as a function of the angle between crosswind and downwind SST gradient. Bottom panel shows QuikSCAT perturbation wind divergence as function of the angle between crosswind and downwind SST gradient. The points are the means within each bin computed from 28 consecutive days, and the error bars are ± 1 std dev of the means within each bin. The lines through the points represent least square fits of the binned overall means to a cosine curve.

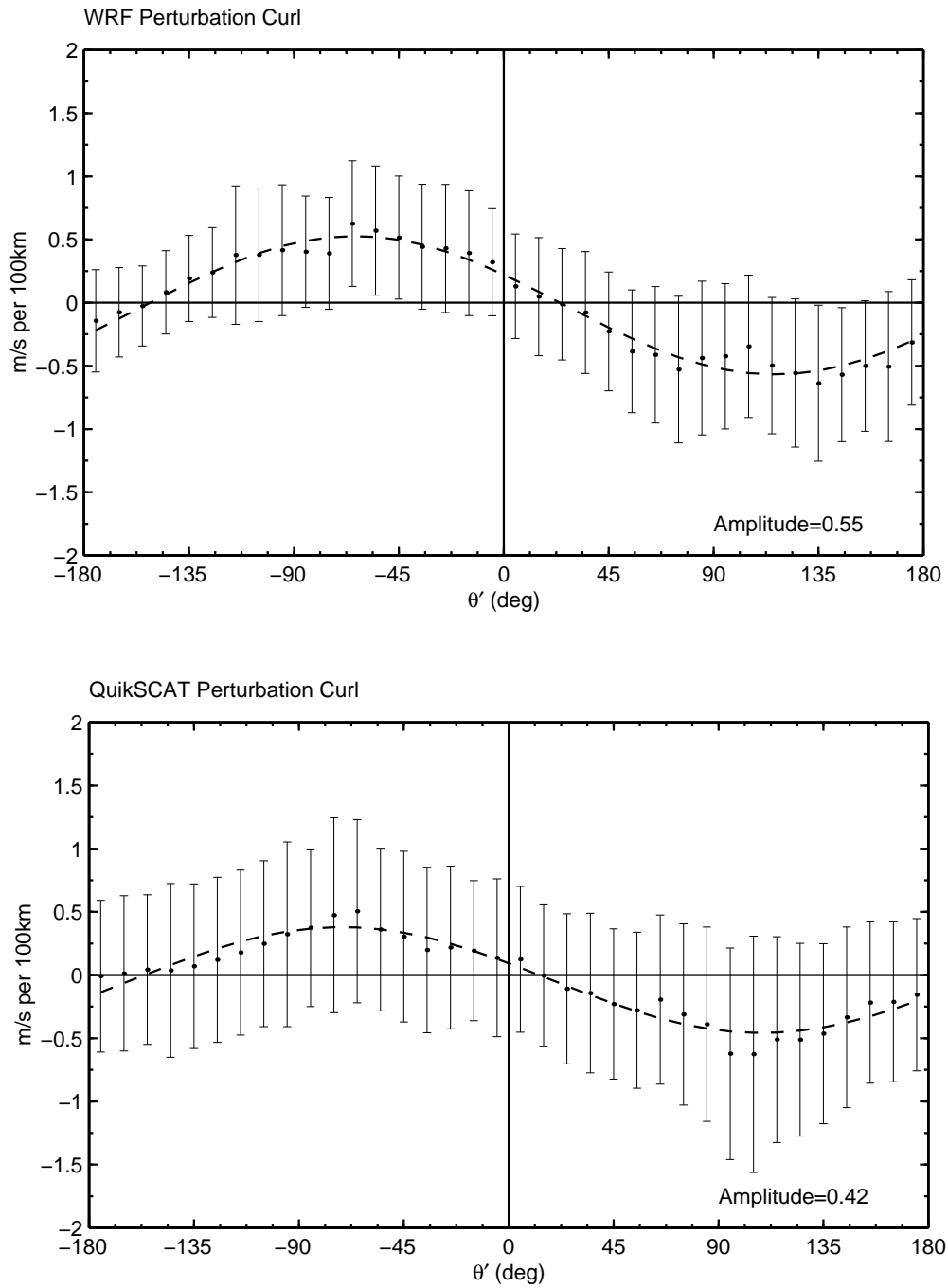


FIGURE 2.8. As in Fig. 2.7, except for the WRF perturbation curl (top) and the QuikSCAT perturbation curl as a function of the angle between crosswind and downwind SST gradient. The lines through the points represent least square fits of the binned overall means to sine.

3. ABL RESPONSE TO MIDLATITUDE SST FRONTS

In this chapter we perform a set of numerical experiments to examine the response of the atmospheric boundary layer (ABL) to mid-latitude sea surface temperature (SST) fronts. Recent observational studies have established that small scale ($\approx 10\text{--}1000$ km) SST variations are positively correlated with surface wind variations. The correlation has been documented for the northeast Pacific equatorial front through in situ measurements (e.g., Wallace et al. 1989, Hashizume et al. 2002). Analyses of satellite observations in numerous regions of the world's ocean (see review by Chelton et al. 2004) have documented that the near-surface divergence is a linear function of the SST gradient and that the coupling coefficients are surprisingly constant over the world's ocean where strong SST gradients persist.

Several numerical experiments have been performed to interpret the observations (de Szoeke 2003, Small et al. 2003, Samelson et al. 2006) with somewhat contradictory results. Depending on the scale of the SST anomalies, every term of the momentum budget that represents an important process in the surface wind–SST coupling has been used to explain the mechanism. Mahrt (1972) noted that for southerly flow across the Equator with non-zero zonal component, the zonal wind component just north of the Equator is opposite to the northern hemisphere Ekman balance and thus accelerates the flow. On time scales of one month and longer, Lindzen and Nigam (1987) suggested that hydrostatic pressure adjustments with positive pressure perturbations over cold water and negative pressure perturbations over warm water generate near-surface pressure gradients that would accelerate the flow. Near the Equator such a pressure gradient would generate strongest winds over the SST front in contrast to the observations. Small et al.

(2005) overcomes this discrepancy by arguing that the slowly adjusting air temperature shifts the pressure adjustment downstream, therefore generating largest wind speeds over the warmest water and vice versa. Yet another group of explanations emphasizes the importance of vertical divergence of turbulent momentum flux. Sweet et al. (1981) and Wallace et al. (1989) argued that a stability-induced increase in the vertical turbulent mixing of horizontal momentum downward increases the near surface velocity over warm water. Over cool water, increased stability reduces vertical mixing and the surface velocity decreases while the flow aloft accelerates. This mechanism was also used by de Szoeke and Bretherton (2004) to explain the results of their LES simulation. An observational study by Mahrt et al. (2003) over the Gulf stream finds evidence for stability-induced vertical momentum mixing. On small scales of less than 10 km, they found that strong southerly momentum is mixed down surface below the 33 m flight level and plays a role in rotating the flow over the the warm side of the Gulf stream.

Samelson et al. (2006), on the other hand, noted that the boundary layer average flux divergence $(\tau_s - \tau_h)/H$ is constant for steady conditions with constant pressure gradient forcing and no entrainment stress at the top of the boundary layer. Under these conditions the surface stress and hence the surface wind speed changes with changes in the depth of the boundary layer H . Samelson et al. (2006) assumed no entrainment stress for simplicity, but Stevens et al. (2002) and others have found that entrainment mixing of ABL air with the free atmosphere is an important process in the time averaged ABL momentum budget.

The complexity of surface wind adjustments in the vicinity of real world SST variations, in combination with undersampling of the ABL vertical structure by satellite and in situ instruments, make it difficult to isolate the governing physical processes. Numerical simulations of the ABL flow over idealized SST fronts

provide the possibility of identifying the governing ABL adjustment mechanisms with the objective of interpreting ABL response in more realistic conditions. To be useful, a simulation must simultaneously resolve the complex vertical structure of the ABL adjustment in the vicinity of the front while covering a spatial domain large enough to simulate the important physical processes already mentioned such as pressure adjustments and zonal advection. De Szoeke and Bretherton (2004) took a Lagrangian approach using an eddy resolving large eddy simulation (LES) column model with prescribed large-scale time-varying conditions of underlying SST, large-scale pressure gradients and overlying free atmosphere temperature and humidity to advect the 3 km cubic domain across the Equator near 95° W. They found that the vertical wind structure and surface wind in their model agrees well with the vertical mixing effect of Sweet et al. (1981) and Wallace et al. (1989). They also noted that, due to the model design, differential advection at different heights is not simulated. Moreover, because the horizontal pressure gradient force driving the LES model is prescribed, de Szoeke and Bretherton (2004) are unable to determine the role of meso- and synoptic scale pressure adjustments.

Small et al. (2003, 2005) used a finite difference numerical model to simulate a large domain in the eastern tropical Pacific of roughly 30° latitude \times 30° longitude, but with limited vertical resolution of 12 levels below 800 hPa. They conclude that a lagged pressure adjustment can explain surface wind acceleration in the vicinity of the equatorial SST front but note that modeled acceleration of surface wind near the front is too small. Although they did not find any evidence for the Wallace et al. mechanism in their simulations, they note that aircraft observations during the EPIC field program (Raymond 2004) show anomalous turbulent momentum flux convergence that could increase surface wind acceleration to the observed levels.

Another LES-type simulation is presented in Samelson et al. (2006) for the flow of a shallow boundary layer across an SST front. They conclude under the condition of a constant pressure gradient across the SST front that the change in vertical momentum mixing cannot accelerate surface wind and that a deepening of the boundary layer is responsible for the increased surface stress.

Because of the various model designs and setups, previous numerical simulations are unable to depict all essential processes simultaneously. These studies tend to favor one mechanism while not being able to exclude others. This study overcomes these deficiencies by adopting a mesoscale numerical model with high vertical resolution. This simulation uses a total of 69 levels on a stretched vertical grid. The lowest model layer is at 22 m with more than 30 levels in the lowest 1500 m. The model allows for simulation over a large-scale domain and also resolves differential horizontal advection of momentum and heat in shallow layers near the surface.

3.1. Simulations with idealized SST fronts

This section describes two basic model simulations which use simplified bottom boundary conditions to study the marine boundary layer response to mid-latitude sea surface temperature (SST) fronts. The simulations are performed using the WRF-model with the Grenier-Bretherton ABL scheme (GB01, detailed discussion can be found in Section 2.1.1). The lateral boundary conditions of the WRF-model outer domain along 42° E and 88° E and between 33° S and 57° S are prescribed by an aqua-planet version of the global circulation Community Atmosphere Model (CAM) (Fig. 3.1). The CAM simulations were performed by Eric Maloney (Oregon State University) with forcing by steady, latitudinally varying SST over the hypothetical ocean-covered planet and time-invariant solar radiation. The symmetric SST pattern eliminates the influence of the land mass distribution and generates nearly symmetric time-averaged meteorological fields about the meteorological equator. We chose an arbitrary 30 day time period after the three year spin up to initialize and to calculate time-dependent lateral boundary conditions for the WRF-model simulations. At the initial time of the WRF simulation the SST distribution was modified to include an SST-front extending in the north-south direction (Fig. 3.1). Two simulations were performed. The SST-front consists either of a positive 4 K change or a negative 4 K change over a distance of approximately 0.5° longitude. The sign of the SST change across the front is the only difference between the two simulations. Therefore, any difference in the response between the two simulations must be directly related to the SST change. Experiments with east-west SST-fronts were also considered but abandoned for practical reasons. Our strategy of analyzing the anomalies associated with the SST-front could not be applied to the east-west cases. It is difficult to

partition the time-averaged response to a mesoscale south-to-north SST gradient into its large-scale and mesoscale components. Large scale effects would most likely dominate the small scale adjustments and the small frontal anomalies would be absorbed into the adjustment of the mean background flow.

The use of a high vertical resolution numerical weather prediction model overcomes limitations of the previous numerical studies. For practical reasons Large Eddy Simulation (LES) modelers have found it necessary to prescribe pressure distributions and to place the upper boundary below the tropopause. These practical limitations artificially suppress the response of the pressure field to differential heating and prevent dynamical adjustments of the pressure and wind fields. Regional Climate Models (RCM) and Global Circulation Models (GCM) allow for differential heating and pressure adjustment. However, the finite difference numerical models that have been used thus far have been limited by the vertical resolution which is crucial for studies of boundary layer processes.

This WRF-model simulation overcomes some of the limitations of previous regional finite difference numerical simulations by increasing the vertical resolution in the boundary layer in combination with the use of a state-of-the-art boundary layer scheme. The boundary layer scheme is a layer-orientated vertical turbulent mixing scheme that allows for multiple vertically stacked turbulent layers (Bretherton et al. 2004). Changes in SST are communicated throughout the atmosphere in the inner domains of the model. Far away from the region of interest at the boundaries of the outermost domain, the model is constrained to match the results from global aqua-planet simulations. This provides the ideal test environment for simulations of various midlatitude SST distributions.

We believe that the ABL adjustment mechanism depends on the scale of the SST anomaly. Previous numerical simulations (e.g., Small et al. 2003,

Hafner and Xie 2003, Small et al. 2005) have relied on observed SST distribution that contain a broad range of SST gradients on scales from 50 km to 1000 km which potentially underestimate sharp SST gradients similar to the ones observed by Mahrt et al. 2004 and de Szoeke and Bretherton (2005). Consequently, the previous regional model results might not contain the small scale ABL response to sharp SST gradients. From our numerical simulations of step-like SST-fronts, we extend the wavenumber cut-off to larger values. We hope to simulate the small scale response of the ABL to sharp SST gradients and to predict the magnitude of the pressure gradient changes associated with the SST change as well as the phase relation of the pressure anomaly relative to the SST-front.

The initial fields and boundary conditions were provided by Eric Maloney from an integration of the Community Atmosphere Model version 2 (CAM2). The simulation represents the general circulation over an ocean-covered planet with meridionally symmetric SST and radiation. The CAM2 SST boundary condition is time invariant and the latitudinal structure is represented by a smoothed cosine-fit of observed zonally-averaged SST from the Advanced Microwave Scanning Radiometer (AMSR). The SST for the regional WRF simulation is derived from the aqua-planet simulation by altering only the lower boundary condition of the SST distribution. In the first experiment (hereafter denoted by P4 or “plus 4K”) the background SST is increased by 4 K from approximately the middle of the high resolution inner-most domain to simulate a step increase in SST in the east-west direction, and creating, thereby, a north-south SST front through the center of the domain (Fig. 3.1). Similarly, for the second experiment (hereafter denoted by M4 or “minus 4K”), the background SST is decreased by 4 K to simulate a negative north-south SST front. The orientation of the SST front is almost perpendicular to the prevailing west-northwest background wind and the two experiments therefore

simulate cold-to-warm (P4) and warm-to-cold (M4) transitions. The outer WRF domains cannot resolve the sharpness of the SST front, creating a mismatch at the boundaries. In addition, there is an SST front created at the outer boundary of the WRF domain where the perturbed SST values are blended with those used in the CAM2 simulation. However, the boundaries of the outer domain are far away from the inner domain’s SST front and most of the inconsistency is absorbed by a numerical “sponge layer” at the edge of the outer domain.

We will see that both simulations M4 and P4 show large responses in the atmospheric boundary layer. The response is not linear, and this asymmetry between the cold-to-warm response and warm-to-cold response indicates that adjustment mechanisms may differ in the M4 and P4 simulations. The results of each experiment are described in the following two sections and are compared in the section thereafter.

We will show that the region of the largest response occurs in a relatively narrow transition region over and just downstream from the largest SST gradients. In this region, the flow is adjusting rapidly towards the balanced state found in the far-field, away from the region of strong SST gradient. The flow in the far-fields is in an Ekman balance between pressure gradient force, Coriolis force and turbulent stress convergence. The flow across the SST gradients changes the depth of the boundary layer. A deeper boundary layer and stronger wind speeds are found over the warmer water and a shallow boundary layer and weaker wind speeds are found over the cold water in the far-fields (compare with Samelson et al. 2006). In the narrow SST region, the ABL adjusts to the rapidly changing conditions. There are however qualitative and quantitative differences in the adjustment mechanisms of P4 and M4 in the transition zone.

3.1.1. Methodology

We use 30-day simulations of the regional mesoscale WRF-model to examine the ABL responses to positive and negative step changes in SST. The lateral boundary conditions for the WRF-model are taken from a single CAM2 simulation over a symmetric aqua-planet after a 3-year spin-up period.

We now introduce some terminology that will facilitate the discussion of the P4 (Section 3.2) and the M4 (Section 3.3) experiments. The change in SST occurs over a distance of approximately 0.5° longitude and remains constant thereafter. The area between 60.5° longitude and $61.^\circ$ longitude will in the following be referred to as the SST front or the frontal region. The width of the frontal region was limited by the resolution of the model's finite difference scheme. It was our intent to make the frontal region as narrow as possible to study the ABL response to a "step" change in SST. Several experiments were performed to estimate an 'effective resolution' of the model. The horizontal finite difference scheme of the WRF-model produces a computationally stable ' $2\Delta x$ ' oscillation due to spatial undersampling as the front width approaches the grid spacing. The width of the SST front was therefore chosen to be as narrow as possible while suppressing the computational mode. The functional form of the step change in SST is given as a hyperbolic cosine function. The sharp SST front can be well resolved with by a minimum of 6 grid points in longitudinal direction. The wind direction is consistently from the west-northwest, and therefore the wind direction is almost perpendicular to the SST front. Short periods of easterly surface winds due to synoptic variability were found during the 30 day run. The flow of boundary layer air during these periods opposed the prevailing direction relative to the SST-front. Although including these periods did not alter the time-averaged mo-

momentum budget results qualitatively, the inclusion complicated the analysis and obfuscated the results. As will be discussed in section 3.4 where the P4 and the M4 are compared, physically different mechanisms are present for cold-to-warm and warm-to-cold SST fronts. The simplest and most effective way to avoid the complication is to exclude the periods of reversed wind direction from the analysis.

From the meridionally averaged longitude-height cross-sections for the P4 experiment (Figs. 3.7 – 3.12) and from the M4 experiment (Figs. 3.19 – 3.24) it becomes apparent that most of the adjustment of the ABL takes place in a relatively narrow transition zone about 100 km wide beginning near the upstream frontal boundary and extending slightly further than the downstream frontal boundary. The magnitude of the zonal momentum advection term (Figs. 3.5, 3.18) can be used to characterize the regions of strong and weak adjustment and to separate the model domain into three regions (Fig. 3.6). Upstream and away from the SST front, the momentum advection is approximately zero and longitudinal changes in meteorological variables are small. This region is in Ekman balance and therefore is referred to as the “equilibrium region”. Near and just downstream from the SST front, advection is a dominant term in the momentum balance and the atmosphere is adjusting rapidly to the increase of SST. This region is hereafter called the “transition region” or “advection region”. Advection becomes negligible again downstream of the transition region. However, the atmosphere is still not in balance and continuing adjustments are taking place, although at a much slower rate compared to the transition region. This third region found downstream of the transition region is called the “quasi-equilibrium” region. The region is nearly in Ekman balance but thermodynamically driven pressure adjustments are still taking place. Each of these regions will be separately discussed for the P4 and M4 experiment in sections 3.2 and 3.3, respectively.

An important characteristic of the boundary layer is its depth H . Traditionally, the boundary layer depth is thought to be the height above the ground where the direct influence from the surface vanishes. The GB01 ABL-scheme calculates a boundary layer depth based on the buoyancy frequency of the layer. The parameterization identifies the top of the convective layer as the location where $(N^2 l^2)_{layer} \geq -0.5(N^2 l^2)_{avg}$, where N is the buoyancy frequency, l is the turbulent length scale, and the subscript “avg” indicates an average over all convective layers below a given layer indicated by subscript “layer” (Grenier et al. 2001). This ABL scheme predicts very shallow boundary layers in stable conditions. In our analysis, however, we are interested in the depth of the momentum boundary layer, which can be significantly deeper in stable conditions than the buoyancy frequency definition used by GB01 would suggest. Therefore, the GB01 definition of H cannot successfully be used as the momentum boundary layer depth in all situations. An alternative definition of H as the level of zero stress is also deficient because we wish to analyze the *averaged* as opposed to *instantaneous* momentum budgets. There is a difference between 1) averaging the stress first and then calculating H and 2) calculating H for each observation and subsequently averaging the individual heights. To illustrate this difference, assume H to be the level where stress becomes negligible and imagine two instances, one where the stress vanishes at 500 m and one at 1000 m. Averaging the individual heights results in an average boundary layer depth of 750 m. However, the averaged stress will have significant values above 750 m (in this simple case exactly 1/2 of the 1000 m deep boundary). Estimating H from the averaged stress would therefore result in a boundary layer deeper than 750 m. Large variability of the boundary layer depth can increase the discrepancies. The simple example also shows that in order to obtain a height closer to 750 m from averaged stress profiles, one needs to choose

larger-than-zero values of the stress to define a consistent averaged boundary layer depth.

Instead of identifying H by defining a stress threshold level, we use a threshold value for stress convergence \mathfrak{S}_H to find the depth of the averaged boundary layer. To obtain a meaningful value of \mathfrak{S}_H from the averaged momentum budgets, we bin-average the instantaneous boundary layer depth from the ABL-scheme over the upstream region (Figure 3.2) where the variability of turbulent stress convergence is smaller than anywhere else in the domain. The maximum frequency of simulated ABL depth consistently occurs at a level of 450 m. The corresponding value of turbulent flux convergence at $H = 450$ m (\mathfrak{S}_{450}) is $2 \times 10^{-4} \text{ ms}^{-2}$ which then may be used as an indicator of the momentum boundary layer depth across the SST front. The average momentum boundary layer depth in the transition and quasi-equilibrium region is therefore found by descending from the top of the model column until a level where $\mathfrak{S} = \mathfrak{S}_{450}$ is found. Descending from the top of the model column avoids ambiguities where stress convergence changes sign within the ABL. Turbulent stress convergence of $2 \times 10^{-4} \text{ ms}^{-2}$ corresponds roughly to $1/e$ of the surface value over our model domain.

Comparing this momentum boundary layer depth to the cross section of potential temperature θ shows satisfying results. The momentum boundary layer depth of the P4 run (Fig. 3.3) lies at the top of a well mixed layer where the vertical gradient of potential temperature is small and just below a region of weakly stable θ . From its upstream height of 450 m, the boundary layer grows rapidly to about 750 m within about 50 km. In the M4 run the averaged momentum boundary layer depth can also be related to the potential temperature. The momentum boundary layer depth follows the weakly stable potential temperature in the upstream region and drops rapidly to about 200 m over the SST front and the ABL becomes very

stable. Subsequently, the boundary layer depth increases slowly along the contours of θ .

In the P4 experiment, an *internal* boundary layer can be identified. This internal layer is convectively driven by the surface buoyancy fluxes associated with large positive sea-minus-air temperature difference. At the top of the internal boundary layer, air from the more stable upper portion of the ABL is incorporated into the internal boundary layer through entrainment. The well mixed thermodynamic properties of the internal layer can be used to estimate the depth of the layer. We define the depth by the level where the vertical gradient of θ changes sign from unstable (< 0) to stable (> 0) conditions. In the M4 run, no such internal boundary layer exists because of the stabilizing effect of the decreasing SST downstream.

It is important to note that the thermodynamic boundary layer depth is relatively constant across the SST-front. In this region of the ocean, the stratification of the lower atmosphere is slightly stable with a weak inversion at around 800 m (Fig. 3.3). The virtually constant thermodynamic boundary layer depth lies above the momentum boundary layer. In large scale regions with strong convection, the momentum and thermodynamic boundary layer depth are expected to be approximately equal. For the remainder of the chapter the concept of the momentum boundary layer depth is more useful for our discussion. However, it is important to be aware of the differences between the momentum and thermodynamic boundary layer depth to avoid confusion in Chapter 4 and 5.

3.1.2. Analysis of the simulated momentum budget

The simulations contain variability on time and space scales from days to weeks. Our objective is the analysis of the average boundary adjustment that persists on time scales of a month or longer. This lowpass component is obtained by averaging over the last 28 out of the 30 days of simulation. The 2 days at the beginning of the simulation are not used to exclude the period during which the WRF-model is adding mesoscale detail to the CAM2 initial conditions and adjusting to the imposed boundary conditions. The output interval is 4 hours which gives 168 output periods spread over 28 consecutive simulation days. The momentum budget for the zonal and meridional component can be written as follows.

$$\frac{\partial \bar{u}}{\partial t} = -\bar{u} \frac{\partial \bar{u}}{\partial x} - \bar{v} \frac{\partial \bar{u}}{\partial y} - \bar{w} \frac{\partial \bar{u}}{\partial z} + f\bar{v} - \frac{1}{\rho_o} \frac{\partial \bar{p}}{\partial x} - \frac{\partial}{\partial z} \overline{\langle u'w' \rangle} \quad (3.1)$$

$$\frac{\partial \bar{v}}{\partial t} = -\bar{u} \frac{\partial \bar{v}}{\partial x} - \bar{v} \frac{\partial \bar{v}}{\partial y} - \bar{w} \frac{\partial \bar{v}}{\partial z} - f\bar{u} - \frac{1}{\rho_o} \frac{\partial \bar{p}}{\partial y} - \frac{\partial}{\partial z} \overline{\langle v'w' \rangle} \quad (3.2)$$

where the 28-day Reynolds average is denoted by an overbar. All terms in the above equations have the usual meaning, and the terms $\frac{\partial}{\partial z} \overline{\langle u'w' \rangle}$ and $\frac{\partial}{\partial z} \overline{\langle v'w' \rangle}$ denote the (Reynolds averaged) convergence of subgrid turbulent momentum flux. All other co-variance terms were found to be negligibly small compared with the major terms in the equation. $\frac{\partial}{\partial x} \overline{\langle u'u' \rangle}$, $\frac{\partial}{\partial x} \overline{\langle u'v' \rangle}$, $\frac{\partial}{\partial y} \overline{\langle v'v' \rangle}$ and $\frac{\partial}{\partial y} \overline{\langle v'u' \rangle}$ are found to be small and are omitted in Eqn. 3.1 and 3.2 for simplicity. The low-pass fields from the model are in approximate steady state and we are left with advection, pressure gradient, Coriolis, and turbulent flux convergence terms. The model response is very homogeneous in the latitudinal direction because of the assumed structure of the SST front. It is therefore possible to take an additional average in the latitudinal direction to increase the statistical stability of the results. Analysis

of the remaining terms shows that meridional and vertical advection is small compared to the other leading terms and we can rewrite the momentum budget as follows, retaining only the dominant terms.

$$0 = -u \frac{\partial u}{\partial x} + f v - \frac{1}{\rho_o} \frac{\partial p}{\partial x} - \frac{\partial}{\partial z} \langle u' w' \rangle \quad (3.3)$$

$$0 = -u \frac{\partial v}{\partial x} - f u - \frac{1}{\rho_o} \frac{\partial p}{\partial y} - \frac{\partial}{\partial z} \langle v' w' \rangle \quad (3.4)$$

The double overbars for temporal and latitudinal averaging have also been omitted for simplicity.

In the following illustrations the first three RHS-terms in Eqn. 3.3 and 3.4 are referred to as ‘advection’, ‘coriolis’ and ‘pressure gradient force (PGF)’ terms. The last term is referred to as the turbulent stress convergence term or, for simplicity, the ‘turbulence’ term. The negative value of advection can also be interpreted as acceleration and the terminologies will be used interchangeably.

3.2. Results from cold-to-warm SST front experiment (P4)

This section describes the first of two experiments to examine the response of the atmospheric boundary layer (ABL) to an idealized SST front. The SST boundary condition for this experiment includes a north-south front in the center of the inner domain (Fig. 3.1). The background SST from the CAM2 aqua-planet integration is increased by 4 K uniformly along the front to the east of 60.5° longitude. The momentum budgets of the equilibrium and the quasi-equilibrium region have similarities and will be discussed together in Section 3.2.1. The transition region will be discussed in Section 3.2.2.

3.2.1. Equilibrium and quasi-equilibrium region (P4)

The equilibrium region is located on the upstream side of the front from the western boundary of the domain to about 60.5° longitude. The quasi-equilibrium region is located on the downstream side of the SST front from about 61.6° to the eastern end of the domain. The non-equilibrium transition region between 60.5° and 61.6° longitude is discussed in Section 3.2.2. The air that enters the equilibrium region is in approximate Ekman balance and the advection term is small. The remaining terms of the momentum budget are approximately constant in the zonal direction as the air approaches the front near 60.5° . The momentum boundary layer top is nearly constant at about 450 m (Fig. 3.2). In the quasi-equilibrium region located downstream of the SST front, advection again becomes negligible and the flow has returns to approximate Ekman balance. The momentum balance in the upstream equilibrium region is consistent with the ABL model of Stevens et al. (2002). The ABL in the downstream quasi-equilibrium region is slowly adjusting to the new equilibrium condition after passing over the SST front. The changes agree with the lagged pressure adjustment mechanism found by Small et al. (2005). Air temperature (Fig. 3.3) changes at a much slower rate than the SST. Hence, the heat flux associated with the air-sea temperature difference remains large in the quasi-equilibrium region and therefore the largest pressure gradients are found there. The slow adjustment process in downstream direction is shown by the horizontal changes of zonal wind (Fig. 3.7), zonal and meridional stress convergence (Fig. 3.8) and zonal advection (Fig. 3.10). The zonal and meridional wind velocities are fairly constant at a given height (Fig. 3.7). While the zonal velocity is larger in the downstream than in the upstream region, the meridional velocity is slightly smaller in the downstream region and the elevated wind

maximum is diminished. The increase of zonal velocity is mostly near the surface which reduces the ABL vertical shear. The convergence of zonal and meridional turbulent momentum flux (Fig. 3.8) show the adjustment of the ABL towards Ekman balance for a deepening boundary layer. In the quasi-equilibrium region, the values of zonal turbulent flux convergence are larger than in the equilibrium region. In equilibrium conditions, momentum advection is small and vertically uniform. The vertical structure (see also Fig. 3.30) shows a balance between of coriolis, advection, turbulence and an increasing PGF term. Therefore, zonal turbulent flux convergence is adjusting to the environment for at least 100 km after passing the SST front. The meridional turbulent flux convergence term decreases in the quasi-equilibrium region, but it also shows signs of continued adjustment. The corresponding turbulence term (Fig. 3.9) shows larger values at a given level in the downwind region and generally higher values over the warmer SST. As expected, the meridional stress vanishes near 200 m in the core of the elevated meridional wind maximum. Meridional stress increases in the downstream region below the elevated wind maximum. Higher levels show only small changes of meridional stress.

In the equilibrium region, the ratio of surface stress to boundary layer height is approximately constant, consistent with the arguments of Samelson et al. (2006). In the upstream region $\tau_s/H = 4.3 \times 10^{-4} \text{s}^{-1}$ while in the downstream region $\tau_s/H = 4.1 \times 10^{-4} \text{s}^{-1}$ (Fig. 3.14). This is remarkable, given the 3-dimensional character of the experiment and the fact that the pressure gradient changes in the vertical and across the SST-front.

The air temperature increases much slower than the underlying SST. The maximum air-sea temperature difference and largest sensible heat flux are therefore found downstream of the SST-front. A similar response was observed by

Thum et al. (2002) in the equatorial Pacific north of the cold tongue where temperature advection shifts the location of the largest heat flux downwind to the north of the strongest SST gradients. Since the surface buoyancy and temperature advection are large contributions in the thermodynamic equation, the pressure perturbation is lagged relative to the SST (Fig. 3.11). The resulting zonal pressure gradient force (Fig. 3.11) is larger in the downstream region and slowly increases to the eastern edge of the domain. The meridional pressure gradient force is mostly determined by the large scale pressure distribution that has a meridional gradient nearly 5 times larger than the zonal component.

Turbulence kinetic energy (TKE) (Fig. 3.12) in the upstream region is maximum where the shear of zonal and meridional wind is maximum, just below the elevated meridional wind maximum. Larger values of TKE are found in the downstream region where two TKE maxima are observed, one near the surface due to buoyancy production (Fig. 3.13) and one just above the internal boundary layer. The vertical structure of TKE agrees well with the findings of de Szoeke and Bretherton (2004) although the pattern of TKE from the WRF simulation is smoother, possibly because of the long time-averaging period.

Generally, the difference between the upstream and the downstream equilibrium region is most pronounced below 200 m. This observation is another indication that the vertical resolution near the surface is important.

3.2.2. Non-equilibrium transition region (P4)

The rapidly changing SST in the frontal zone drives significant changes in the structure of the mean fields and turbulence in the ABL, both horizontally and vertically. The zonal momentum budget is not in Ekman balance. The part of

the boundary layer below 200 m experiences an acceleration over the SST front (Fig. 3.10). The acceleration is maximum near 61° longitude slightly downstream of the strongest SST gradient. From this point, the near-surface acceleration gradually decreases, becoming insignificant at about 61.6° longitude which marks the beginning of the quasi-equilibrium region discussed above. The acceleration is strongest near the surface and confined vertically to below 200m. In an almost complementary pattern to the acceleration, the zonal turbulent flux convergence decreases significantly in magnitude below 200m and changes sign near the surface at around 61° longitude (Fig. 3.8). The sign change of the stress convergence is also found in observational data during EPIC 2001 C130 flights over the equatorial SST front (Small et al. 2005, their Fig. 13c) and is similar to the LES model results of de Szoeke and Bretherton (2004). The negative values aloft are slightly shifted downstream relative to the near-surface positive values.

The values of the pressure and Coriolis terms in this region rapidly approach their values in the downstream equilibrium region, but the changes in magnitude are much smaller compared to the advection and turbulence terms, especially near the surface.

3.2.3. ABL average and surface momentum budget (P4)

As a result of the vertical dipole structure of the zonal turbulent stress, the ABL-averaged momentum budgets (Fig. 3.15) are significantly different than the near-surface momentum budgets in the transition region. The ABL-averaged budget shows that the zonal and the meridional flow is close to Ekman balance with relatively small accelerations in the zonal direction. The zonal and meridional residual from the sum of advection, PGF, coriolis and turbulence terms

are denoted as X and Y , respectively. The zonal residual X and the meridional residual Y can be interpreted as the sum of effects from entrainment, changes in boundary layer depth and other subgrid-scale mechanisms such as the effects of shallow convection on the ABL-averaged momentum budget. The residuals become significantly less than zero in the region where the boundary layer deepens, consistent with the notion of entrainment by changes in the boundary layer depth. In the simplest form, entrainment may be parameterized following Stevens et al. 2001 who use a bulk entrainment to define the stress at the top of the momentum boundary layer

$$\tau = w_e \Delta \mathbf{U} = w_e (\mathbf{U}_T - \mathbf{U}) \quad (3.5)$$

where w_e is the entrainment velocity and \mathbf{U}_T is the vector wind above the ABL. Note that the residuals X and Y and entrainment have opposite signs due to the definition of X and Y as a residual. Changes in pressure gradient force are compensated by changes in the Coriolis term.

In contrast, the surface momentum budget (Fig. 3.16) is highly ageostrophic in the transition region. The dominant balance of the zonal budget is between the advection and stress convergence terms. This zonal and meridional force balance is most easily observed in vector form (Fig. 3.17). Near the surface, the vector of turbulent stress convergence rotates clockwise where zonal advection becomes important. For a brief period, the zonal component of the turbulent stress vector is pointing in the direction of the zonal wind. In the transition region, turbulent stress convergence decreases, and in parts of the transition region, momentum stress convergence is accelerating the flow. The changes in the PGF and Coriolis terms are relatively small. The meridional surface budget terms are

larger in magnitude but the transition zone changes are smaller. The vertically integrated ABL seems to adjust more geostrophically than the near-surface layers.

3.3. Results from warm-to-cold SST front experiment (M4)

The M4 experimental setup is similar to the P4 simulation; only the SST boundary condition changes. Instead of a positive 4K change, the sea surface temperature is decreased by 4 K in the eastern part of the domain to examine the adjustment of the ABL to decreasing SST. The prevailing wind direction is now towards decreasing SST. As in P4, short periods with easterly wind directions are removed from the average, although no qualitative changes were found when retaining the entire record. The transition zone is now characterized by the sudden collapse of the momentum boundary layer to below 200 m with a subsequent slow deepening to around 230 m in the downstream quasi-equilibrium region. We again divide the domain into upstream equilibrium, transition, and downstream quasi-equilibrium regions based on the importance of the advection term (Fig. 3.18). The locations of the boundaries of the transition region are similar in the two experiments. In the M4 experiment, the downstream boundary of the transition region has moved slightly upstream, making the transition region slightly smaller in the M4 experiment.

3.3.1. Equilibrium and quasi-equilibrium region (M4)

The location of the equilibrium region boundary in M4 coincides with that of the P4 run. The quasi-equilibrium region, however, begins about 0.4° of longitude closer to the SST-front near 61.2° longitude. The decrease of ABL height between the upstream equilibrium and the downstream quasi-equilibrium region

is more than 200 m, essentially a collapse of the initial convectively driven momentum boundary layer. Higher zonal velocities are observed in the equilibrium region compared to the quasi-equilibrium region (Fig. 3.19). The differences between equilibrium and quasi-equilibrium region are most pronounced near the surface where the zonal wind decreases by 3 ms^{-1} . In the horizontal, there is very little zonal wind speed change within each region. The meridional velocity shows an increase in the elevated wind maximum in the quasi-equilibrium region. The near-surface northerly meridional wind becomes stronger by about 1 ms^{-1} . The vertical shear for both meridional and zonal wind increases in the quasi-equilibrium region. The vertical convergence of zonal turbulent stress (Fig. 3.20) is almost identical in the equilibrium and quasi-equilibrium regions. However, meridional stress convergence is significantly larger in the quasi-equilibrium region. The decrease of zonal turbulent stress (Fig. 3.21) in the quasi-equilibrium region reflects the deceleration of zonal wind compared to the equilibrium region. The zonal advection (Fig. 3.22) is small above the boundary layer in the quasi-equilibrium region. However, in the layer that was detrained from the boundary layer there is negative advection which is consistent with the notion that the detrained air is able to accelerate freely until a new momentum balance is established (de Szoeke and Bretherton 2004). The meridional advection term is larger in the quasi equilibrium region, which is related to the strengthening of the elevated meridional wind maximum. The cooling of the air over the cooler SST leads to hydrostatic increases in pressure in the quasi-equilibrium region and the zonal pressure gradient (Fig. 3.23) changes accordingly with most significant changes in the boundary layer. The meridional pressure gradient is mostly controlled by the large-scale forcing. Turbulence kinetic energy has a similar structure in the upstream and downstream equilibrium regions. The maximum in TKE is found in

the lower third of the boundary layer. The ratio of surface stress to boundary layer height is not equal in the equilibrium and quasi-equilibrium region (Fig. 3.25). In the upstream region, we find τ_s/H to be $4.5 \times 10^{-4} \text{s}^{-1}$, while in the downstream region this ratio is closer to $\tau_s/H = 5.6 \times 10^{-4} \text{s}^{-1}$. The increase in τ_s/H between the equilibrium and quasi-equilibrium region can be explained by the increase in pressure gradient which should translate into higher surface winds. This indicates that changes in surface pressure across the SST front are important.

3.3.2. Non-equilibrium advection region (M4)

The transition region is characterized by the sudden collapse of the boundary layer as the SST begins to decrease. The most significant changes in zonal surface wind (Fig. 3.19) are observed in this region. The changes at a constant elevation within the upper part of boundary layer are much weaker. The meridional wind remains virtually constant horizontally and vertically. The momentum boundary layer collapse is most easily observed in the longitude-height cross-sections of zonal turbulent flux convergence (Fig. 3.20), which is confined to a very shallow layer. The meridional flux convergence increases toward the surface without reaching an extremum. The zonal stress (Fig. 3.21) decreases rapidly while meridional stress only decreases slightly. The decrease of zonal momentum (Fig. 3.22) is observed only below 100 m. The meridional advection in this region shows only small differences from the upstream and downstream regions but is decelerating in the transition zone. No sudden changes in the pressure gradient response can be observed (Fig. 3.23). However, the zonal pressure gradient decreases faster in the boundary layer than above. At a given height within the boundary layer, turbulence kinetic energy decreases and is fairly homogeneous

almost throughout the entire boundary layer. The fact that the ratio of surface stress to boundary layer height is not constant (Fig. 3.25) is an indication that the boundary layer height in the transition region is either overestimated or that other processes in the transition zone are of equal importance.

3.3.3. ABL average and surface momentum budget (M4)

The boundary layer averaged momentum budget (Fig. 3.26) shows that the integrated boundary layer flow is approximately in Ekman balance in the transition zone. The change of the zonal pressure gradient is mostly balanced by a change in Coriolis force and a small reduction of turbulent stress. The residual of Coriolis, advection, turbulent stress convergence and pressure gradient force is interpreted as a detrainment process and is positive in accordance with the decrease in boundary layer height. The change of the Coriolis force across the SST-front is similar in the surface (Fig. 3.27) and the ABL-average (Fig. 3.26) momentum budgets. The similarity between surface and ABL-average is also found in the PGF term. However, zonal momentum stress convergence and zonal momentum advection show substantial differences between near-surface and the ABL-average response. The momentum budget terms are shown in vector form to illustrate the force balance (Fig. 3.28). In the transition zone the near-surface acceleration becomes important and the stress convergence vector rotates counter-clockwise before adjusting to the new Ekman balance in the quasi-equilibrium region.

3.4. Comparison of the responses between P4 and M4

The qualitative and quantitative differences in the adjustment mechanism of P4 and M4 are highlighted by adding the two simulations and removing the zonal average from the sum. If the responses are completely symmetric, the composites will be zero. Any non-symmetric responses will deviate from zero. The results show that asymmetries are found mostly in the transition zone (Fig. 3.29). The largest differences occur near the upstream boundary of the transition region while smaller differences are found closer to the downstream boundary of the transition region. The large asymmetries near 60.9° longitude reflect the fact that the deceleration and flux convergence in the M4 transition zone are confined below 100 m while the acceleration and flux divergence in the P4 transition region extend to around 200 m. The small asymmetry near the downstream boundary of the transition zone around 60.7° longitude is the result of the slight upwind shift of the advection and flux convergence terms in M4 relative to the acceleration and flux convergence terms in P4. The momentum flux composite and the advection composite are almost complementing one another except for some stress convergence near 61.2° longitude between 300 m and 400 m. The differences between the P4 and M4 transition zones are a consequence of the different adjustment mechanism between the warm-to-cold and cold-to-warm flow. In the warm-to-cold (M4) case, the boundary layer collapses suddenly and the deceleration takes place over shorter spatial scales than the acceleration associated with the convective mixing in the internal boundary layer in the cold-to-warm (P4) case.

3.5. Discussion

Several mechanisms have been proposed to explain the strength and the location of the acceleration of near-surface winds in the vicinity of oceanic SST fronts. We presented simulations of the WRF regional mesoscale model with high vertical resolution in the boundary layer to analyze the importance of the various possible mechanisms for high correlation between mesoscale anomalies of surface wind stress and SST in the vicinity of large SST gradients. The importance of stability-induced changes in turbulent momentum transport has been emphasized by a number of studies (Sweet et al. 1981, Wallace et al. 1989, Park et al. 2002, and de Szoeke and Bretherton 2004). Mahrt (1972) and Tomas et al. (1999) have noted that momentum advection in flows in low latitudes is important. Other studies (Mahrt et al. 2004, Cronin et al. 2003, Small et al., 2005) have suggested that a (lagged) pressure adjustments is responsible for the SST-wind correlation. Samelson et al. (2006) argue that surface stress depends on the boundary layer depth. This numerical study includes pressure as a state variable and resolves the boundary layer in adequate detail to discuss the importance of pressure adjustment, momentum advection, turbulent stress convergence and the changes in boundary layer height.

The near-surface wind acceleration and deceleration is found in a narrow transition zone of about 100 km co-located with the SST-front. In this zone, we find that the change of pressure gradient is small. Therefore, the lagged pressure adjustment mechanism by Cronin et al. (2003) and Small et al. (2005) cannot explain the acceleration and deceleration in the vicinity of the SST-front. In the quasi-equilibrium region downstream from the transition region, an Ekman

balance is found between pressure gradient force, turbulent stress convergence and Coriolis force.

The balance between the pressure gradient and frictional forces alone cannot explain the vertical differential advection. While the pressure gradient force (Fig. 3.30, Fig. 3.31) is very similar below and above 200 m, the advection and stress convergence change dramatically in the lower 200 m. The large vertical changes and the shallowness of the internal boundary layer might also explain why other coarser vertical resolution models have had difficulties in simulating the observed stress convergence in the transition zone, keeping in mind that turbulent stress is modeled as a derivative quantity and hence turbulent stress convergence as a second derivative. Our findings, which are consistent with satellite observations (Chapter 1) and with observations of the marine boundary layer (Friehe et al. 1991), demonstrate the importance of adequate vertical resolution of the boundary layer. With coarser vertical resolution in the boundary layer used by Small et al. (2005) and by global circulation models it is not possible to simulate important stress convergence features near the surface.

We have shown that the quantity τ_s/H is not constant across step changes of SST. In the far fields where advection becomes small and τ_s/H can be obtained by integration, we have shown that pressure anomalies are as important as changes in boundary layer depth. In the transition zone where pressure gradient force might be assumed constant with height, we have found that advection is important and cannot be ignored. Therefore, the assumptions leading to $\tau_s/H = \text{constant}$ are not applicable to at least part of the transition region. Indeed, we have presented a simulation where turbulent stress convergence is acting to accelerate the surface winds in the downstream direction.

Our results suggest that entrainment of momentum by a convectively driven thermal internal boundary layer (TIBL) is the mechanism controlling the acceleration and the strength of the turbulent flux convergence in the transition zone of the cold-to-warm experiment. A TIBL has been found by Friehe et al. (1991) in a model simulation of the Frontal Air-Sea Interaction Experiment. The TIBL also determines the strength of the pressure perturbations since initially the air only moistens and warms within the TIBL. From the sequence of profiles in the transition region (not shown), it becomes apparent that the response of turbulence and advection somewhat leads the response of the pressure gradient. This suggests that the pressure gradient is not involved in determining the location of the acceleration in the transition zone.

Turbulent flux convergence can act to accelerate the flow in two ways, 1) by simply reducing the vertical convergence of the stress that usually acts to decelerate the flow, or 2) by actively accelerating the flow in the case when momentum is redistributed in the boundary layer. The TIBL is important in both cases. Once the TIBL forms at the SST-front, an intricate new balance between turbulence, pressure gradient and advection develops. The large sea-minus-air potential temperature difference triggers the formation of a convectively driven internal boundary layer which then grows by entrainment. Entrainment incorporates higher velocity air into the TIBL, while at the same time enhanced mixing reduces the vertical shear, thus increasing stress while decreasing stress convergence. The reduced stress convergence is balanced by an acceleration of the near-surface wind. Advection increases vertical shear while turbulent mixing reduces it. Advection and turbulent flux convergence may strengthen simultaneously until convectively driven entrainment and mixing can no longer be maintained or becomes too weak. The wind shear is large in the entrainment zone of the internal boundary layer.

Therefore, and in combination with large mixing coefficients, turbulent fluxes increase aloft and become larger than the surface flux. The near-surface turbulent stress convergence becomes positive and turbulent flux actively accelerates the flow.

The stabilizing effects of decreasing SST in the downwind direction in the M4 simulation efficiently cuts off the buoyancy generation of TKE that supports the boundary layer. As a result, the momentum boundary layer collapses and little mixing remains above the new boundary layer top at about 200 m. The air aloft is free to accelerate which effectively separates faster moving air from the slower moving air within the boundary layer. The pressure gradient in the new shallow boundary layer cannot support the upstream wind speed and the reduced mixing acts to decelerate the surface winds. The resulting deceleration leads to strong advection near the surface and reduces the vertical shear. As in the P4 simulation, advection and turbulent stress convergence increase in magnitude simultaneously to efficiently reduce surface wind speed and adjust the flow towards the new balanced state.

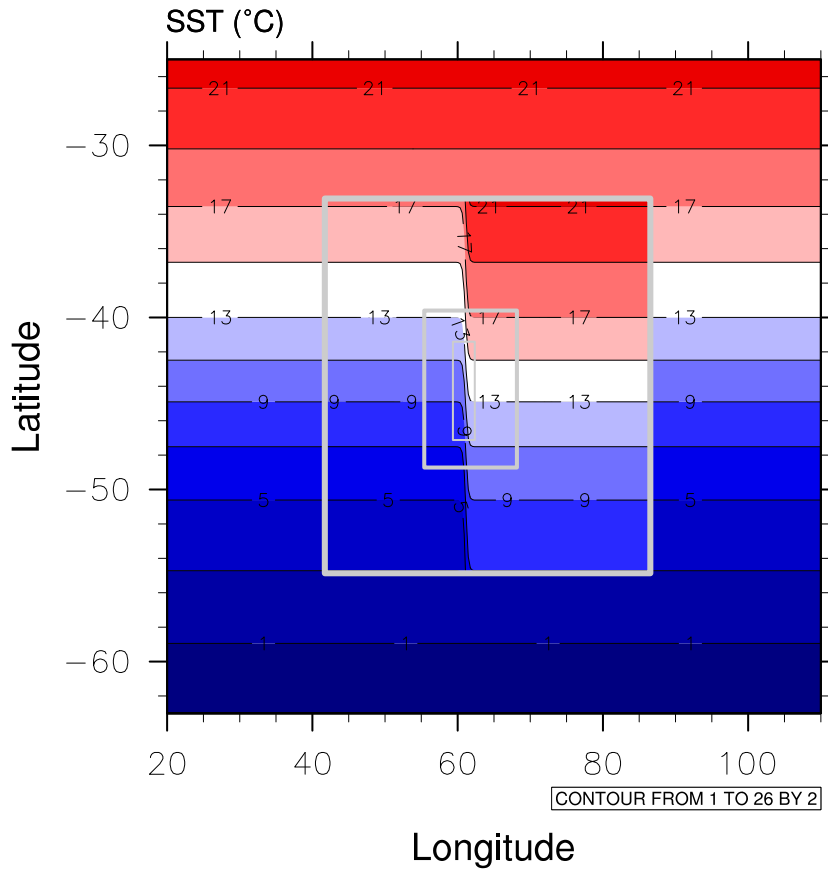


FIGURE 3.1. Maps of background SST in the region of the Agulhas return current. Shaded SST is shown in 2°C contour intervals. Gray rectangles denote the boundaries of the 3 nested WRF domains. Inside the WRF domains the SST is increased by 4 K within a narrow north-south frontal region.

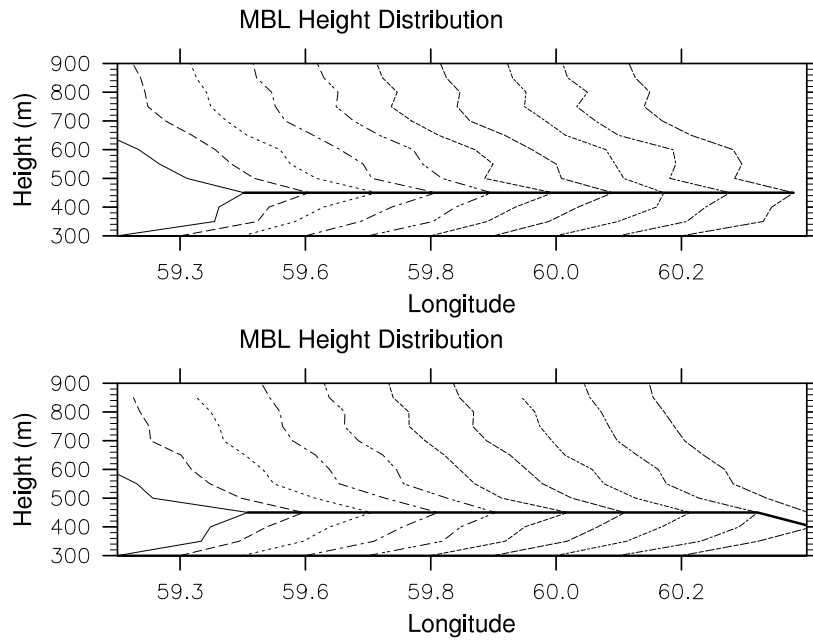


FIGURE 3.2. Bin-averaged distribution of normalized momentum boundary layer depth as function of longitude in the upstream region. Each vertical profile is a distribution at a given longitude. A thick line denotes the ABL depth that occurred most often. Top panel is derived from the P4 experiment and the bottom panel from the M4 experiment. The vertical bin size for each distribution is 50m. Shown is the region upstream of the SST front where the momentum boundary layer depth is not influenced by the SST front.

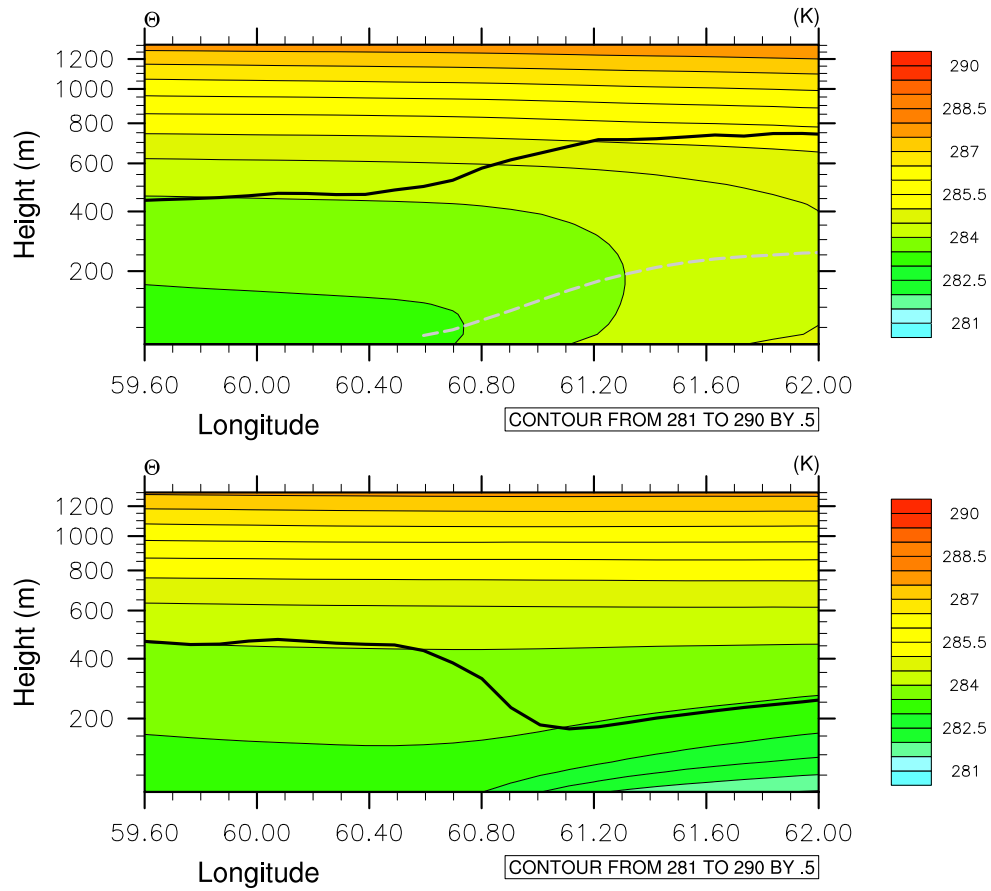


FIGURE 3.3. Longitude-height cross-section of the potential temperature θ . Top panel shows results from P4 and bottom panel results from M4. The solid line in each panel denotes the momentum boundary layer depth; the thick dashed line in the upper panel is a measure of the internal boundary layer depth. See text for the definitions of the boundary layer depths.

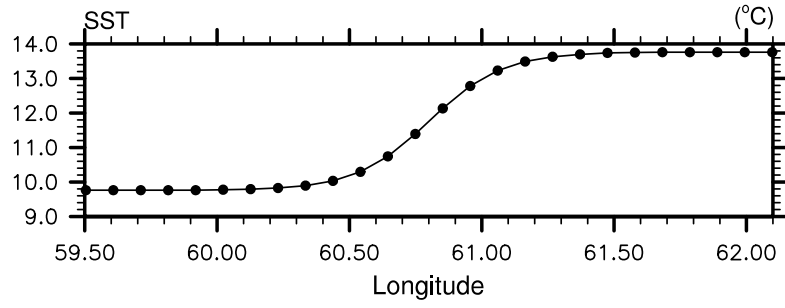


FIGURE 3.4. Sea surface temperature at 43° S as function of longitude. Dots represents model gridpoint locations. Latitudinal dependence of SST is approximately a cosine function of the latitude.

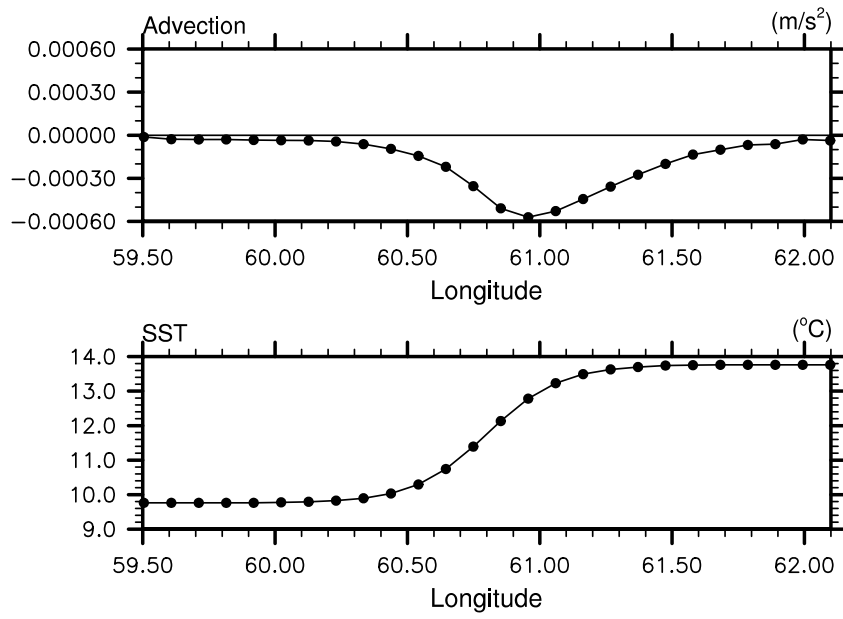


FIGURE 3.5. Top: Near-surface advection as a function of longitude. Bottom: Co-located sea surface temperature distribution as function of longitude.

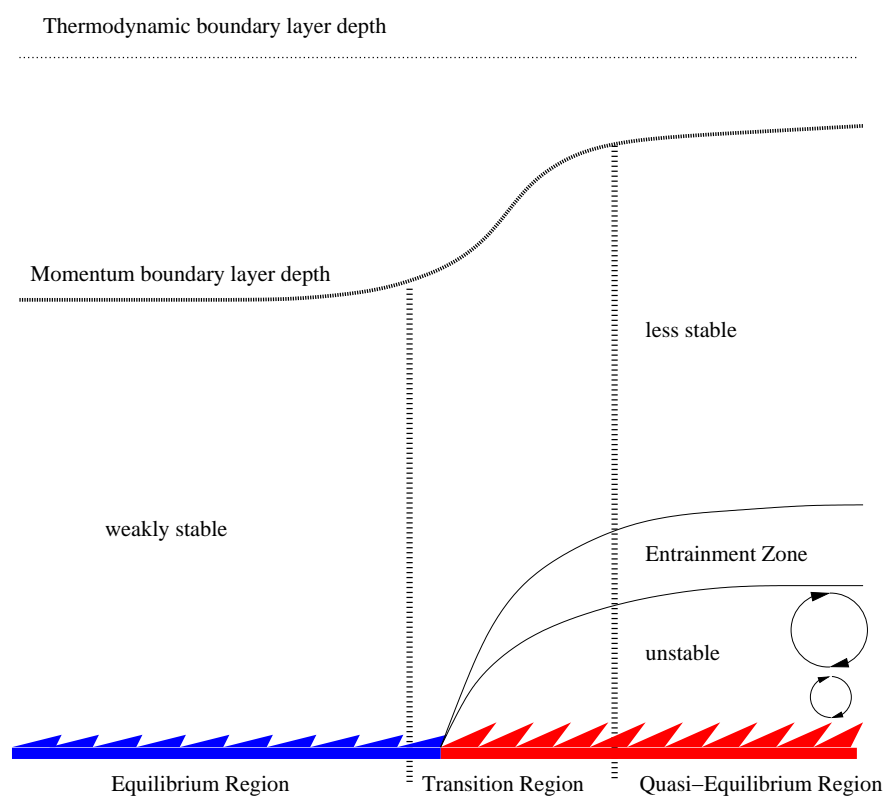


FIGURE 3.6. Schematic description of the cold-to-warm experiment.

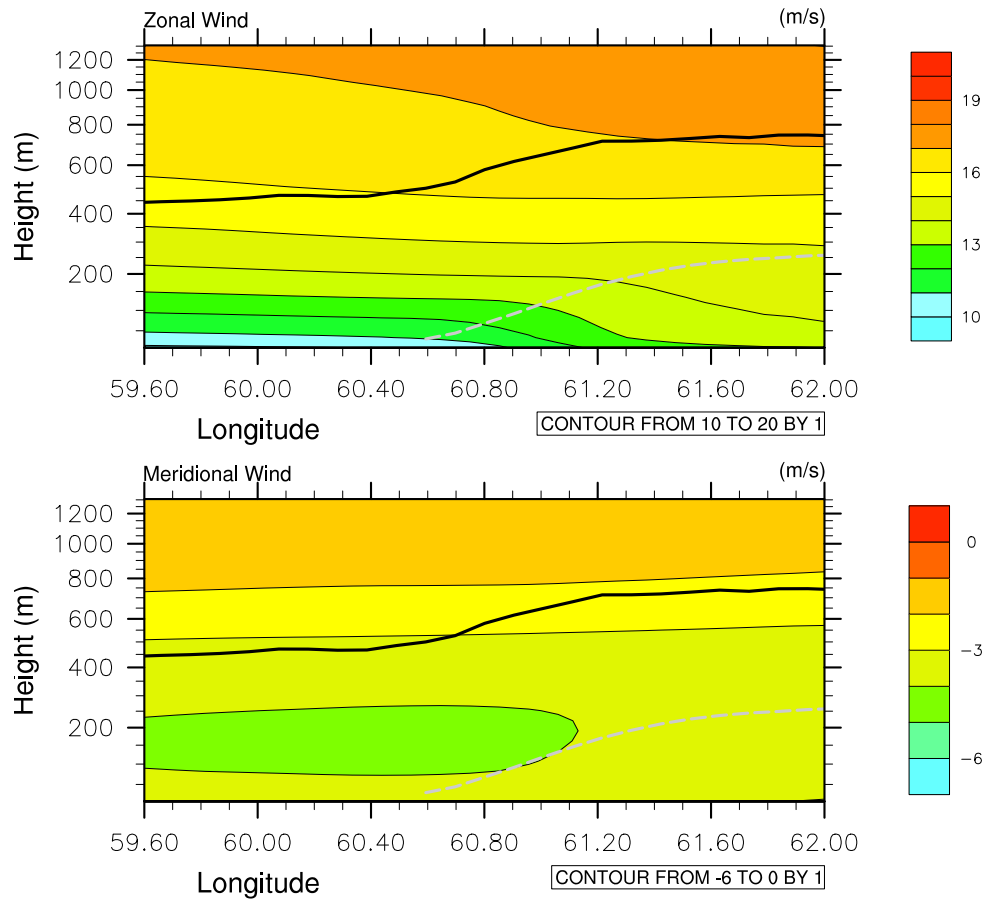


FIGURE 3.7. As in Fig. 3.3, except for the zonal (top) and meridional (bottom) velocity of the P4 experiment.

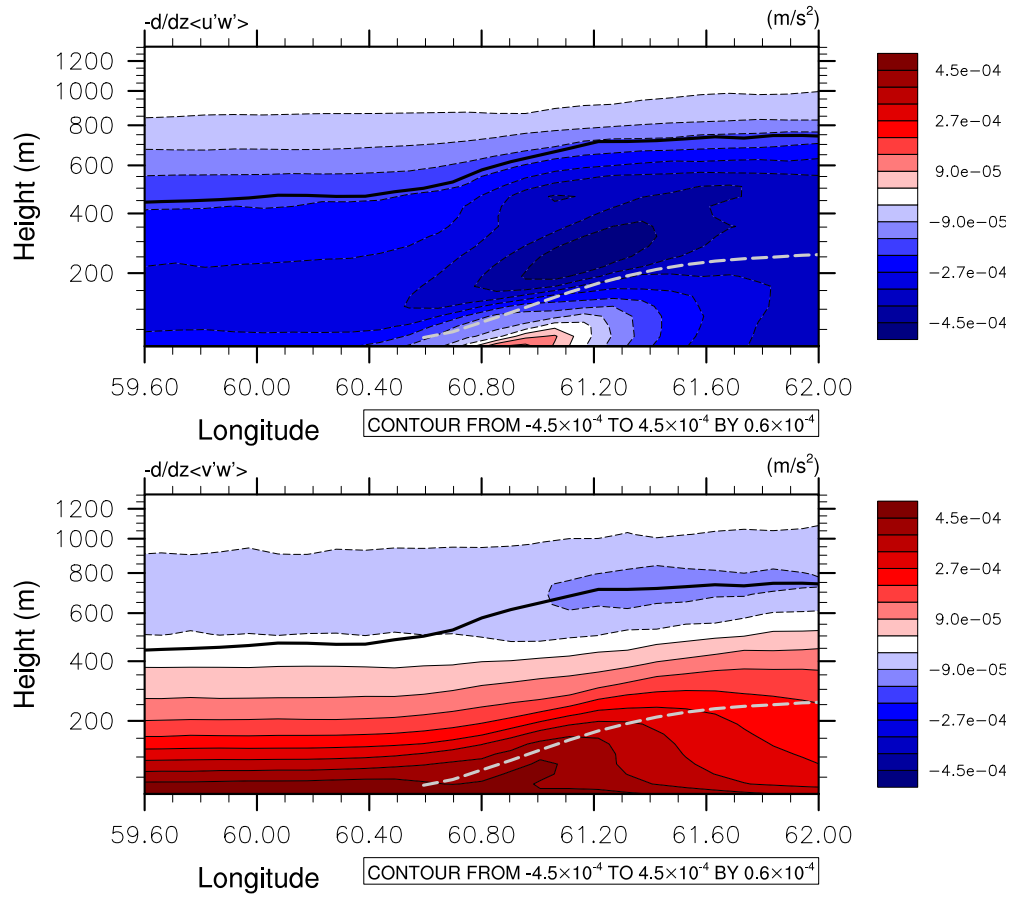


FIGURE 3.8. As in Fig. 3.3, except for the zonal (top) and meridional (bottom) turbulent stress convergence of the P4 experiment.

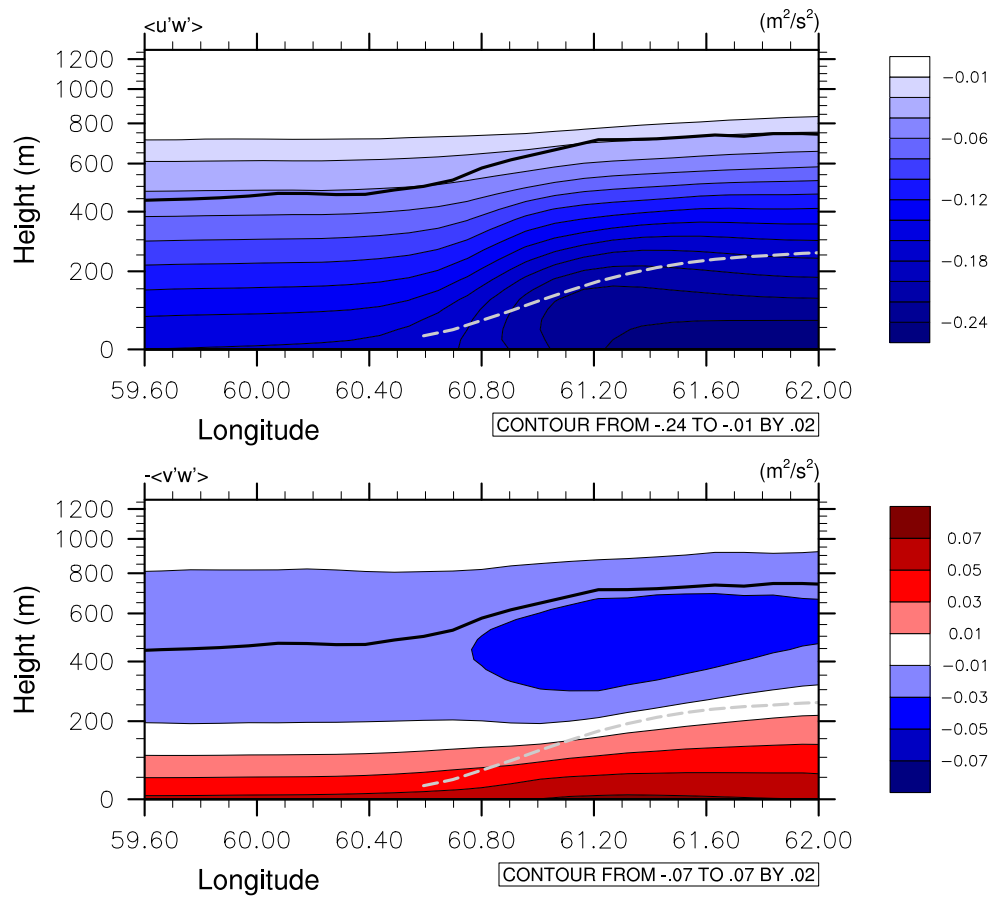


FIGURE 3.9. As in Fig. 3.3, except for the zonal (top) and meridional (bottom) turbulent stress of the P4 experiment.

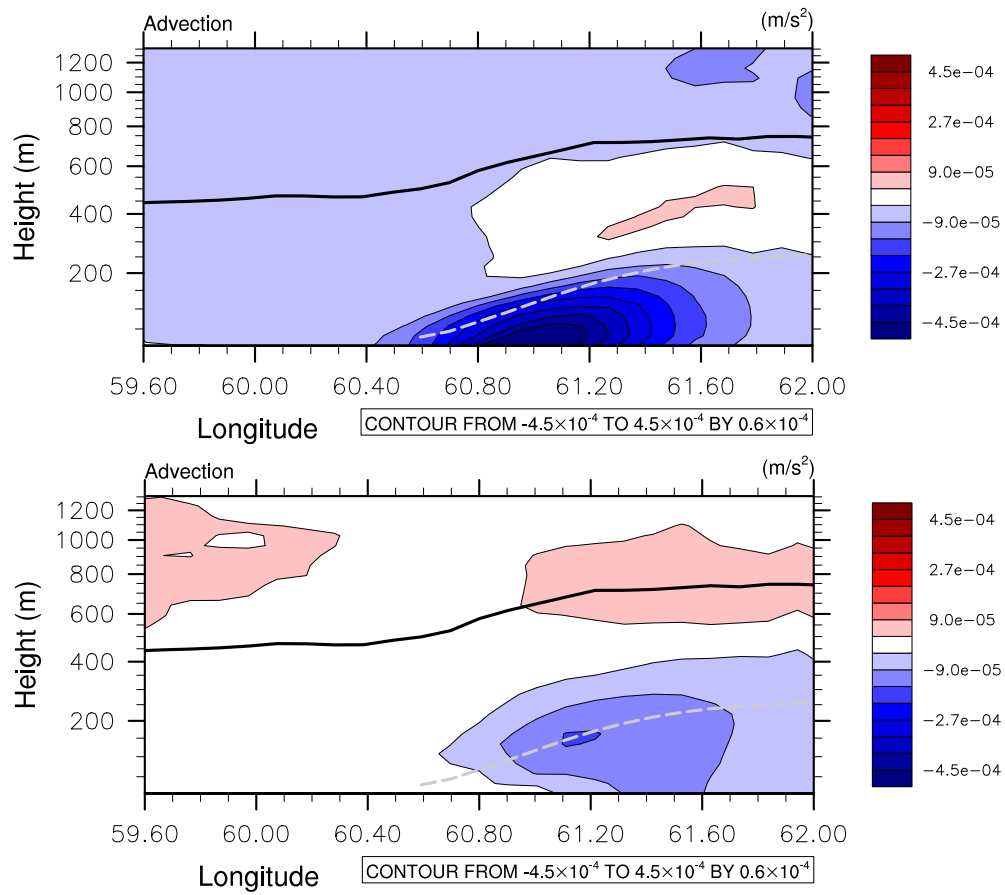


FIGURE 3.10. As in Fig. 3.3, except for the zonal (top) and meridional (bottom) advection of the P4 experiment.

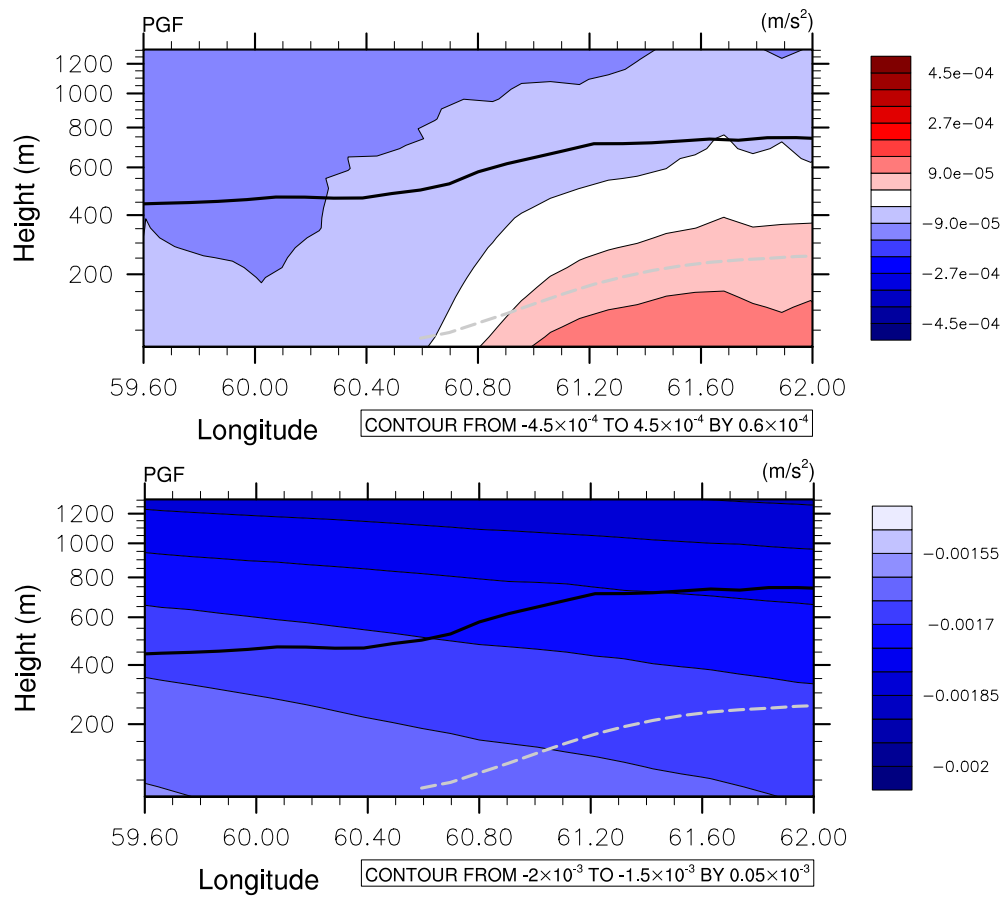


FIGURE 3.11. As in Fig. 3.3, except for the zonal (top) and meridional (bottom) pressure gradient force of the P4 experiment.

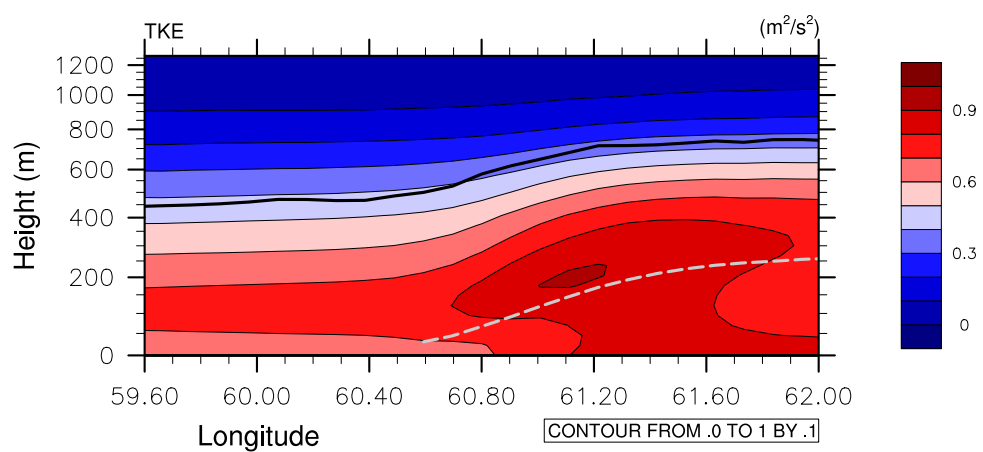


FIGURE 3.12. As in Fig. 3.3, except for the turbulent kinetic energy of the P4 experiment.

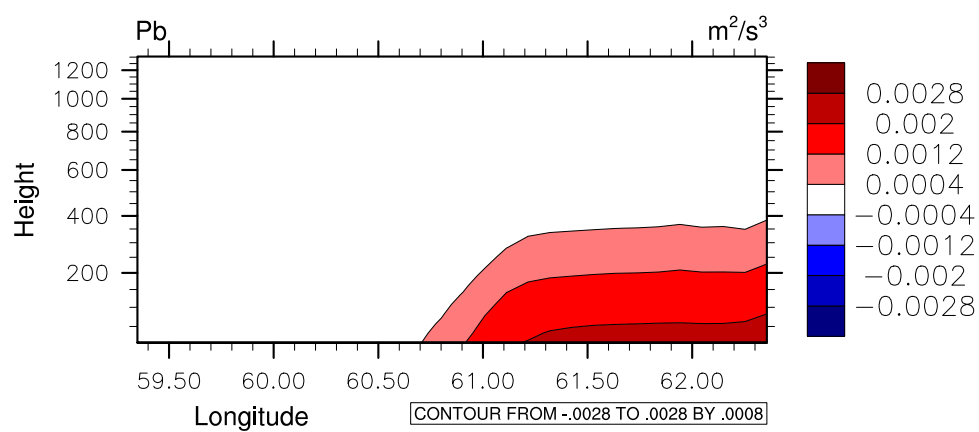


FIGURE 3.13. As in Fig. 3.3, except for the buoyancy production of turbulent kinetic energy of the P4 experiment.

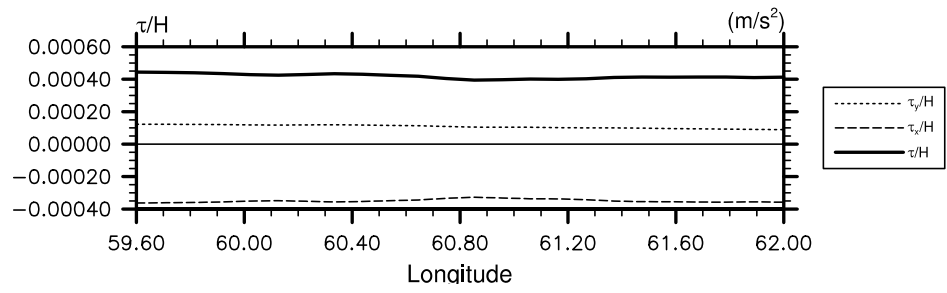


FIGURE 3.14. Ratio of surface stress to momentum boundary layer depth as function of longitude. Solid line denotes the magnitude τ_s/H , dashed the zonal component τ_x/H and dotted the meridional component τ_y/H .

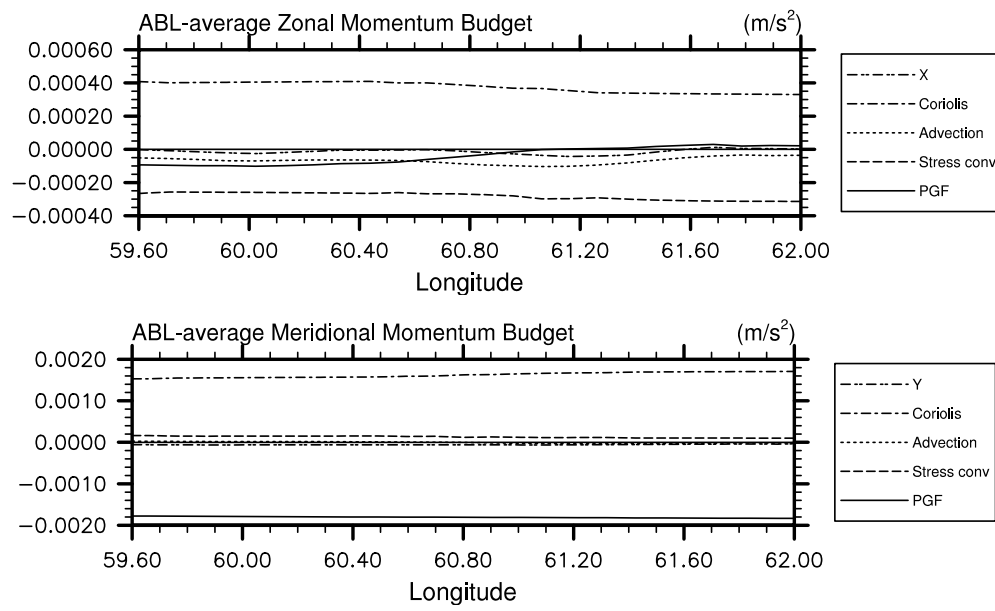


FIGURE 3.15. Momentum boundary layer average zonal (top) and meridional (bottom) momentum budget as function of longitude. The zonal and the meridional residual is denoted by X, Y, respectively.

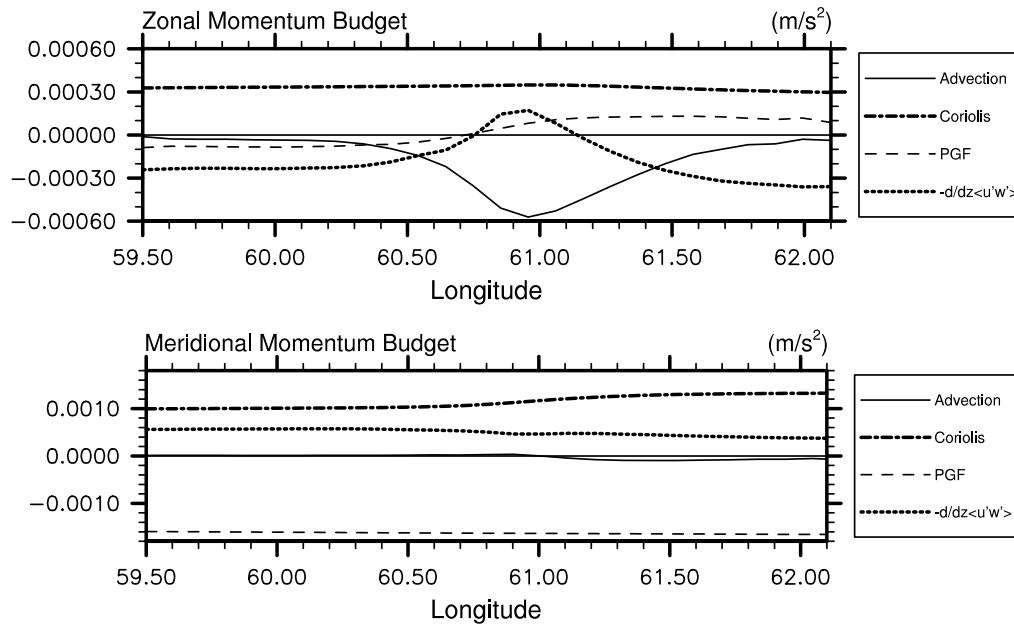


FIGURE 3.16. Zonal (top) and meridional (bottom) momentum balance at near surface model level (12m) as function of longitude. Shown are advection (solid), coriolis (thick dash-dotted), pressure gradient (dashed) and turbulent stress convergence (thick dotted).

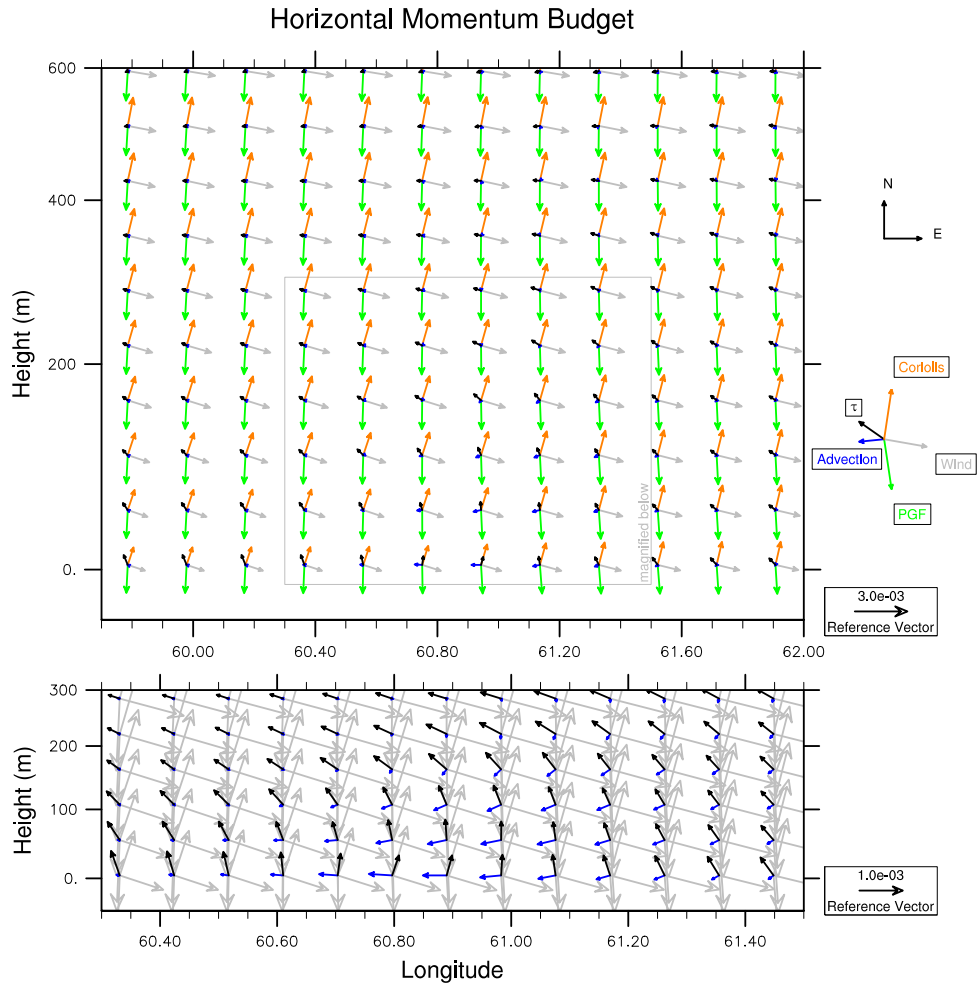


FIGURE 3.17. Vertically staggered vector representation of the momentum budget from P4. Northward vectors are pointing up and eastward vectors point to the right. Top panel vectors represent Coriolis (orange), advection (blue), turbulent stress convergence (τ , black), and pressure gradient force (“PGF”, green). Additionally wind direction (“Wind”) is overlaid in gray. Bottom panel shows selection of top panel magnified with colored vectors for advection (blue) and turbulent stress convergence (black), other vectors are repeated for completeness, but grayed-out for clarity. Note that not all grid locations are showed.

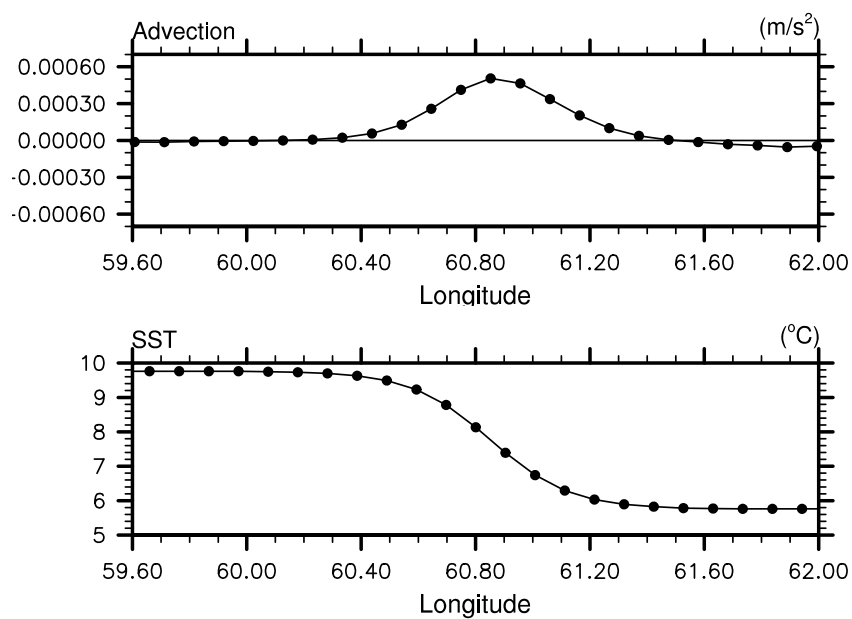


FIGURE 3.18. Top: Near-surface advection as a function of longitude. Bottom: Co-located sea surface temperature distribution as function of longitude.

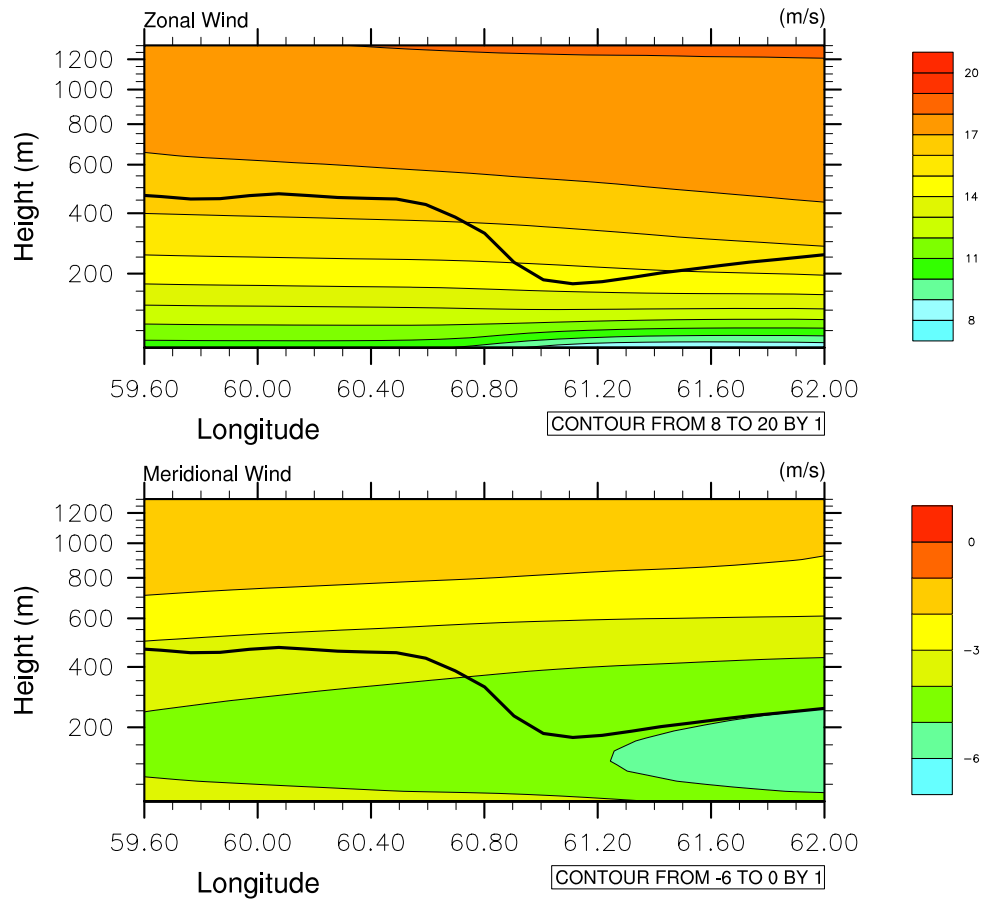


FIGURE 3.19. As in Fig. 3.3, except for the zonal (top) and meridional (bottom) velocity for the M4 experiment.

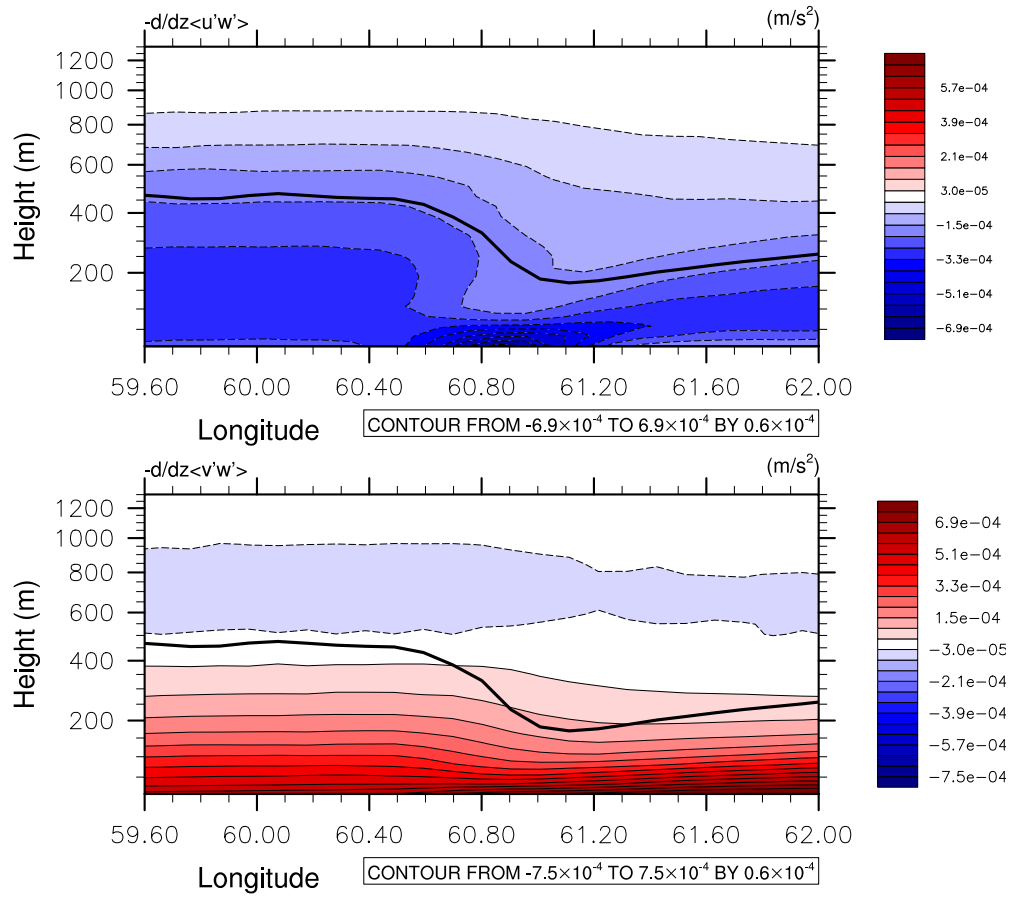


FIGURE 3.20. As in Fig. 3.3, except for the zonal (top) and meridional (bottom) turbulent stress convergence of the M4 experiment.

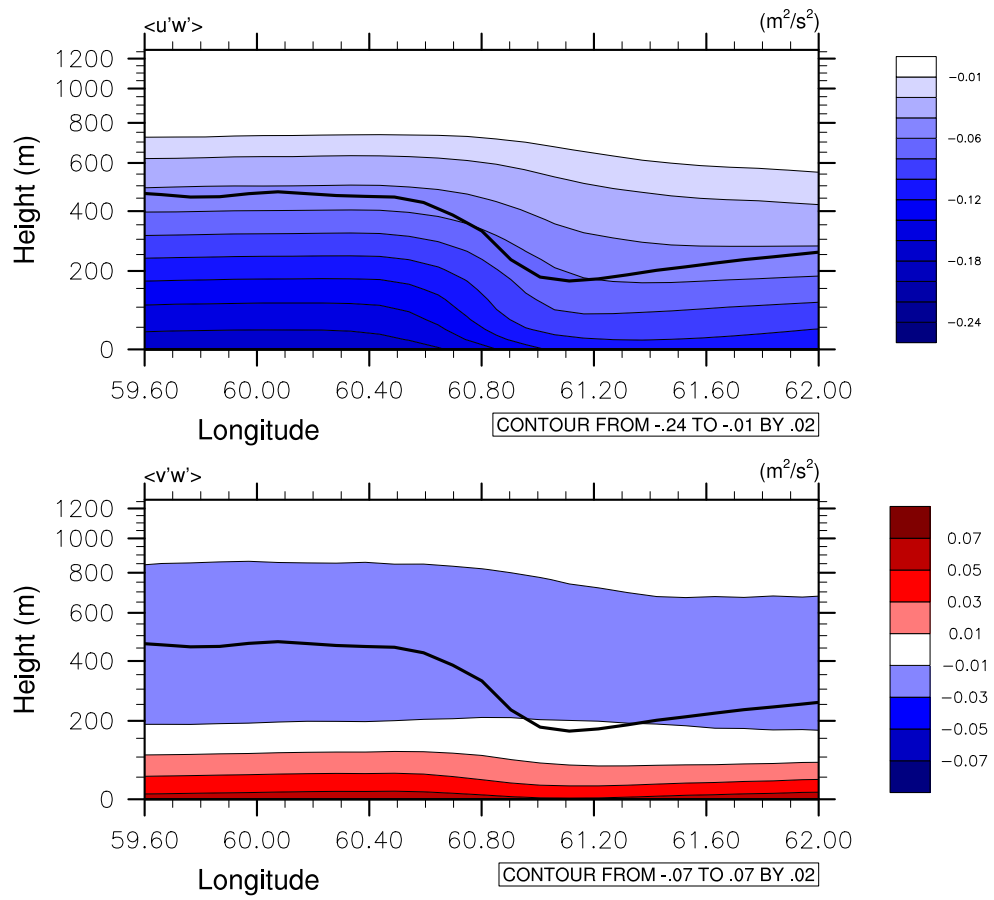


FIGURE 3.21. As in Fig. 3.3, except for the zonal (top) and meridional (bottom) turbulent stress of the M4 experiment.

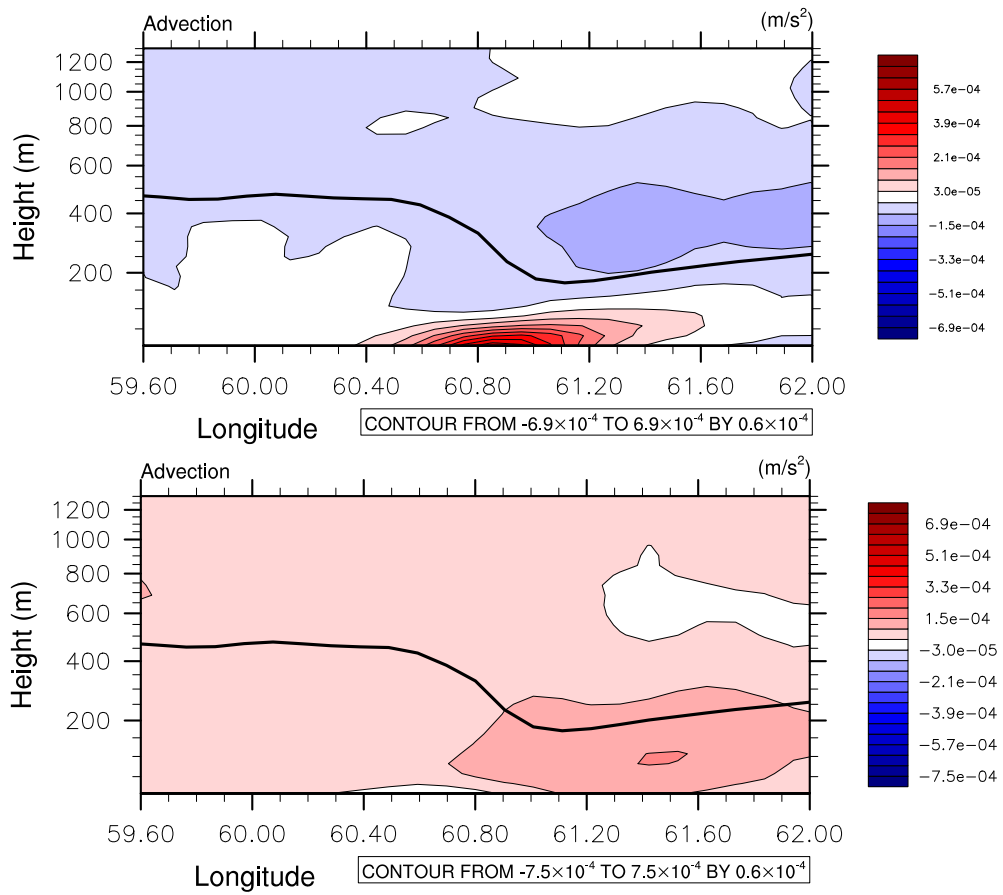


FIGURE 3.22. As in Fig. 3.3, except for the zonal (top) and meridional (bottom) advection of the M4 experiment.

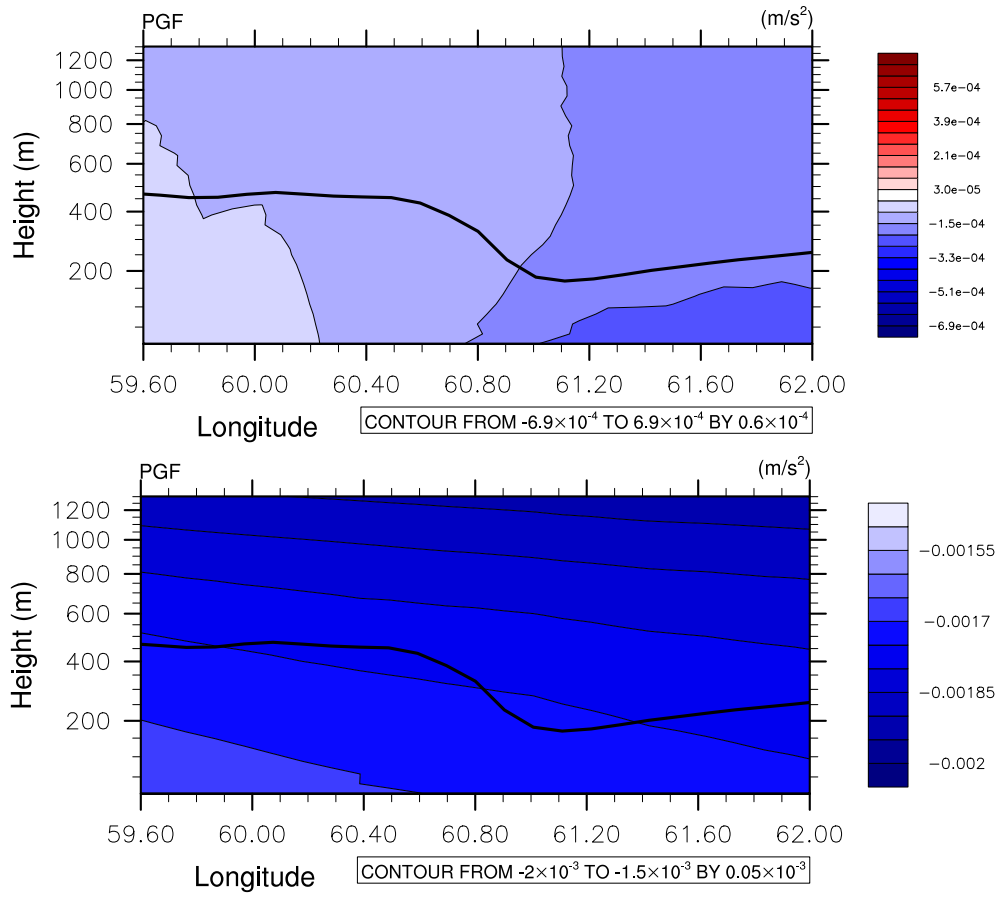


FIGURE 3.23. As in Fig. 3.3, except for the zonal (top) and meridional (bottom) pressure gradient force of the M4 experiment.

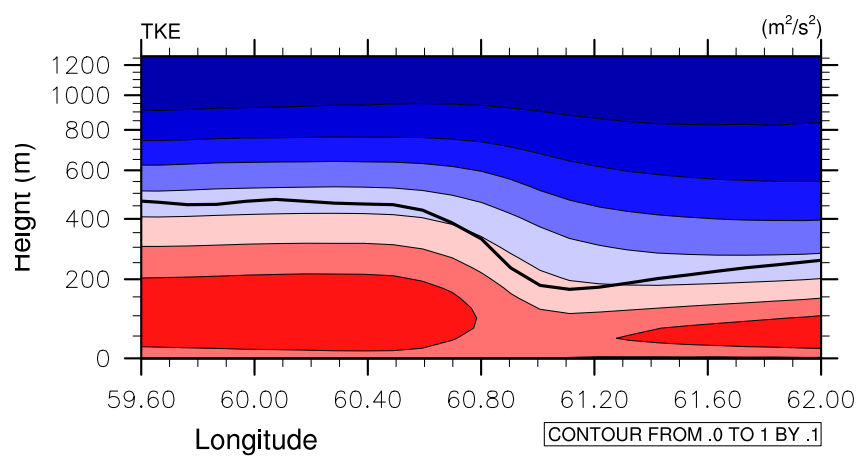


FIGURE 3.24. As in Fig. 3.3, except for the turbulent kinetic energy of the M4 experiment.

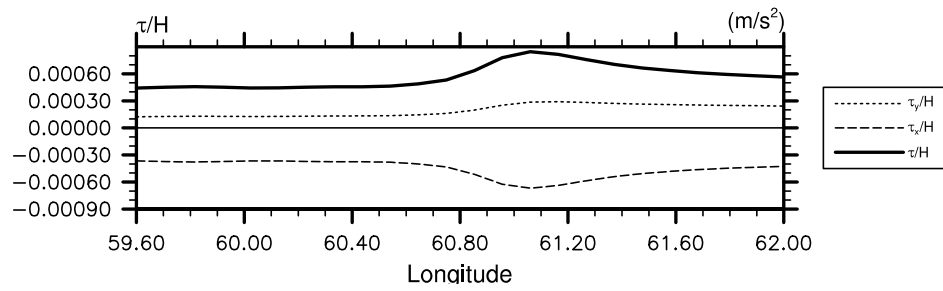


FIGURE 3.25. Ratio of surface stress to ABL depth as function of longitude. The solid line denotes the magnitude τ_s/H , dashed the zonal component τ_x/H and dotted the meridional component τ_y/H .

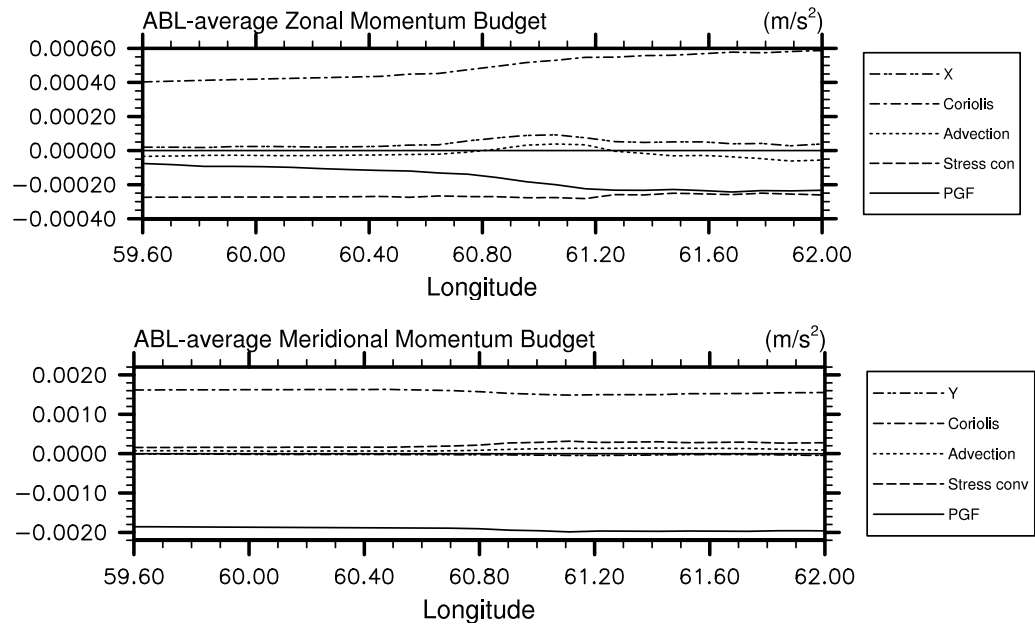


FIGURE 3.26. Momentum boundary layer average zonal (top) and meridional (bottom) momentum budget as function of longitude. The zonal and the meridional residual is denoted by X, Y, respectively.

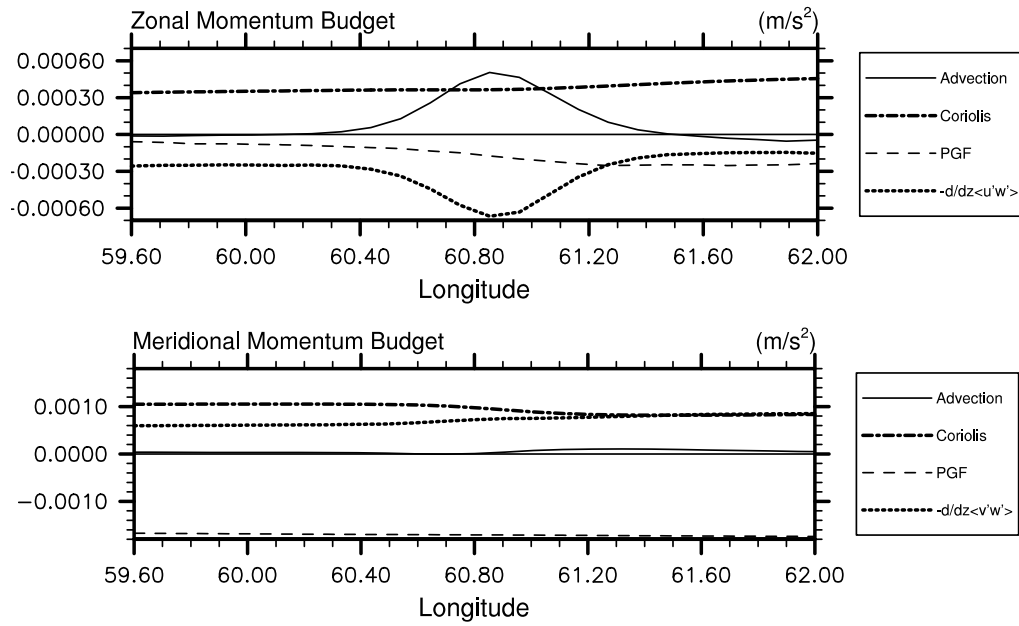


FIGURE 3.27. Zonal (top) and meridional (bottom) Momentum Balance at near surface model level (12m) as function of Longitude. Shown are Advection (solid), Coriolis (thick dash-dotted), Pressure gradient (dashed) and turbulent stress convergence (thick dotted).

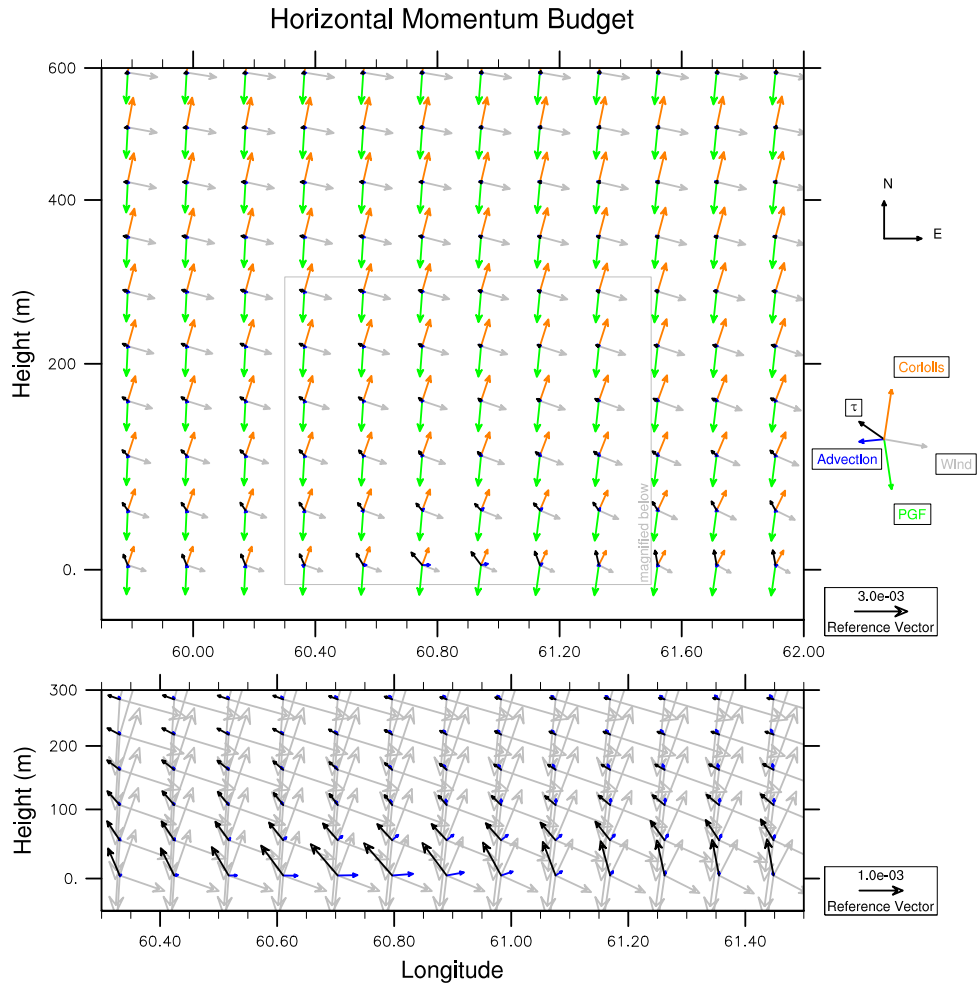


FIGURE 3.28. Vertically staggered vector representation of the momentum budget from M4. Northward vectors are pointing up and eastward vectors point to the right. Top panel vectors represent Coriolis (orange), advection (blue), turbulent stress convergence (τ , black), and pressure gradient force (“PGF”, green). Additionally wind direction (“Wind”) is overlaid in gray. Bottom panel shows selection of top panel magnified with colored vectors for advection (blue) and turbulent stress convergence (black), other vectors are repeated for completeness, but grayed-out for clarity. Note that not all grid locations are shown.

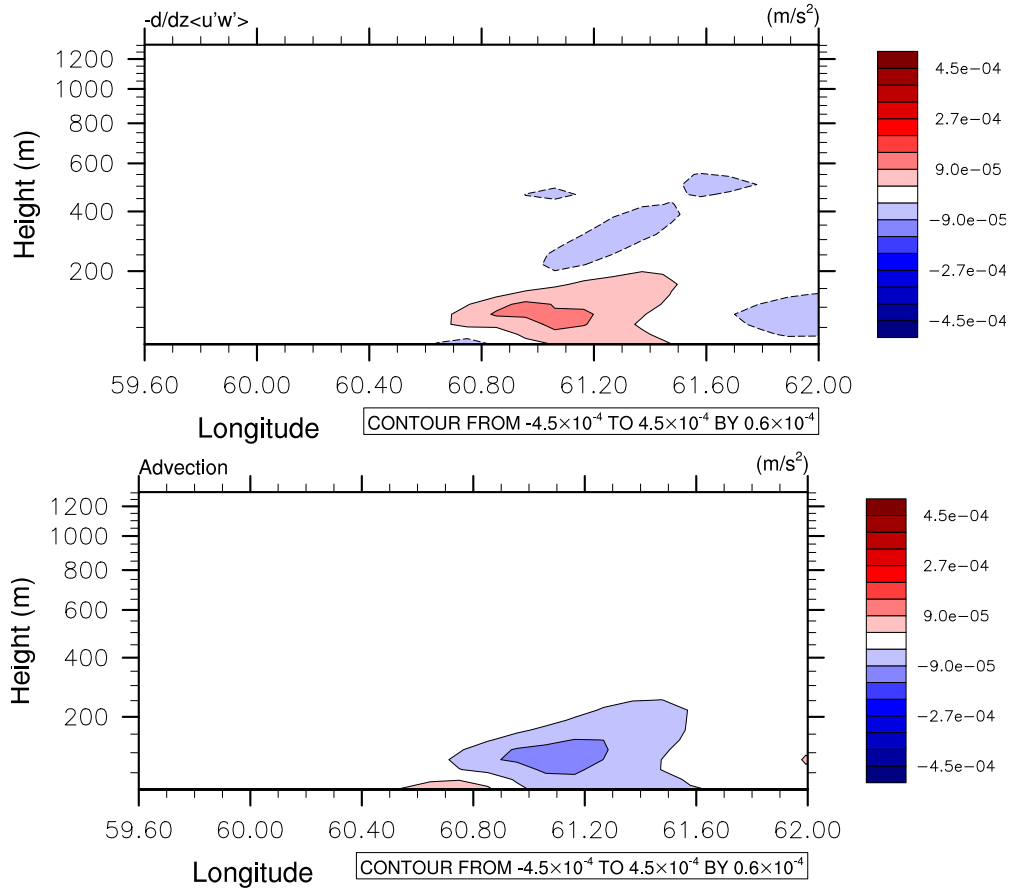


FIGURE 3.29. Longitude-height cross section of 1) zonal turbulent flux convergence from P4 and M4 added and zonal mean removed (top) and 2) zonal advection from P4 and M4 added and zonal mean removed (bottom).

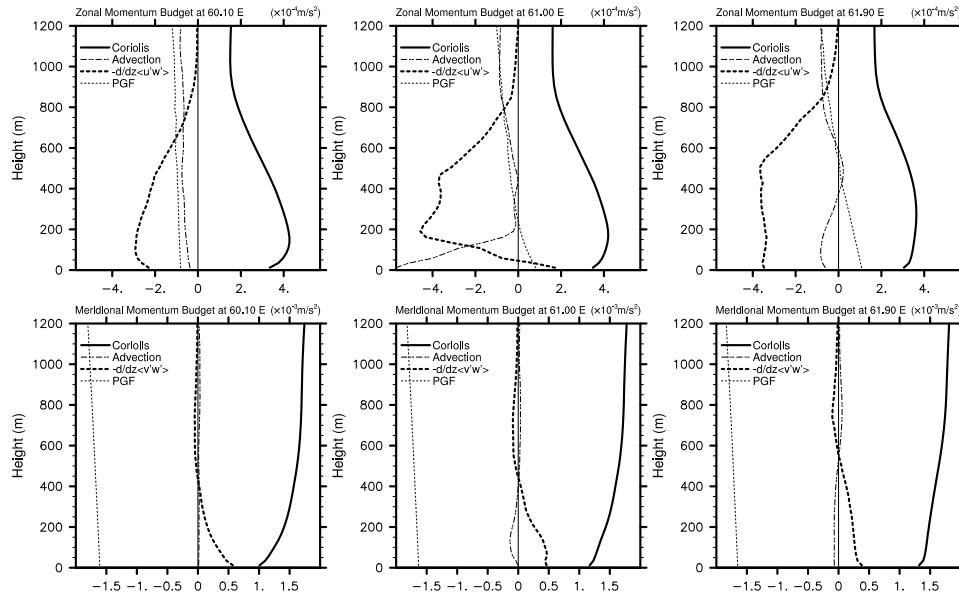


FIGURE 3.30. Vertical profile of the zonal (top) and meridional (bottom) momentum budget from P4 at three locations. Shown from left to right are the upstream, transition and downstream region relative to the SST front. Note the order-1 difference of scales of zonal and meridional budgets.

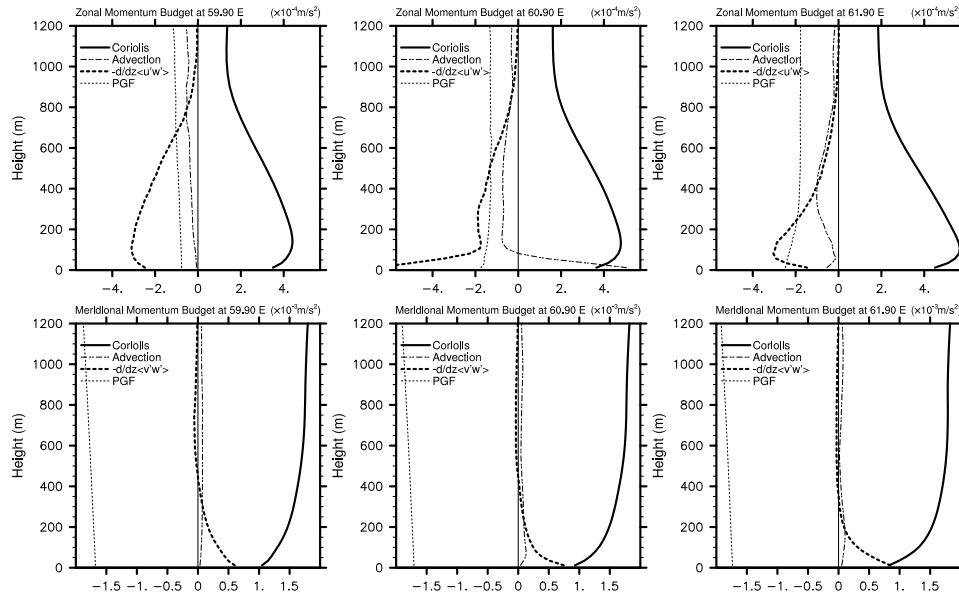


FIGURE 3.31. Vertical profile of the zonal (top) and meridional (bottom) momentum budget from M4 at three locations. Shown from left to right are the upstream, transition and downstream region relative to the SST front. Note the order-1 difference of scales of zonal and meridional budgets.

4. ABL RESPONSE TO IDEALIZED MESOSCALE MIDLATITUDE SST ANOMALIES

In the Agulhas region, the monthly averaged SST pattern appears to be a quasi-periodic series of warm and cold anomalies with spatial scales on the order of 200-500 km (Fig. 2.1), giving an ABL horizontal advective timescale of ~ 6 hours. These anomalies are found over the world ocean and suggests that, in many regions with large SST variations, the ABL must be continually adjusting to changing SST. Before the downwind quasi-equilibrium conditions simulated in Chapter 3 can occur, another adjustment process has begun for the next SST anomaly. In this chapter we therefore extend our study of ABL adjustment to more realistic SST perturbations that are similar to the SST perturbations of the Agulhas region (Fig. 4.1). To remove ambiguity in the definition of the spatial scale, we examine the ABL response to sinusoidal SST anomalies. The budgets of heat and momentum then can be related directly to the SST perturbations and the phase relationships among the dependent variables can be studied. The periodic nature of the assumed SST pattern also facilitates a more robust statistical analysis.

Although vertical redistribution of momentum is important for the wind accelerations in the lower ABL, we will see that vertical momentum exchange is not the driving mechanism for the wind stress response. We show how the heating pattern creates pressure perturbations that can drive the acceleration of surface winds and we speculate how this adjustment changes with changing scales of the SST perturbations. We use the ratio τ_s/H of surface stress and boundary layer depth as an indicator to determine if the boundary layer is in a simple Ekman balance or if additional terms are necessary to describe the adjustments.

This chapter is organized in the following way: In the first section, the model configuration, the initial model fields and boundary conditions, including SST forcing, are briefly described. Section 4.1 also describes the methodology of the analysis and discusses the major force balances of the surface and the ABL-averaged momentum budget. Section 4.2 shows the importance of the pressure gradient force as the driving mechanism of the observed near-surface wind adjustments and demonstrates the good agreement between simulated surface wind divergence term and the horizontal Laplacian of the pressure term in the divergence equation.

4.1. Model description and initial fields

We analyze the ABL response to a field of mesoscale SST anomalies arranged in a checkerboard pattern with scales similar to those observed in the Agulhas region. The basic model setup is identical to Chapter 3 except for the underlying SST and the number of nested domains. The initial atmospheric fields and boundary conditions were obtained from a symmetric aqua planet CAM2 simulation performed by Eric Maloney. The CAM2 simulation was spun up for 3 years. The 30 consecutive days after spin up were used to initialize the WRF-model and to obtain the lateral boundary conditions. For practical reasons, the intermediate nest was dropped in favor of a larger inner domain with $20^\circ \times 8^\circ$ grid size. The grid spacing of the inner domain is 15 km, which is roughly two times larger than in the SST-front experiments considered in Chapter 3, but is adequate to resolve the mesoscale SST anomaly pattern. The high vertical resolution of the model experiment in Chapter 3 was maintained because of its importance for resolving the large vertical differential advection of horizontal momentum and

stress convergence (compare Fig. 3.30, Fig. 3.31, for example). The outer to inner grid ratio of 5:1 does not noticeably change the behavior of the model near the lateral boundaries compared to the 3:1 ratio in Chapter 3. However, some noise is apparent near the boundaries of the inner nest (Fig. 4.2) which cannot be removed by the 2-D loess filtering used here. Irrespective of the origin of the noise, no data within $1/2^\circ$ of the inner nest boundary was used in the analysis. The first 2 days of simulation are discarded to allow the model some adjustment time. The mean wind direction over the 28 days is west-north-west, close to the zonally symmetric flow from the CAM2 aqua-planet simulation. The 1-month averaging period is not sufficiently long to remove all synoptic variability that causes departures from the zonal flow. The integration period includes short intervals with prevailing easterly surface wind. As in Chapter 3, these easterly wind periods were excluded from the analysis. Note that the results remain qualitatively the same when including the periods of easterly wind. However the magnitude of the averaged response is reduced. Model output is composited relative to the SST anomalies so that we may interpret the ABL response as the result of prevailing westerly flow over a periodic series of warm and cold SST anomalies.

4.1.1. SST Forcing

The SST pattern is derived by estimating the spatial scales and magnitude of the SST variations in the Agulhas region (Fig. 4.2). The dominant scales are approximated as 4° longitude and 5° latitude with amplitudes of 2.5 K. These values were used to generate SST perturbations that vary in meridional and zonal direction as cosine functions of the latitude and longitude, respectively. The resulting SST field used to perturb the aqua planet background SST is shown in

(Fig. 4.1). Near the strongest SST gradients, the SST changes by about 4 K over a distance of about 1° longitude. The maximum SST gradient is thus about $1/2$ of the values used in the SST front experiment in Chapter 3.

4.1.2. Results

We calculate perturbations of the flow by applying a spatial high-pass filter to all meteorological variables. We use the same 30° longitude by 10° latitude loess-filter that was discussed in Chapter 2. The similarity of the response of the zonal and meridional wind perturbations over the entire inner domain for all positive anomalies, and for all negative anomalies (Fig. 4.2), motivates compositing the ABL response relative to the SST perturbations. The homogeneity of the response also allows us to examine the variability in the zonal direction by averaging the meteorological fields in meridional direction only. The resulting height-longitude and surface composite figures cover a spatial area that extends 2.5° or $1/2$ wavelength of the SST perturbation in meridional direction and the entire domain in zonal direction.

For consistency and to simplify comparison between this and the previous results in Chapter 3, the methodology from Chapter 3 is used to determine the average momentum boundary layer depth. Since the previous simulations and this simulation are based on the same aqua planet boundary conditions, it is reasonable to assume the same momentum boundary layer depth of 450 m over unperturbed SST. The value of turbulent flux convergence that represents the boundary layer depth (\mathfrak{S}_{450}) is assumed to be $2 \times 10^{-4} \text{ ms}^{-2}$. The exact value that is chosen to represent the momentum boundary layer depth is not crucial for the analysis

in this chapter. The conclusions of this chapter are the same for other values or methods (not shown) to determine the momentum boundary layer depth.

Although the analysis will focus mainly on the composited fields, the spatial relation between the SST perturbation and the ABL response can more easily be perceived initially by eye by visualizing the response over the entire domain. The maps of near-surface zonal and meridional velocity (Fig. 4.2) reveal the consistency of the ABL response to the SST perturbation. The wavelength of the SST perturbation is used as the unit length of phase ($= 360^\circ$) to quantify the phase relation between wind and SST perturbations. It is apparent that the zonal velocity is phase locked to the SST perturbations with a shift of about 30° longitudinally and 7° latitudinally to the south-east relative to the SST perturbation. The amplitude of the zonal velocity perturbation is about 2 ms^{-1} . The meridional velocity anomaly is phase shifted approximately 90° to the east and is nearly in phase in the south-north direction relative to the SST anomaly. Therefore, meridional velocity is in phase with the SST gradient. The meridional velocity anomalies are on the order of 0.6 ms^{-1} , about one-third weaker than the zonal velocity anomalies. The spatial scale of the imposed SST perturbations is different in the meridional and zonal direction, thus creating smaller SST gradients in the meridional direction than in the zonal direction. The reasons for the phase relationships will be addressed at a later point but the horizontal scale difference explains the differences in the zonal and meridional velocities. The slight off-meridian location of the zonal velocity pattern towards the south-east relative to the SST perturbation agrees very well with the direction of the prevailing wind.

The longitude-height cross sections in Figs. 4.3 – 4.6 are used to show the vertical structure of quantities that are important for the boundary layer momentum budgets. Each cross section shown is chosen along the latitude of

maximum ABL response to the SST anomalies for a given variable. The lower panel of Fig. 4.3 shows the vertical structure of zonal wind and turbulent stress convergence in relation to the boundary layer depth. The top panel in Fig. 4.3 shows SST, boundary layer depth, and perturbations of near-surface advection, turbulent stress convergence, coriolis force, and pressure gradient force at the same latitude of maximum ABL response.

The response of zonal wind is strongest near the surface and becomes small above 120 m Fig. 4.3. The zonal turbulent stress convergence term has a dipole pattern with largest values near the surface and a reversal in sign at around 120 m. A similar pattern was found in the transition zone over the SST fronts Chapter 3. While the stress divergence maximum generally is observed over negative SST gradients, the precise location of the maximum turbulent stress divergence is exactly where the momentum boundary layer depth minimum occurs. Maximum turbulent stress convergence, on the other hand, occurs over the maximum positive SST gradients. The amplitude of the surface zonal stress convergence is about $2 \times 10^{-4} \text{ms}^{-2}$, which is comparable to the amplitude found in the P4 and M4 experiment.

The growth and collapse of the momentum boundary layer as air flows over the SST anomalies is apparent in the middle and upper panels of Fig. 4.3. The change of H is not symmetric relative to the SST. The growth phase from the minimum to maximum momentum boundary layer depth is almost 3 times as long as the short collapsing phase. The maximum H is shifted about 25° in wavelength downstream in terms of SST phase while the minimum H is observed 35° in wavelength upstream of the SST minima. In regions of surface cooling, the momentum boundary layer collapses more rapidly than it increases over regions of surface warming. The momentum boundary layer begins to deepen in

a region where downwind SST is still decreasing (e.g. near 67° longitude) and it continues to grow in regions where the downwind SST is already decreasing (e.g. 70.1° longitude). The buoyancy flux, generated by the air-sea temperature difference, heats the boundary layer from below and generates turbulence. Once the heating is cut off, the turbulence decays rapidly in the layer above. On the other hand, it takes time to deepen the boundary layer by buoyancy because turbulent elements have to overcome the slightly stable environment. Over time, the surface heating therefore gets distributed over a deeper layer.

Samelson et al. (2006) note that the ratio τ_s/H of surface stress and boundary layer depth should be approximately constant under the assumption of constant pressure gradients and equilibrium conditions. Greater surface wind stress should therefore be associated with a deeper momentum boundary layer. If τ_s/H is not constant, the ABL may not be in equilibrium or other effects that were neglected may be important. The ratio τ_s/H therefore may be used as an indicator of where a simple steady Ekman balance does or does not hold. The ratio may be used to divide the third panel into 3 distinct sections: (1) a section of fairly constant ratio of around $3 \times 10^{-4} \text{s}^{-1}$, (2) a section of rapid increase in τ_s/H to as much as $7 \times 10^{-4} \text{s}^{-1}$, and (3) a subsequent section of slow decrease back to the constant value (Fig. 4.3, third panel).

The two dominant terms of the surface zonal momentum budget – zonal momentum advection and stress convergence – are shown in second panel of Fig. 4.3. Similar to the SST front experiment in Chapter 3, the two terms have the same phase relationship to the SST and are nearly a mirror-image of the other: positive advection and turbulent flux divergence over negative SST gradients and vice versa.

Similarly Fig. 4.4 shows a longitude-height cross section, but for meridional velocity and meridional turbulent convergence. The pattern of turbulent stress convergence tilts eastward while the contours of meridional velocity are tilted westward with height. The maximum meridional wind is not found near the surface, but aloft at around 120 m.

The composites of the zonal and meridional surface pressure gradient perturbations show that the zonal surface pressure gradient perturbation nearly in phase with the SST perturbation (Fig. 4.5). Assuming hydrostatic balance, it might be expected that pressure anomalies are in phase with SST anomalies and the pressure gradient force therefore should be in phase with the SST gradient. However, temperature advection (Thum et al. 2002; Small et al. 2004) and the delay in upper-layer heating shifts the pressure gradient downwind. In a vertically integrated sense, the surface pressure gradient force can be approximated following Mahrt et al. (1982) and assuming no contribution from the free atmosphere:

$$-\frac{1}{\rho_o} \frac{\partial P}{\partial x} = -g\Delta\theta \frac{\partial H}{\partial x} + \Gamma H \frac{\partial \theta}{\partial x}, \quad (4.1)$$

$$\text{where } \Gamma = \frac{g}{\theta_o}. \quad (4.2)$$

The first term on the RHS corresponds to the pressure gradient force in the shallow water equations accounting for a change in the ABL depth H and the second term accounts for the change in perturbation pressure gradient force due to horizontal variation in ABL density. The two terms usually have opposing effects: As the boundary layer deepens, less dense air above the boundary layer is replaced by denser boundary layer air, thereby creating a pressure gradient force towards the region with lower boundary layer depth in analogy to the shallow water equation. The second term, however, creates a pressure gradient force in the direction of increasing boundary layer depth because the heat flux decreases the

average density of the boundary layer. Cronin (2003) suggested that both terms balance in the region where the boundary layer deepens rapidly, thereby shifting the response of the pressure gradient. In this experiment, however, the weak stratification near the boundary layer top creates only small density differences and the effect of the shallow water term is negligible. The pressure gradient force can be estimated by the change in potential temperature alone and Eqn. 4.1 can be written as:

$$-\frac{1}{\rho_o} \frac{\partial P}{\partial x} \approx \Gamma H \frac{\partial \theta}{\partial x}, \quad (4.3)$$

The model pressure gradient force and the estimated pressure gradient force based on Eqn. 4.3 show a good agreement in terms of magnitude and location relative to the pattern of SST (Fig. 4.6).

The surface momentum budget is not in Ekman balance (Fig. 4.4). Zonal advection is balanced by stress convergence and a significant ageostrophic component is observed because the zonal Coriolis force and the pressure gradient force show a similar rather than opposing surface pattern. The resulting ageostrophic wind is important for maintaining the balance of the surface zonal momentum budget.

The largest term of the meridional momentum budget over maximum SST anomalies is the meridional Coriolis force (Fig. 4.4). It originates from the large changes of the zonal velocity. The meridional pressure gradient is negligible at the latitude of strongest SST anomalies (Fig. 4.5), leaving the coriolis term unbalanced by the pressure gradient force. The balance is maintained by the meridional component of the stress convergence and meridional advection of momentum. Although the surface pressure gradient is in phase with the SST anomalies in the meridional direction, the meridional surface stress is not in phase with the SST

pattern but is shifted about 30° in wavelength to the south relative to the SST anomalies. This phase shift might be explained by the large Coriolis term right over the maximum SST anomalies.

Assuming zero stress at the top of the momentum boundary layer, the monthly layer-averaged stress convergence is expected to equal the negative of the surface stress written in a bulk formulation $\tau(H) - \tau(0) = H * C_d * v * |V|$. This is true for the zonal component of stress and surface wind. However, we find a discrepancy between the monthly layer-averaged meridional stress and the meridional surface stress from the bulk formula. This indicates that the nonlinearities in the bulk formulation are important.

4.2. Discussion

The findings of this chapter differ in several aspects from the expectations derived from simple quasi 2-dimensional flow across an SST front considered in Chapter 3. The growth and decay of the boundary layer and the significant changes in τ_s/H clearly indicate that a simple balance between stress convergence and a change in boundary layer depth as suggested by Samelson et al. (2006) is not adequate on this scale. The pressure is not constant across the SST anomalies. The scale of the SST pattern is such that the surface heating persists long enough so that it can heat a deep enough layer to change the pressure significantly. Temperature advection creates a shift in the pressure response. The scale of the response of the surface stress is similar to the scale of the pressure response. Changes in pressure, friction and momentum are important components of the momentum budget.

An important conclusion of Samelson et al. (2006) is that in the vertically averaged momentum boundary layer budget the stress convergence becomes τ_s/H and cannot drive the near-surface acceleration. For the zonal layer-averaged momentum budget, we find a balance between the stress convergence, the pressure gradient force, zonal advection and coriolis force (Figs. 4.7 – 4.10). The pattern of layer-averaged stress convergence and pressure gradient force are similar (Fig. 4.7 and Fig. 4.8) which indicates that the layer-averaged pressure is the driving force on this scale. We have also shown that the pressure gradient force can be estimated by the gradient of the perturbation potential temperature (Eqn. 4.3), which in turn can be related, as we shall see in Chapter 5, to the SST perturbation by a simplified thermodynamic energy equation. The layer-averaged equations are approximately linear and may be relatively easy to solve and interpret. We present such an analysis in Chapter 5.

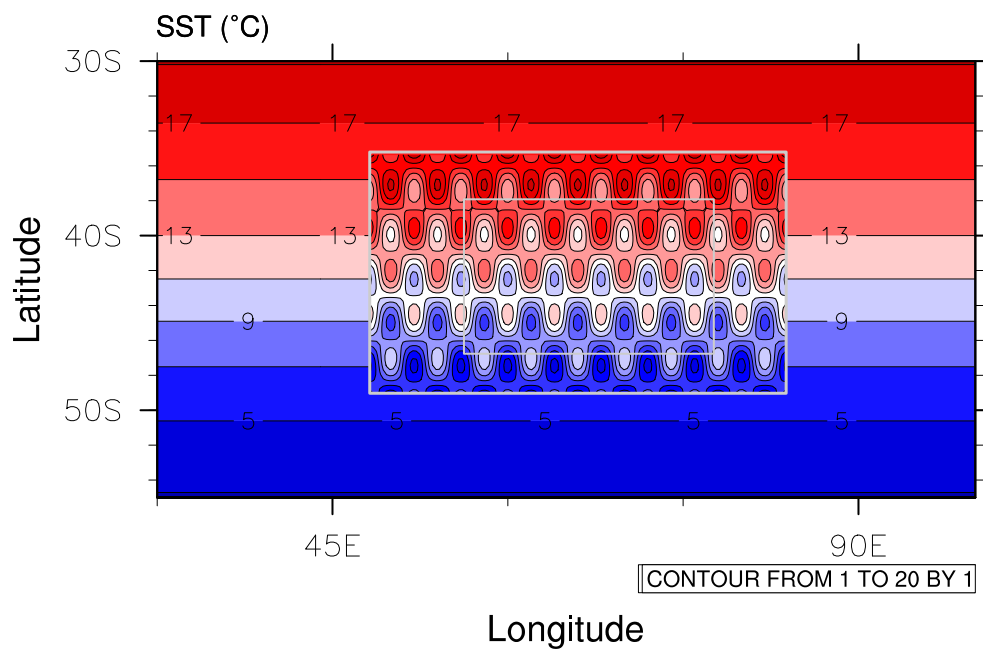


FIGURE 4.1. Maps of background SST in the region of the Agulhas return current. Shaded SST is shown in 2°C contour intervals. Gray rectangles denote the boundaries of the 2 nested WRF domains. Contour interval for the WRF domains is 1°C, outside contour interval 2°C

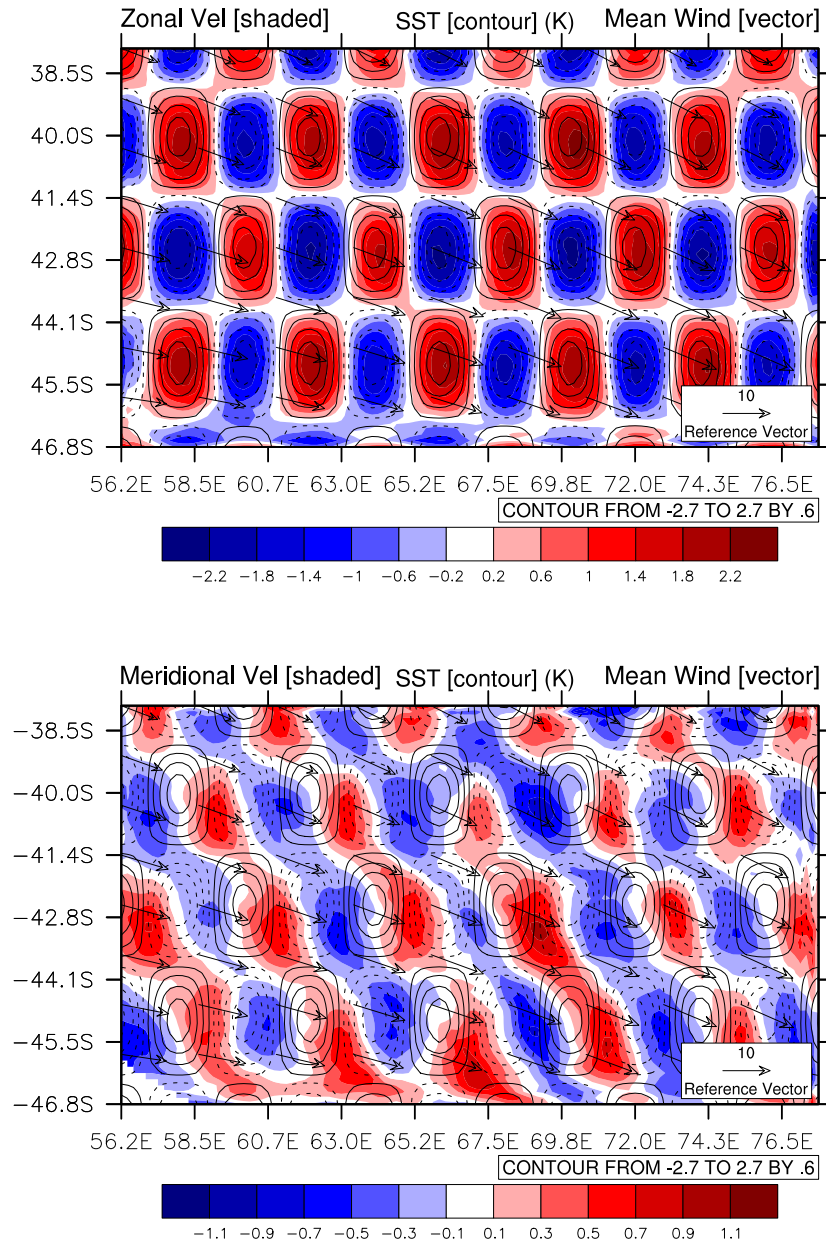


FIGURE 4.2. Map of near-surface zonal (top) and meridional (bottom) wind speed perturbations with SST contour and mean wind speed vector overlay.

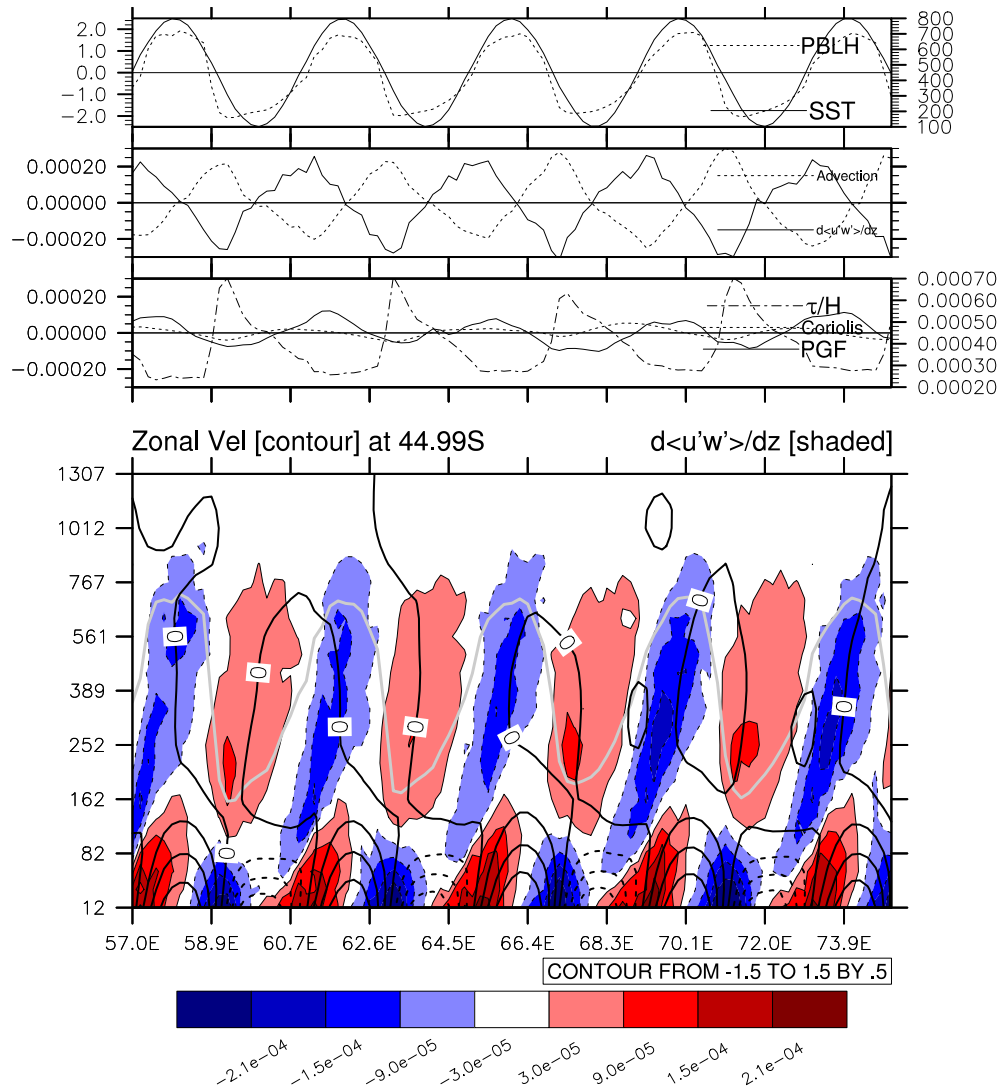


FIGURE 4.3. Composites of boundary layer variables as function of longitude: SST perturbation and boundary layer depth (top panel) near the location of maximum boundary layer depth variation. Perturbation of advection and turbulent stress convergence (second panel). Ratio of perturbation surface stress and boundary layer depth (“ τ/H ”), Coriolis force (“Coriolis”) and pressure gradient force (“PGF”) (third panel). Longitude-height cross section (bottom panel) of meridional turbulent stress convergence (shaded) with zonal velocity (black) and boundary layer depth (gray) contours overlaid.

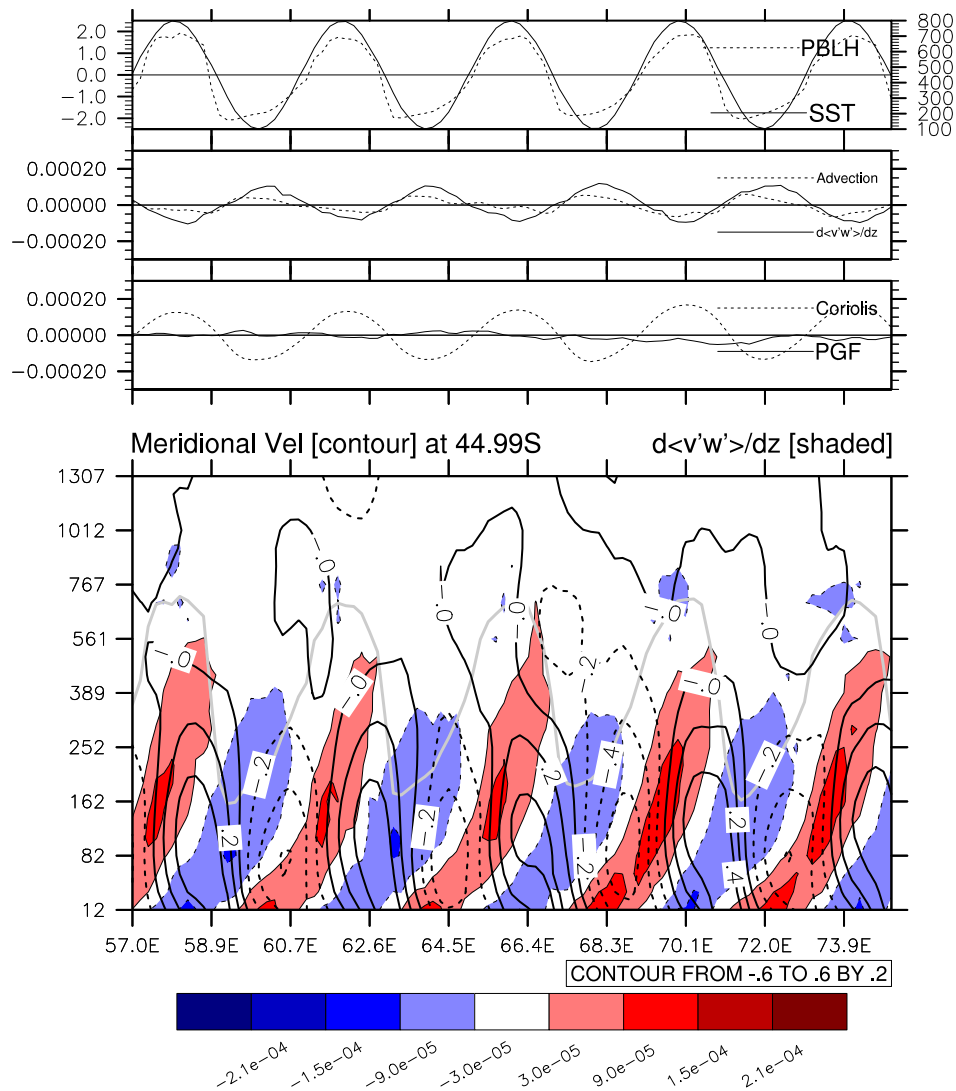


FIGURE 4.4. Composites of boundary layer variables as function of longitude: SST perturbation and boundary layer depth (top panel) near the location of maximum boundary layer depth variation. Perturbation of advection and turbulent stress convergence (second panel). Coriolis force (“Coriolis”) and pressure gradient force (“PGF”) (third panel). Longitude-height cross section (bottom panel) of meridional turbulent stress convergence (shaded) with meridional velocity (black) and boundary layer depth (gray) contours overlaid.

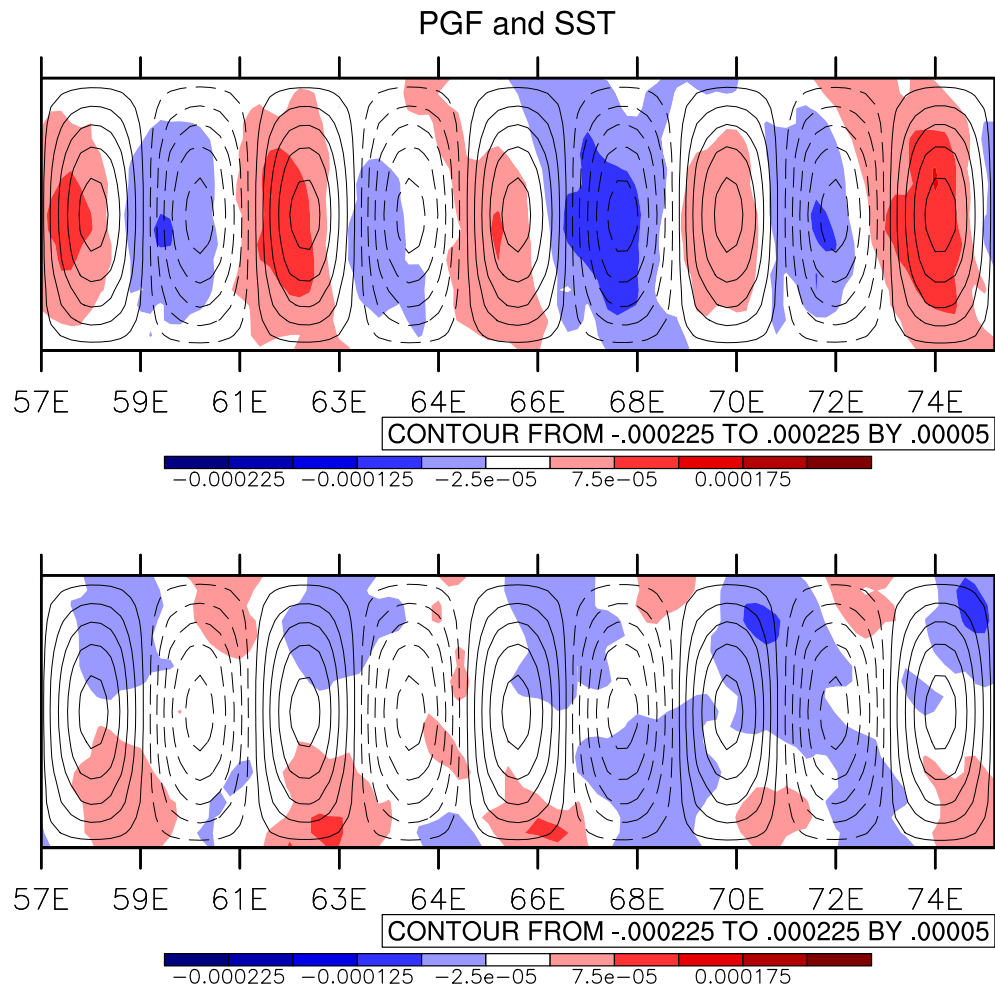


FIGURE 4.5. Composites of surface pressure gradient force and SST. Top panel shows zonal and bottom panel meridional maps of shaded “PGF” and contour SST overlaid. Zero contour lines are omitted for clarity.

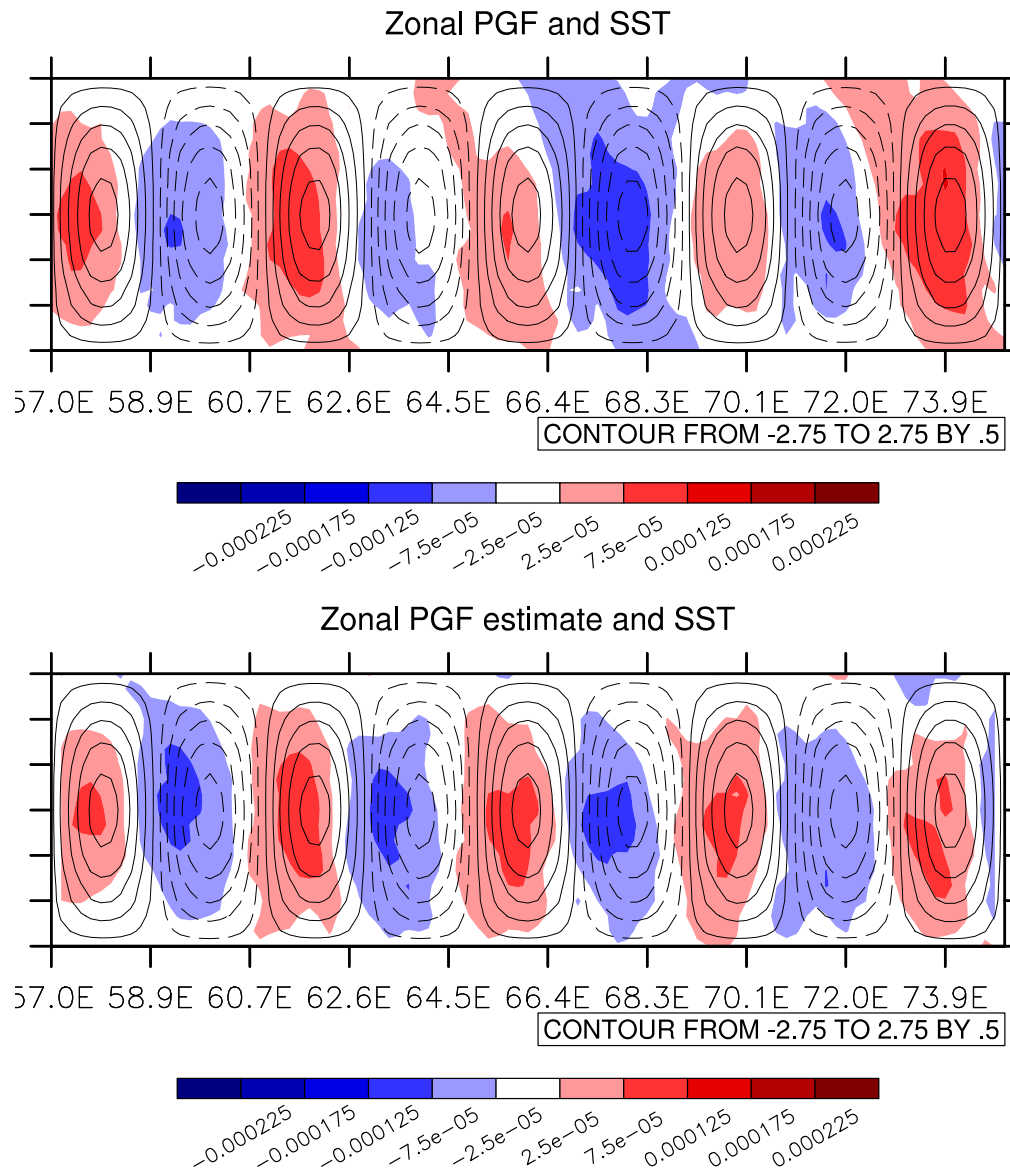


FIGURE 4.6. Composites of surface pressure gradient force and SST. Top panel shows modeled PGF from the WRF simulation and bottom panel PGF estimates based on the horizontal change of potential temperature θ (Eqn. 4.3). Contours of SST are overlaid. Zero contour lines are omitted for clarity.

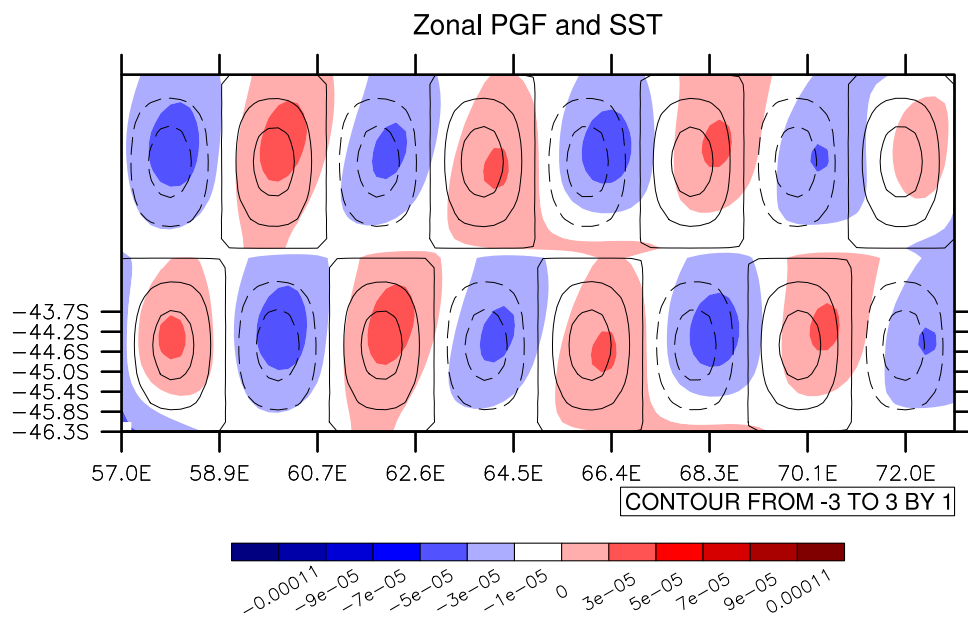


FIGURE 4.7. Boundary layer integral of zonal PGF and SST. The composite of the top row is identical to the bottom row shifted by one-half wavelength to show the spatial structure. Note that some additional smoothing has been applied to remove very high wavenumber noise of unknown origin.

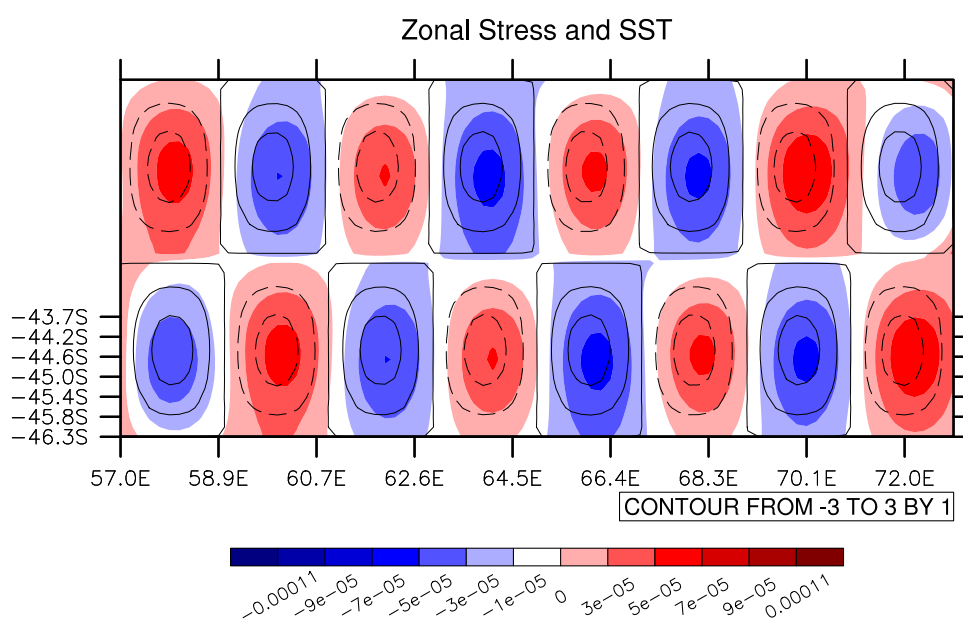


FIGURE 4.8. As in (Fig. 4.7, except for the zonal stress.

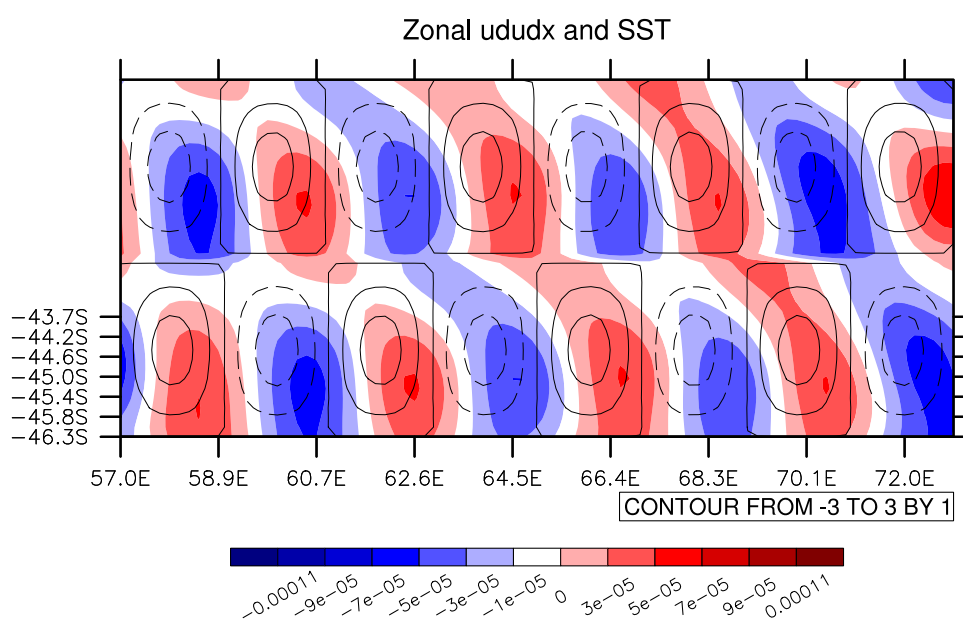


FIGURE 4.9. As in (Fig. 4.7, except for the zonal advection.

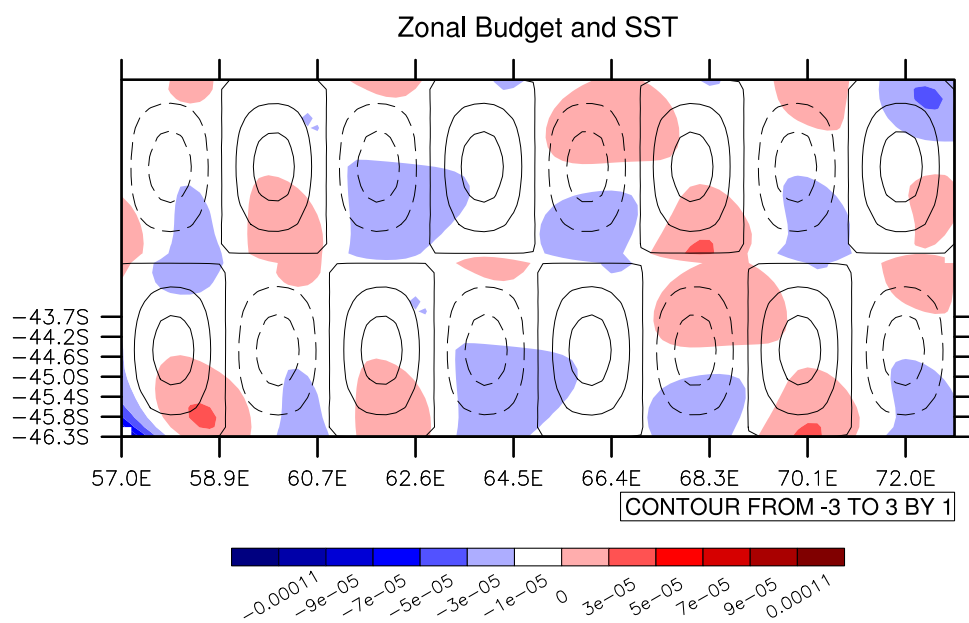


FIGURE 4.10. As in (Fig. 4.7, except for the zonal momentum budget.

5. A LINEAR DIAGNOSTIC MODEL OF ABL RESPONSE TO MESOSCALE SST ANOMALIES

We now return to the central question of this thesis: What are the mechanisms responsible for the satellite-observed coupling between the surface wind stress and SST anomalies with spatial scales of hundreds of kilometers? In Chapters 3 and 4 we have seen that vertical momentum exchange within the boundary layer plays an important role in determining the internal structure of the boundary layer. As pointed out by Samelson et al. (2006), however, these internal mechanisms can obscure the true nature of the coupling at the surface, where integral constraints must be satisfied over the entire boundary layer.

5.1. A Linearized ABL-averaged diagnostic model

The results from Chapter 4 suggest that the vertically integrated response of the ABL flow to SST anomalies may be represented by a simple linearized 1-layer diagnostic model for perturbations of a purely zonal mean flow. A linearized model allows us to provide an analytical expression for the surface wind speed perturbations in terms of the SST perturbation.

The vertically integrated heat and momentum budgets are well represented by:

$$U \frac{\partial}{\partial x} \theta = \frac{C_\theta U_o}{H} (\theta_{\text{sfc}} - \theta_o) \quad (5.1)$$

$$U \frac{\partial}{\partial x} u = -\frac{1}{\rho_{oo}} \frac{\partial}{\partial x} p - \tau_{x,o}/H + fv \quad (5.2)$$

$$U \frac{\partial}{\partial x} v = -\frac{1}{\rho_{oo}} \frac{\partial}{\partial y} p - \tau_{y,o}/H - fu \quad (5.3)$$

In Eqns. 5.1 – 5.3, U represents the vertically integrated mean zonal wind speed, u , v , p and θ represent vertically integrated perturbation quantities for wind, pressure

and potential temperature. Subscripts “o” refer to surface ABL quantities, while θ_{sfc} is the SST anomaly. Note that the perturbation wind does not enter the heat budget since $C_\theta |u_o| \overline{\Delta\theta} \ll C_\theta U_o \theta_{\text{sfc}}$. H is the depth of the vertical integration, which is assumed to be a constant level of zero stress.

The perturbation of θ can be related to the pressure gradient by vertically integrating the hydrostatic equation to the height H where, in addition to being the level of zero stress, we assume that the perturbation of the potential temperature vanishes. This thermal boundary layer height H_θ is different from the momentum BL height H in previous chapters. However, we assume that the two definitions can be used interchangeably here because the numerical values are similar. The surface pressure gradient then becomes:

$$-\frac{1}{\rho_{oo}} \nabla p_{\text{sfc}} = g \frac{H_\theta}{\theta_{oo}} \nabla \theta \quad (5.4)$$

The analysis of the WRF-model suggests a simple linear decrease of the perturbation pressure gradient with increasing height (compare Fig. 5.1). It is then possible to relate Eqn. 5.4 to the vertically integrated perturbation pressure gradient:

$$-\frac{1}{H_\theta} \frac{1}{\rho_{oo}} \int_0^{H_\theta} \nabla p \, dz = -\frac{1}{H_\theta} \frac{1}{\rho_{oo}} \frac{H_\theta}{2} \nabla p_{\text{sfc}} \quad (5.5)$$

$$= \frac{g}{2} \frac{H_\theta}{\theta_{oo}} \nabla \theta \quad (5.6)$$

$$= \frac{\Gamma}{2} \nabla \theta \quad (5.7)$$

Next, we replace the pressure gradient in Eqns. 5.2–5.3 with the ABL averaged potential temperature gradient (Eqn. 5.7) and apply a simple drag law for the surface stress, namely:

$$\tau_{x,o} = C_d U_o u_{\text{sfc}} = C_d U_o r_u u \quad (5.8)$$

$$\tau_{y,o} = C_d U_o v_{\text{sfc}} = C_d U_o r_v v \quad (5.9)$$

The coefficients $r_{u,v}$ represent a simple form of the shape function that relates surface wind speed to the ABL-average velocity components. The choice of different values for the ratio between surface velocity and ABL-average velocity is justified by the analysis of the WRF-model run in Chapter 4 where it was found that the zonal ratio is several times larger than the meridional (Fig. 5.4) surface to ABL-average velocity. This difference is related to differences in vertical shear between the zonal and the meridional wind components (Figs. 4.3, 4.4). The surface potential temperature θ_o is related to the vertically averaged θ by:

$$\theta_o = r_\theta \theta \quad (5.10)$$

The resulting three equations provide a complete set that can be solved analytically for the three unknowns u , v and θ :

$$U \frac{\partial}{\partial x} \theta = \frac{C_\theta U_o}{H_\theta} (\theta_{\text{sfc}} - r_\theta \theta) \quad (5.11)$$

$$U \frac{\partial}{\partial x} u = \frac{\Gamma}{2} \frac{\partial}{\partial x} \theta - C_d U_o r_u u / H_\theta + f v \quad (5.12)$$

$$U \frac{\partial}{\partial x} v = \frac{\Gamma}{2} \frac{\partial}{\partial y} \theta - C_d U_o r_v v / H_\theta - f u \quad (5.13)$$

Note that the thermodynamic equation (Eqn. 5.11) is uncoupled from the momentum equations (Eqns. 5.12 – 5.13). In other words, the feedback between the heat flux and the perturbation wind is of secondary importance on the spatial and temporal scales of interest in this study. Since the thermodynamic equation (Eqn. 5.11) is uncoupled, the vertically averaged potential temperature θ (and hence the pressure perturbation) can be obtained independently of the momentum equations.

The exact analytical solutions of Eqns. 5.11–5.13 were obtained with the help of Mathematica (see APPENDIX B). The solution for the homogeneous part of the zonal and meridional momentum equation (Eqn. 5.12 and Eqn. 5.13)

involves two unknown integration “constants”. The inhomogeneous part is solved by the technique known as variation of constants. The exact solution is provided in Appendix B but it is instructive to obtain the polarization equation for the system of equations. We assume a standard wave-like perturbation in the form of:

$$\theta = \tilde{\theta} \cdot e^{i(kx+ly)} \quad (5.14)$$

$$u = \tilde{u} \cdot e^{i(kx+ly)} \quad (5.15)$$

$$v = \tilde{v} \cdot e^{i(kx+ly)} \quad (5.16)$$

and prescribe the SST perturbation as:

$$\theta_{\text{sfc}} = \tilde{\theta}_{\text{sfc}} \cdot e^{i(kx+ly)} \quad (5.17)$$

The substitution of θ in Eqn. 5.11 with its wave form (Eqn. 5.14) can easily be solved to yield the phase and gain relations between the potential temperature amplitude $\tilde{\theta}$ and the amplitude of the SST perturbation $\tilde{\theta}_{\text{sfc}}$. With the shorthand notation of the inverse adjustment length scale:

$$a = \frac{C_\theta U_o}{H_\theta \cdot U} \quad (5.18)$$

the thermodynamic equation is rewritten as:

$$\tilde{\theta} = \frac{a}{r_\theta a + ik} \cdot \tilde{\theta}_{\text{sfc}} \quad (5.19)$$

and the phase φ_θ and gain A_θ can be calculated to yield the polarization relation for the thermodynamic equation:

$$\varphi_\theta = \tan^{-1}\left(-\frac{k}{r_\theta a}\right) \quad (5.20)$$

$$A_\theta = \frac{a}{\sqrt{r_\theta^2 a^2 + k^2}}. \quad (5.21)$$

The polarization relation between and ABL air potential temperature amplitude $\tilde{\theta}$ and SST $\tilde{\theta}_{\text{sfc}}$ becomes:

$$\tilde{\theta} = \frac{a}{\sqrt{r_{\theta}^2 a^2 + k^2}} \cdot e^{\tan^{-1}(-k/r_{\theta}a)} \tilde{\theta}_{\text{sfc}} \quad (5.22)$$

The lack of a meridional derivative in Eqn. 5.11 indicates that the phase shift φ_{θ} is purely zonal. The pattern of ABL potential temperature θ is therefore shifted to the east relative to the pattern of SST by temperature advection, but remains phase-locked with the SST perturbation in the meridional direction.

The values of the parameters are given in Tbl. 5.1. All parameters except C_{θ} , U_o and H_{θ} are determined by the model design: The horizontal scales k and l and the SST perturbation θ_{sfc} are estimated from satellite observations, f and g are physical constants. The vertical ratios $r_{(u,v,\theta)}$ are determined from the WRF simulation. The climatological zonal mean wind of about 10 m/s determines the drag coefficient C_d .

The values for C_{θ} , U_o and H_{θ} allowed more latitude for their specification within physically reasonable limits. All three variables appear in Eqn. 5.11 and therefore affect the amplitude and the phase of the perturbation air temperature and hence the pressure. Fairly large heat exchange coefficient C_{θ} and surface wind speed U_o are necessary to simulate reasonably large pressure gradients. The ABL depth H also influences magnitude of the pressure gradients. Moreover, H_{θ} determines the phase shift of the surface wind to the SST perturbation, since H_{θ} also appears in the momentum equations. The sensitivity of the model is nearly linear in U_o and C_{θ} in terms of the magnitude of the wind components for a range of values of $\pm 50\%$ of the optimal value. The phase relation remains nearly unchanged. Varying the ABL depth H_{θ} has a lesser affect on wind speed magnitude than on the phase relation. Increasing H_{θ} shifts the zonal wind downwind

while decreasing the depth centers the zonal wind perturbation over the SST perturbation. The model seems robust over a wide range of values and it appears that the stratification can influence the phase relation between wind and SST perturbations.

Using the values from Tbl. 5.1, the numerical values for the zonal phase $\varphi_{\theta,x}$, meridional phase $\varphi_{\theta,y}$ and gain A_θ are:

$$\varphi_{\theta,x} = -79.6^\circ \quad (5.23)$$

$$\varphi_{\theta,y} = 0.^\circ \quad (5.24)$$

$$A_\theta = 0.18 \quad (5.25)$$

The ABL-averaged potential temperature perturbation is less than 20 % of the SST perturbation. The thermodynamic adjustment length scale $1/a$ is much larger than the length scale of the SST anomalies π/k . In other words, the time the air spends over the anomaly is too short for air temperature to fully adjust. Therefore the sensible heat flux is roughly in phase with the SST anomaly. The heating associated with the SST perturbation is distributed over the depth of the thermodynamic boundary layer H_θ . Therefore, even small potential temperature perturbations can have significant pressure gradients.

Since the potential temperature and its zonal gradient are in quadrature, and $\varphi_{\theta,x} = -79.6$, the zonal potential temperature gradient is approximately in phase with the patterns of SST; the meridional temperature gradient, however, is 90° out of phase with SST.

Pressure and air temperature are in phase. The zonal phase of the zonal pressure gradient $\varphi_{\frac{\partial p}{\partial x},x}$ and the meridional phase of the zonal pressure gradient $\varphi_{\frac{\partial p}{\partial x},y}$ are consequently almost zero relative to the pattern of SST:

$$\varphi_{\frac{\partial p}{\partial x},x} = 10.4^\circ \quad (5.26)$$

$$\varphi_{\frac{\partial p}{\partial x},y} = 0.^\circ \quad (5.27)$$

The meridional gradient operator introduces a 90° phase shift to the meridional pressure gradient (Eqn. 5.13). The meridional pressure gradient is therefore shifted 90° to the north relative to the pattern of θ while it is in phase with θ in the zonal direction. Numerically the phases are estimated to be:

$$\varphi_{\frac{\partial p}{\partial y},x} = -79.6^\circ \quad (5.28)$$

$$\varphi_{\frac{\partial p}{\partial y},y} = 90.^\circ \quad (5.29)$$

The amplitudes of the zonal and meridional pressure gradients are:

$$A_{\frac{\partial p}{\partial x}} = 4.1 \cdot 10^{-5} \text{ ms}^{-2}/\text{K} \quad (5.30)$$

$$A_{\frac{\partial p}{\partial y}} = 2.2 \cdot 10^{-5} \text{ ms}^{-2}/\text{K} \quad (5.31)$$

The polarization relations between ABL velocities and SST are estimated from the exact solution (see APPENDIX B). The numerical estimate for the zonal and meridional phase ($\varphi_{u,x}$ and $\varphi_{u,y}$, respectively) and gain A_u relative to the SST perturbations are:

$$\varphi_{u,x} = -23.6^\circ \quad (5.32)$$

$$\varphi_{u,y} = 5.9^\circ \quad (5.33)$$

$$A_u = 0.113 \text{ ms}^{-1}/\text{K} \quad (5.34)$$

For the meridional velocity, the phases $\varphi_{v,(x,y)}$ and gain A_v are estimated to be:

$$\varphi_{v,x} = -141.6^\circ \quad (5.35)$$

$$\varphi_{v,y} = 81.4^\circ \quad (5.36)$$

$$A_v = 0.095 \text{ ms}^{-1}/\text{K} \quad (5.37)$$

5.2. Discussion

The comparisons between the 1-layer model surface wind fields and the WRF surface wind fields in Figs. 5.2 – 5.3 demonstrate the ability of the 1-layer model to capture the important features of the WRF simulation. The 1-layer model zonal velocity (Fig. 5.2) shows an identical eastward and small southward shift relative to the SST and the magnitude of surface wind perturbation is well simulated. The meridional velocity perturbations in the WRF-model form continuous anomaly bands with a northwest-southeast orientation. The tendency for the northwest-southeast banding on the scale of the SST anomalies is present in the 1-layer model as well, but the bands are less developed (Fig. 5.3). The response of the surface meridional wind is shifted a bit further north in the WRF-model run, which is likely related to the neglect of the meridional advection term in the 1-layer model and nonlinear stress effects.

The coupling between the surface wind stress and SST perturbations is controlled by the pressure gradient force, and the primary dynamical balance is between the pressure gradient force and the surface drag. The linearized zonal advection of momentum $U \frac{\partial}{\partial x} u$ and $U \frac{\partial}{\partial x} v$ is responsible for the eastward shift of the velocities relative to the pattern of SST. The Coriolis force plays a minor role in the adjustment, but is responsible for the small meridional phase shift of the zonal velocity $\varphi_{u,y}$ of 5.9° . The large zonal phase shift of the meridional velocity $\varphi_{v,x}$ of 141.6° can be explained by considering the smaller gain of the meridional pressure gradient $A_{\frac{\partial p}{\partial y}}$ of $2.2 \cdot 10^{-5} \text{ms}^{-2}/\text{K}$ compared to the gain of the zonal pressure gradient, which is almost twice as large (Eqns. 5.30 and 5.31). The meridional pressure gradient is therefore unable to balance the surface drag alone and the phase shift from momentum advection becomes more pronounced.

Within the 1-layer model framework, the difference in coupling coefficients between divergence and curl of the surface wind as a function of down and cross-wind SST gradient can be explained by investigating the terms of the divergence and vorticity budget. The vertically integrated budgets are readily derived from Eqns. 5.12 – 5.13. As previously shown, the coefficient for the divergence-SST coupling is close to twice as large as the coefficient for the curl-SST coupling. The divergence budget is:

$$U \frac{\partial}{\partial x} (\nabla \cdot \mathbf{v}) = \frac{\Gamma}{2} \nabla^2 \theta - \frac{C_d U_o}{H_\theta} \left(r_u \frac{\partial u}{\partial x} + r_v \frac{\partial v}{\partial y} \right) + f \zeta \quad (5.38)$$

$$\text{where } \zeta = \frac{\partial v}{\partial x} - \frac{\partial u}{\partial y} \text{ is the vorticity} \quad (5.39)$$

The largest term is the Laplacian of the pressure term (first term on the RHS, equivalent to the Laplacian of the temperature). The pressure term is balanced by the divergence of surface drag (second term on the RHS) and by the advection of divergence (the LHS). The last term in Eqn. 5.38 is much smaller and can be neglected. The vorticity budget is:

$$U \frac{\partial}{\partial x} \zeta = \frac{C_d U_o}{H_\theta} \left(r_v \frac{\partial v}{\partial x} - r_u \frac{\partial u}{\partial y} \right) + f (\nabla \cdot \mathbf{v}) \quad (5.40)$$

The pressure term vanishes in the vorticity budget and the only remaining forcing term is the divergence term (last term RHS), which is much smaller than the pressure term in the divergence budget. The divergence in the vorticity budget (Eqn. 5.40) is balanced by the advection of vorticity and the curl of surface drag. All terms in the vorticity equation are much smaller than the leading terms in the divergence equation. The pattern of surface divergence from the 1-layer solution is shown in Fig. 5.5 and the pattern of the surface vorticity is shown in Fig. 5.6. The two figures show that divergence is several times larger than vorticity and that the pattern of divergence and vorticity are in quadrature to the pattern of SST. The magnitudes and locations are in good agreement with the WRF simulations.

The difference between the zonal and the meridional ratio of surface to ABL-average wind is important for the location of the vorticity relative to the pattern of SST. This can be illustrated by assuming identical ratios ($r_u = r_v = r$) and by rewriting the vorticity equation as

$$U \frac{\partial}{\partial x} \zeta = \frac{C_d U_o r}{H_\theta} \zeta + f(\nabla \cdot \mathbf{v}) \quad (5.41)$$

In this form, the first term on the RHS provides only a damping to the solution while the LHS shifts the vorticity zonally. The vorticity should therefore be damped and zonally shifted relative to the divergence pattern. However, observations show that the vorticity is located in quadrature to the pattern of divergence. The meridional shift that moves the pattern into quadrature is due to the term $-r_u \frac{\partial u}{\partial y}$ in Eqn. 5.40. The vertical structure of the ABL wind perturbations, as represented by the ABL-average wind ratios for the zonal (r_u) and meridional (r_v) direction, is therefore crucial for explaining the observed curl of the surface wind. The good agreement between the 1-layer model and the WRF simulation can be summarized by the scatter plots that quantify the relation between surface wind curl and divergence as a function of SST gradient and by comparing the coupling coefficients (see Eqns. 2.34 – 2.35) to previous results (e.g. Chelton et al. 2004, O'Neill 2003 and 2005). The coupling coefficients for the divergence and curl as functions of downwind and crosswind SST gradients (Fig. 5.7) are similar to the results from Chapter 1. The amplitudes (Fig. 5.8) of the divergence and curl as functions of the angle between components of downwind and crosswind SST gradient are larger than in the WRF simulation, but the tendency that the amplitude of the divergence is about two times larger than the curl amplitude remains. The coupling coefficient for the divergence as a function of downwind SST gradient can be directly estimated from the gain in the polarization relation (Eqn. 5.34).

Since the zonal velocity amplitude is larger than the amplitude of the meridional velocity, and because the zonal wave lengths are smaller than the meridional we can approximate the divergence by the gradient of the zonal velocity. Ignoring the phase shift (Eqns. 5.32 – 5.33), the polarization relation for the zonal surface velocity can be written:

$$\tilde{u}_{\text{sfc}} = r_u \cdot A_u \text{ SST} \quad (5.42)$$

$$(5.43)$$

The differentiation is approximated by a finite difference Δx :

$$\frac{\Delta \tilde{u}_{\text{sfc}}}{\Delta x} = 6. \cdot 0.113 \frac{\Delta \text{SST}}{\Delta x} \quad (5.44)$$

$$\frac{\Delta \tilde{u}_{\text{sfc}}}{\Delta x} = 0.678 \frac{\Delta \text{SST}}{\Delta x} \quad (5.45)$$

The value of 0.678 is identical to the coupling coefficient obtained from the binned scatter plots (Fig. 5.7).

Although pressure perturbations are the driving force in this adjustment process, the simple 1-layer model has shown that the vertical structure of the wind response, which is expressed here in simple surface/ABL-ratio, is very important. The vertical shear allows the generation of larger vorticity than with vertical uniform wind and is responsible for shifting the vorticity over the regions with large crosswind SST gradients.

The vertical structure is only crudely represented in this 1-layer model and does not explain the differences in the vertical structure of the downwind and crosswind wind perturbation components. The 1-layer model may also be inadequate for investigating the scale dependent response of the surface stress to SST anomalies in the vicinity of SST fronts. This will require the inclusion of mixing and adjustment processes similar to the ones described in Chapter 3, and is left for future work.

Parameter:	Value:	Sensitivity
k	$2 \cdot \pi / 289 \text{ km}^{-1}$	n/a
l	$2 \cdot \pi / 532 \text{ km}^{-1}$	n/a
f	$-5 \times 10^{-5} \text{ s}^{-1}$	n/a
g	9.81 ms^{-2}	n/a
θ_{\circ}	280 K	n/a
θ_{sfc}	2.5 K	n/a
U	10 ms^{-1}	n/a
C_d	1.4×10^{-3}	n/a
r_u	6	n/a
r_v	2	n/a
r_{θ}	2	n/a
C_{θ}	2.5×10^{-3}	large, effects PGF
U_{\circ}	4 ms^{-1}	moderate, effects PGF
H_{θ}	500 m	small, phase shift

TABLE 5.1. Parameters for the 1-layer linear perturbation model. The first 11 parameters were pre-determined by the experimental design and physics. The last three values represent model parameters with a range of physically correct values (see text for details). For these three values the optimal value within the physical range were chosen. The sensitivity of the model is indicated and the influence effect is given.

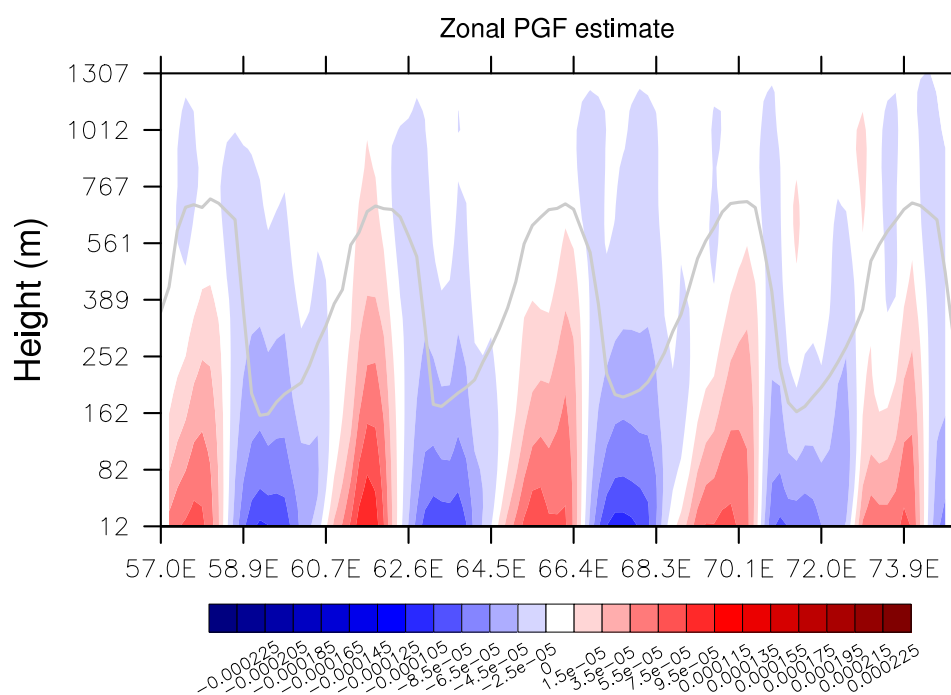


FIGURE 5.1. Latitude-height cross section of estimated pressure gradient force with ABL depth (bottom panel) and SST (top panel). Estimate of “PGF” is shaded with contour of ABL depth (gray) as overlay.

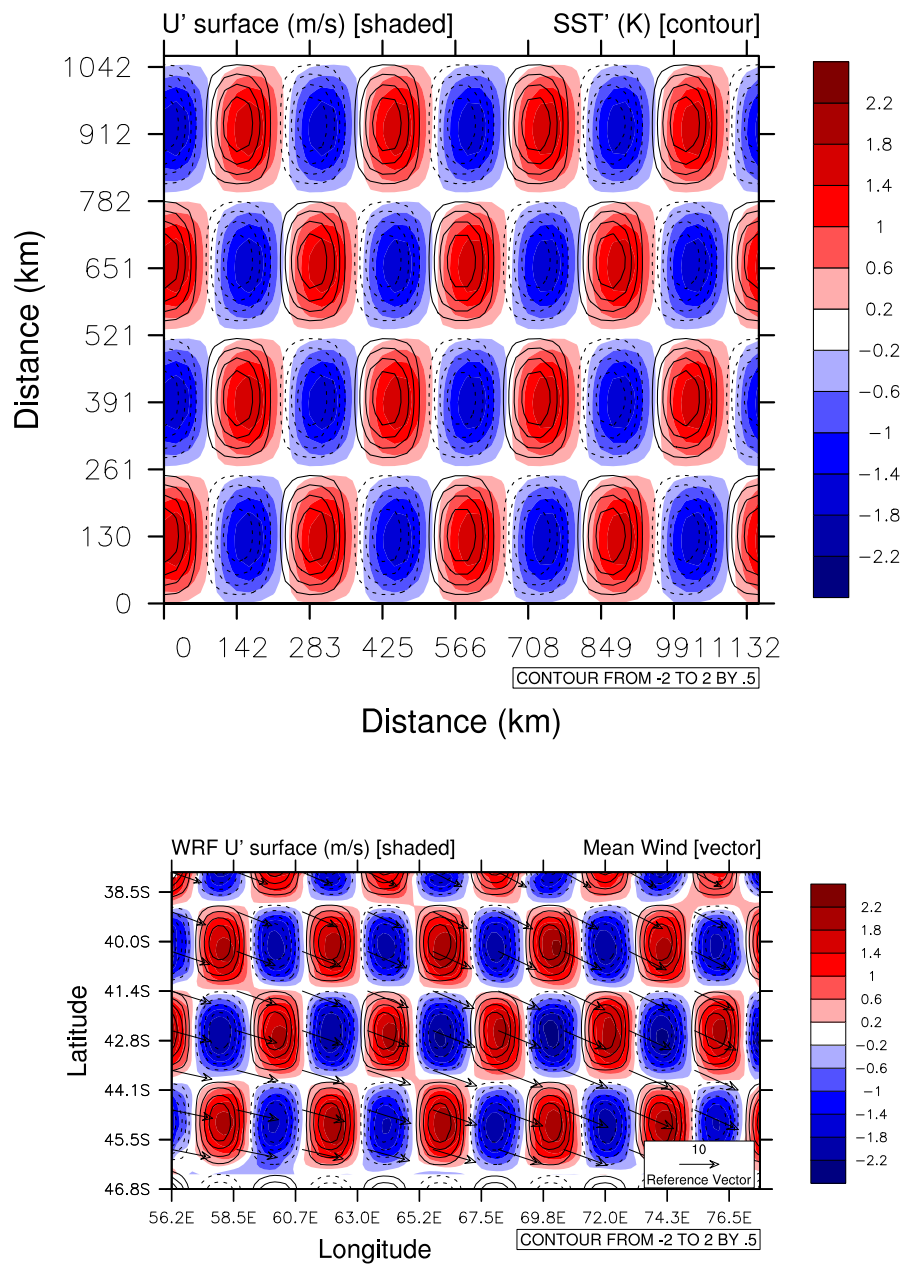


FIGURE 5.2. Map of 1-layer diagnostic model zonal velocity (top) and WRF-model averaged zonal surface velocity (repeated for comparison, bottom). SST contours are shown as overlays with contour interval of $.5^{\circ}\text{C}$. Zero contour of SST is omitted for clarity.

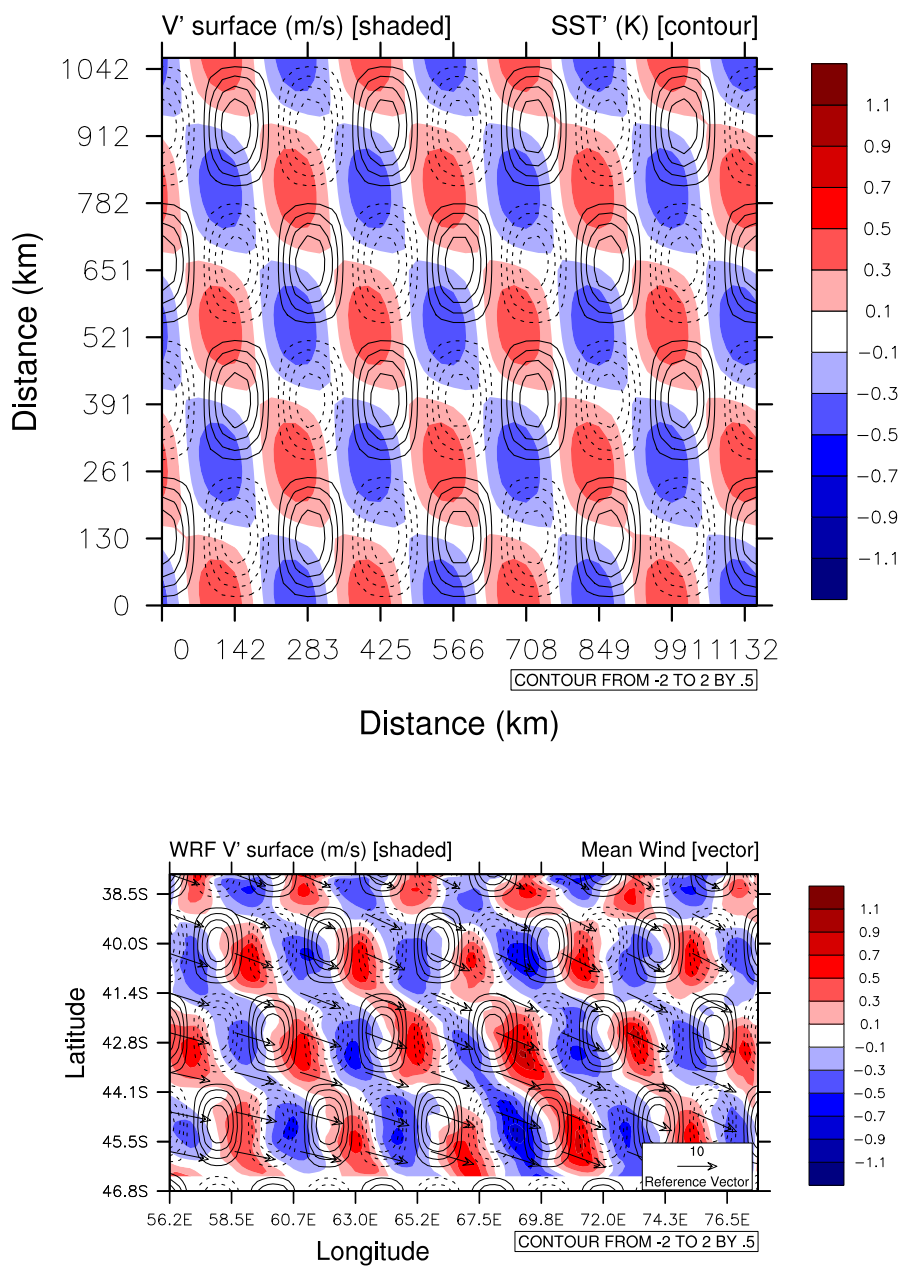


FIGURE 5.3. Map of 1-layer diagnostic model meridional velocity (top) and WRF-model averaged meridional surface velocity (repeated for comparison, bottom). SST contours are shown as overlays with contour interval of $.5^{\circ}\text{C}$. Zero contour of SST is omitted for clarity.

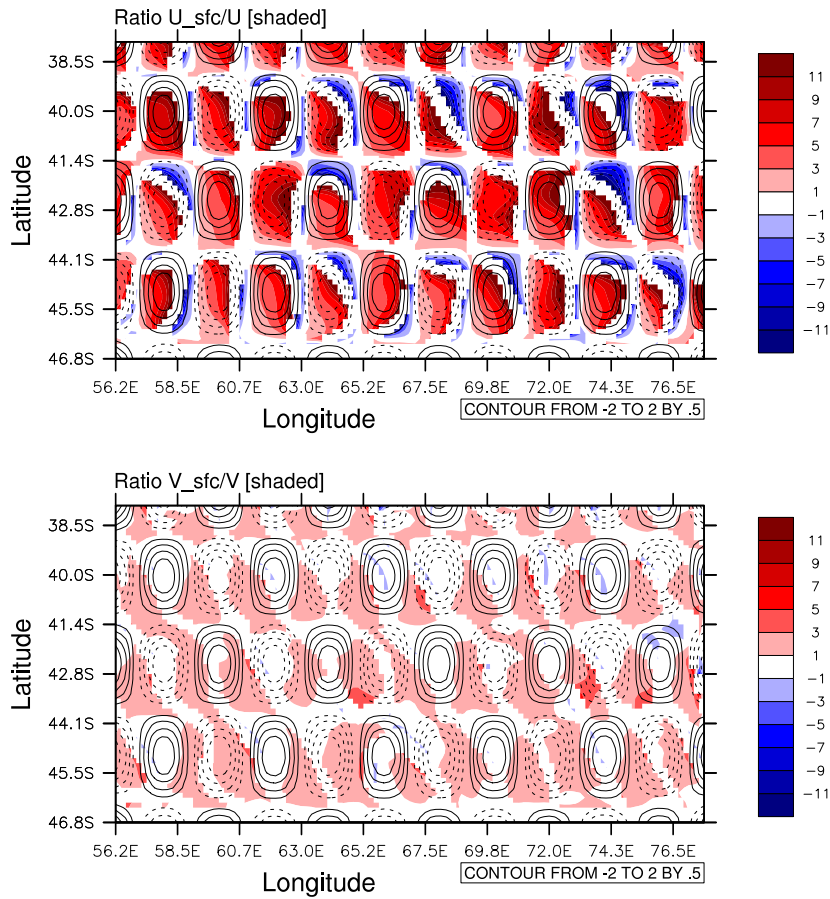


FIGURE 5.4. Map of surface to vertically integrated meridional velocity ratio derived from WRF-model simulation. Top panel shows zonal velocity ratio, bottom panel shows meridional velocity ratio. Locations with vertically integrated velocities of less than 0.05 m/s have been masked. SST contours are shown as overlays with contour interval of .5°C. Positive values of SST is shown as solid and negative SST as dashed contours, the zero contour of SST is omitted for clarity.

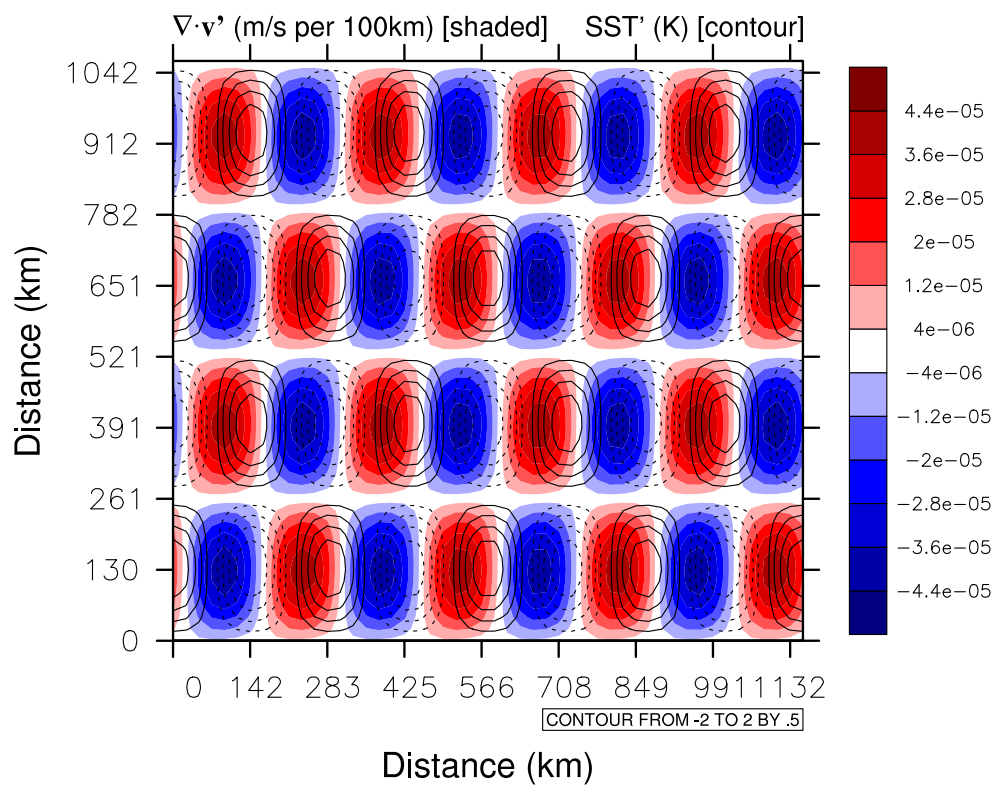


FIGURE 5.5. Map of 1-layer diagnostic model divergence and SST perturbations.

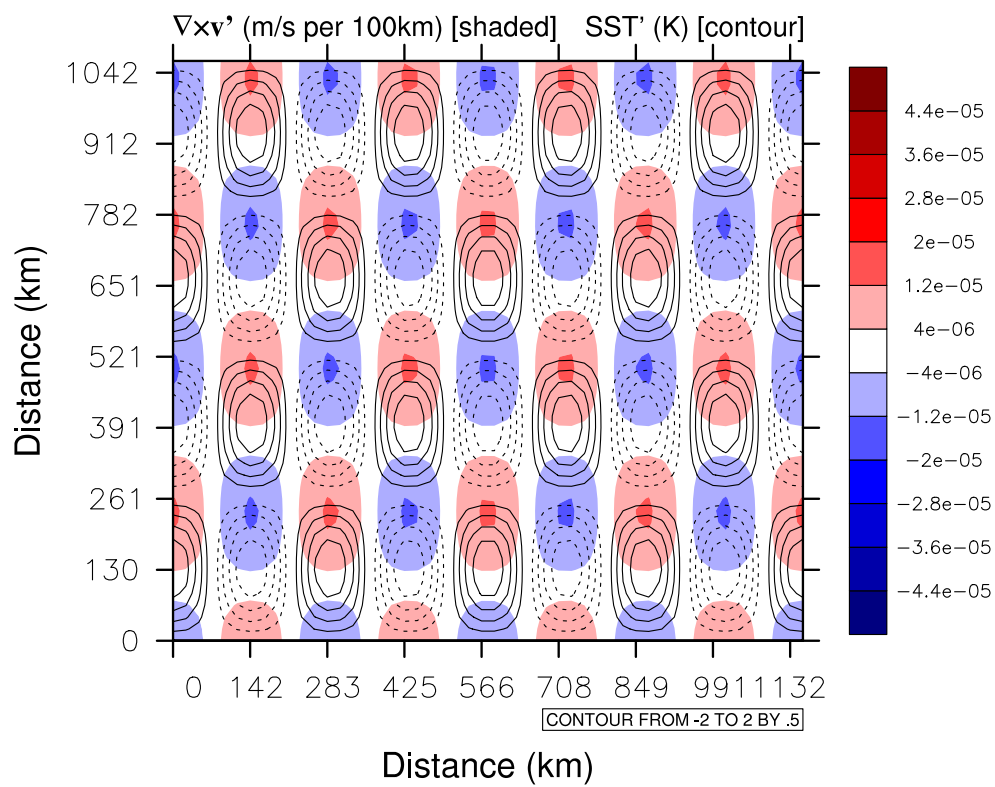


FIGURE 5.6. Map of 1-layer diagnostic model curl and SST perturbations.

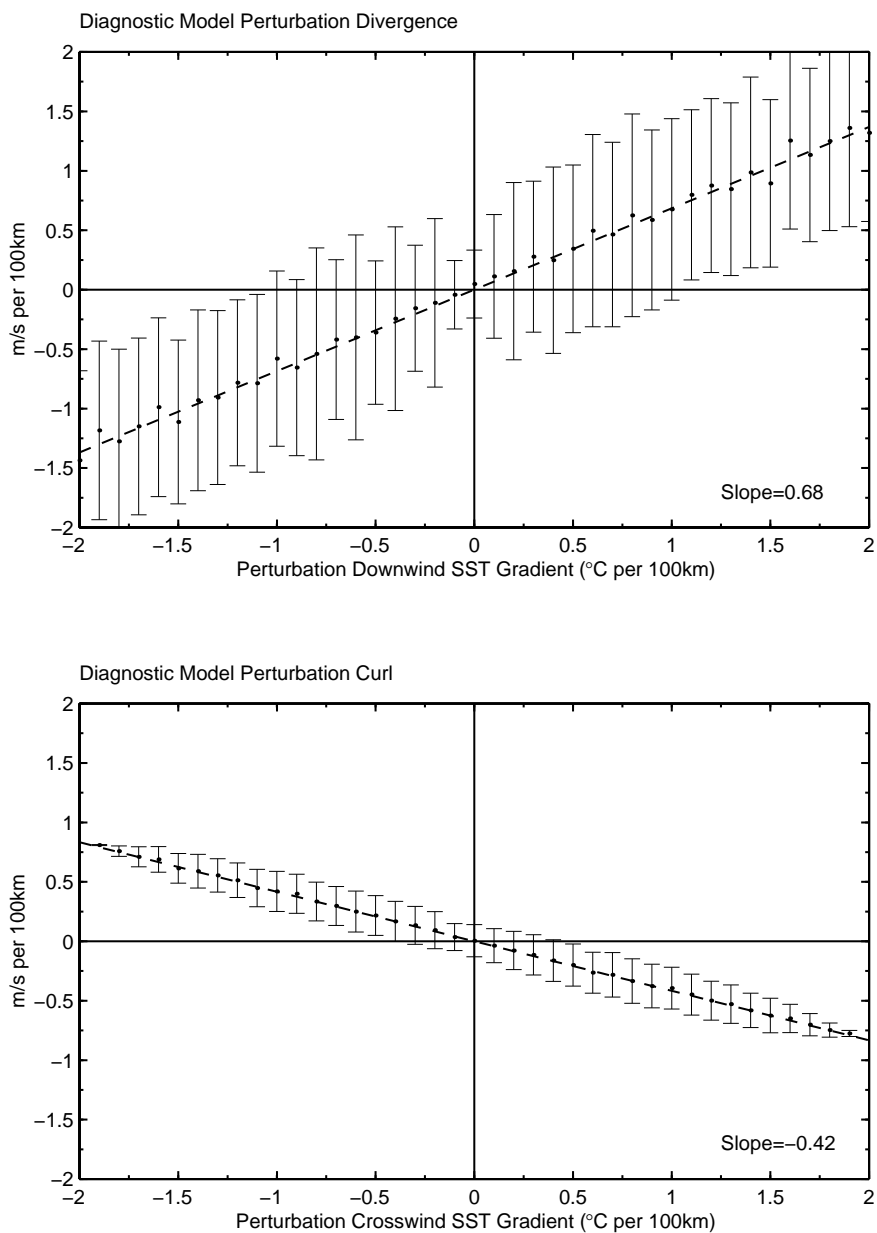


FIGURE 5.7. Binned scatterplots of the relationships between the SST and wind velocity fields calculated from the diagnostic solution of the 1-layer model. Top panel shows perturbation wind divergence as a function of downwind SST gradient and bottom panel shows perturbation wind curl plotted as a function of crosswind SST gradient.

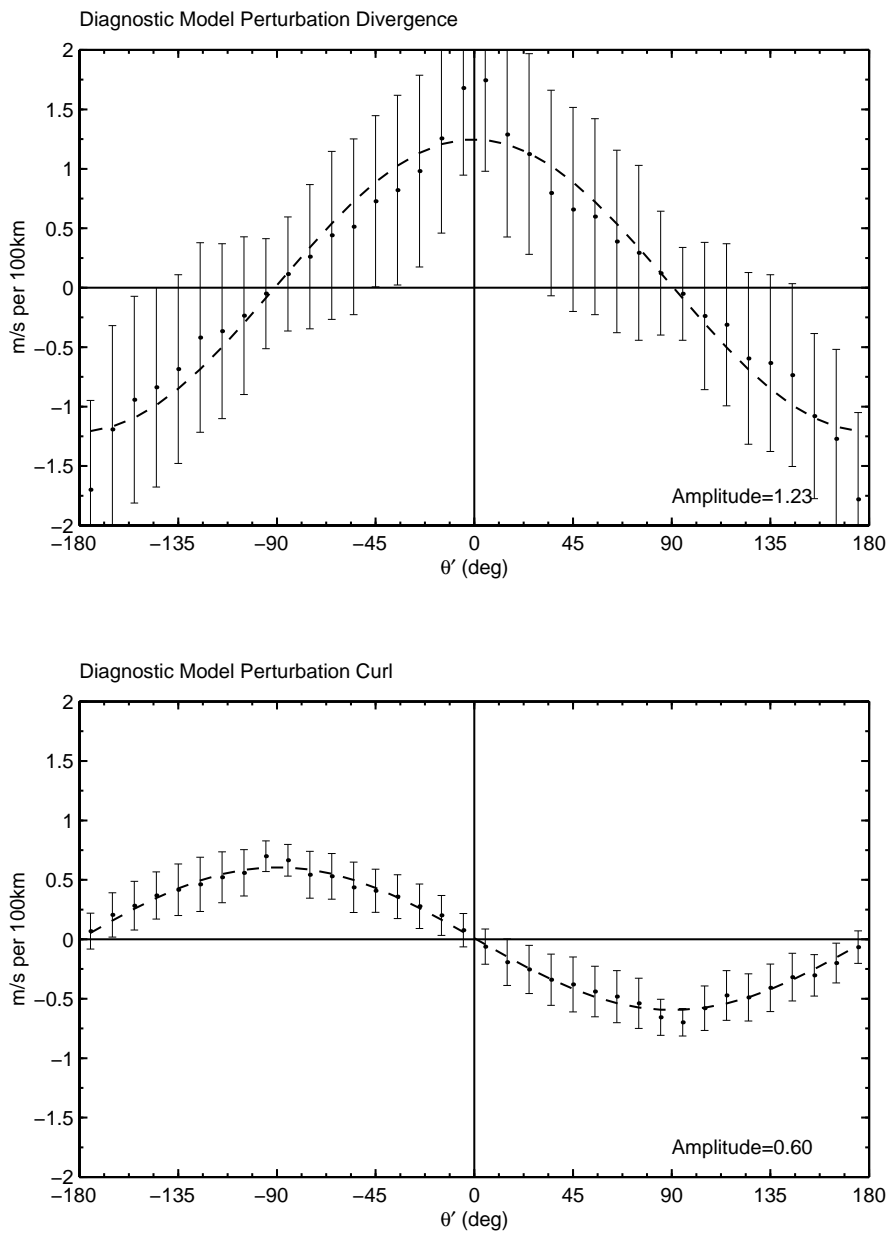


FIGURE 5.8. Binned scatterplots of the angular relationships between the wind and the SST field. Top panel shows perturbation wind divergence as a function of the angle between down and crosswind SST gradient and bottom panel shows perturbation wind curl plotted as a function of the angle between down and crosswind SST gradient.

6. SUMMARY

This thesis has examined the mechanisms that couple the monthly-averaged atmospheric boundary layer (ABL) to sea surface temperature (SST) perturbations over the open ocean on scales of 50-500 km. Numerical and analytical methods were used to simulate and analyze the response of the surface wind to SST perturbations. Numerical experiments were performed with the Weather Research and Forecasting (WRF) mesoscale model to simulate the ABL response to realistic and idealized SST anomalies. Detailed analysis of the simulated momentum budgets lead to the development of a 1-layer diagnostic analytical model that successfully predicts the observed relationship between surface wind and SST anomalies in the Agulhas return current region. The analytical model provides increased understanding of the mechanisms of atmosphere-ocean coupling.

The first numerical experiment established the ability of the WRF model to accurately simulate the surface wind response revealed by QuikSCAT satellite observations over the Agulhas return current. We found that the WRF model successfully simulates the observed correspondence between higher surface winds and positive SST anomalies and between lower surface winds and negative SST anomalies. The comparison with observations was further quantified by computing the coupling coefficients between the surface divergence and surface curl in terms of the downwind and crosswind SST gradients, respectively, and also by the phase and amplitudes of the sinusoidal response of the surface divergence and surface curl as a function of the counterclockwise angle between the downwind and crosswind SST gradients. With the exception of the amplitude of the surface divergence as a function of the counterclockwise angle, the quantitative agreement between the WRF simulations and observations is very good.

Next, a pair of WRF numerical experiments focused on the response of the atmospheric boundary layer to idealized SST fronts. Two independent model runs were performed: (1) a cold-to-warm SST front integration (P4), and (2) a warm-to-cold front integration (M4). The acceleration of the surface wind in P4 and deceleration in M4, were found over a narrow transition zone co-located with the narrow region of largest SST changes. Horizontal momentum is redistributed vertically in the ABL by turbulence and convection in the transition zone, while largest pressure adjustments take place over a much broader region downstream from the SST front. In the cold-to-warm transition (P4), WRF simulates an unstable, growing thermal internal boundary layer (TIBL) in the lower part of the ABL. As the TIBL grows, higher velocity air aloft is incorporated into the TIBL. In the warm-to-cold case (M4), the momentum boundary layer collapses over the transition zone, and vertical mixing of momentum by turbulence and convection ceases in the upper part of the ABL. We conclude that high vertical resolution is required to represent the important ABL adjustment mechanisms associated with SST fronts *within* the ABL.

The final WRF experiment simulated the atmospheric response to idealized mesoscale SST anomalies arranged in a checkerboard pattern over the southern middle latitudes. The alternating positive and negative SST anomalies are assumed to have spatial scales similar to those observed in the Agulhas region. The horizontal scale of the ABL pressure response was found to be similar to the scale of the SST perturbation itself and the horizontal pressure gradient force plays an important role in the vertically integrated horizontal momentum budget. Temperature advection by the mean wind shifts the perturbation pressure gradient over the SST anomalies and a balance is found between the pressure gradient and the perturbation stress convergence of the momentum boundary layer.

Analysis of the vertically integrated momentum budgets from the WRF simulations showed that the ABL response to the Agulhas mesoscale SST anomalies was found to be approximately linear. A linear diagnostic model therefore was developed and analyzed that improves our understanding of the mechanisms coupling the surface wind to the SST anomalies. The analytical model successfully predicts the observed phase and amplitude of the ABL wind, pressure and temperature response to the SST anomalies, with largest quantitative discrepancies found in the perturbation wind component perpendicular to the mean wind direction. By using the divergence and vorticity budgets, the diagnostic model shows how the difference of vertical shear between the cross and downwind wind component might explain the differences in the coupling coefficients between the divergence and curl as functions of downwind and crosswind SST gradients.

BIBLIOGRAPHY

- [1] Angevine, W. M., 2001: Observation of the morning transition of the convective boundary layer, *Bound.-Layer Meteor.*, **101**, 209–227.
- [2] Bretherton, C. S., J. R. McCaa, and H. Grenier, 2004: A new Parameterization for Shallow Cumulus Convection and its Application to Marine Subtropical Cloud-Topped Boundary Layers. Part I: Description and 1D Results, *Mon. Wea. Rev.*, **132**, 864–882.
- [3] Chelton, D. B., and coauthors, 2001: Observations of coupling between surface wind stress and sea surface temperature in the eastern tropical Pacific, *J. Climate*, **14**, 1479–1498.
- [4] Chelton, D. B., and F. J. Wentz, 2005: Global satellite observations of sea surface temperature for numerical weather prediction and climate research. *Bull. Amer. Meteor. Soc.*, **86**, 1097–1115.
- [5] Chelton, D. B., and M. H. Freilich, 2005: Scatterometer-based assessment of 10-m wind analyses from the operational ECMWF and NCEP numerical weather prediction models, *Mon. Wea. Rev.*, **133**, 409–429.
- [6] Cleveland, W. S., and S. J. Devlin, 1988: Locally weighted regression: An approach to regression analysis by local fitting, *J. Amer. Stat. Assoc.*, **83**, 596–610.
- [7] Cronin, M. F., S.-P. Xie, and H. Hashizume, 2003: Barometric Pressure Variations Associated with Eastern Pacific Tropical Instability Waves, *J. Climate*, **16**, 3050–3057.
- [8] Deser, C. , 1993: Diagnosis of the Surface Momentum Balance over the Tropical Pacific Ocean, *J. Climate*, **6**, 64–74.
- [9] de Szoeke, S. P., and C. S. Bretherton, 2004: Quasi-Lagrangian Large Eddy Simulation of Cross-Equatorial Flow in the East Pacific Atmospheric Boundary Layer, *J. Atmos. Sci.*, **61**, 1837–1858
- [10] de Szoeke, S. P., and coauthors, 2005: EPIC 95° W Observations of the Eastern Pacific Atmospheric Boundary Layer from the Cold Tongue to the ITCZ, *J. Atmos. Sci.*, **62**, 426–442.
- [11] Friehe, C. A., and coauthors, 1991: Air-sea fluxes and surface layer turbulence around a sea surface temperature front, *J. Geophys. Res.*, **96**, 8593–8609.

- [12] Grenier, H., and C. S. Bretherton, 2001: A Moist PBL Parameterization for Large-Scale Model and Its Application to Subtropical Cloud-Topped Marine Boundary Layers, *Mon. Wea. Rev.*, **129**, 357–377.
- [13] Hafner, J., and S.-P. Xie, 2003: Far-Field Simulation of the Hawaiian Wake: Sea Surface Temperature and Orographic Effects, *J. Climate***60**, 3021–3032.
- [14] Hashizume, H., and coauthors, 2002: Direct Observations of Atmospheric Boundary Layer Response to SST Variations associated with Tropical Instability Waves over the Eastern Equatorial Pacific, *J. Climate*, **15**, 3379–3393.
- [15] Kain J. S. and J. M. Fritsch, 1990: A One-Dimensional Entraining/Detraining Plume Model and Its Application in Convective Parameterization, *J. Atmos. Sci.*, **47**, 2784–2802.
- [16] Kain J. S., 2004: The KainFritsch Convective Parameterization: An Update. *J. of Applied Meteorology*, **43**, 1701–181.
- [17] Lacis, A. A., and J. E. Hansen, 1974: A parameterization for the absorption of solar radiation in the earth’s atmosphere, *J. Climate*, **31**, 118–133.
- [18] Mahrt, L. J., 1972: A Numerical Study of the Influence of Advective Accelerations in an Idealized, Low-Latitude, Planetary Boundary Layer, *J. Atmos. Sci.*, **29**, 1477–1484.
- [19] Mahrt, L., D. Vickers, E. Moore, 2004: Flow Adjustments Across Sea-Surface Temperature Changes, *Bound.-Layer Meteor.*, **111**, 553–564.
- [20] McCaa, J. R., 2001: A new parameterization of marine stratocumulus and shallow clouds for climate models. Ph.D. dissertation, University of Washington, 161 pp.
- [21] McCaa, J. R., Bretherton C. S., 2004: A new parameterization for shallow cumulus convection and its application to marine subtropical cloud-Topped boundary layers. Part II: Regional simulations of marine boundary layer clouds. *Mon. Wea. Rev.*, **132**, 883–896.
- [22] Mlawer, E. J., S. J. Taubman, P. D. Brown, M. J. Iacono, 1997: Radiative transfer for inhomogeneous atmospheres: RRTM, a validated correlated-k model for the longwave, *Geophys. Res. Lett.*, **102**, 16663–16682.
- [23] O’Neill, and coauthors, 2003: Observations of SST-induced perturbations of the wind stress field over the Southern Ocean on seasonal timescales, *J. Climate*, **16**, 2340–2354.

- [24] O'Neill, and coauthors, 2005: Hight-resolution satellite observations of SST modification of the marine atmospheric boundary layer over the Agulhas Return Current, *J. Climate*, **VV**, pp-pp.
- [25] Nilsson, J , 2000: Propagation, Diffusion, and Decay of SST Anomalies beneath an Advective Atmosphere *J. Phys. Oceanogr.***30**, 1505–1513.
- [26] Park, K.-A., and P. C. Cornillon, 2002: Stability-induced modification of Sea Surface Winds over Gulf Stream Rings, *Geophys. Res. Lett.*, **29**, 2211, doi:10.1029/2001GL014236.
- [27] Raymond, D. J., and coauthors, 2004: EPIC2001 and the Coupled OceanAtmosphere System of the Tropical East Pacific Bulletin of the American Meteorological Society **85**, 1341–1354.
- [28] Samelson, R. M., and coauthors, 2006: On the Coupling of Wind Stress and Sea Surface Temperature, *J. Climate*, **19**, 1557–1566.
- [29] Schlax, M. G., D. B. Chelton, and M. H. Freilich, 2001: Sampling errors in wind fields constructed from singel and tandem scatterometer datasets, *J. Atmos. Oceanic Technol.*, **18**, 1014–1036.
- [30] Skamarock, W. C., J. B. Klemp, J. Dudhia, D. O. Gill, D. M. Barker, W. Wang and J. G. Powers, 2005: A Description of the Advanced Research WRF Version 2, available at http://wrf-model.org/wrfadmin/docs/arw_v2.pdf
- [31] Small, J. R., S.-P. Xie, Y. Wang, S. K. Esbensen, and D. Vickers, 2004: Numerical simulation of boundary layer structure and cross-equatorial flow in the eastern Pacific, *J. Climate*, **62**, 1812–1830.
- [32] Stevens, B., J. Duan, J. C. McWilliams, M. Münich, and J. D. Neelin, 2001: Entrainment, Rayleigh Friction, and boundary Layer Winds over the Tropical Pacific, *J. Climate*, **15**, 30–44.
- [33] Sweet, W. R., and coauthors, 1981: Ocean-atmosphere interaction effects in the lower troposphere across the north wall of the Gulf Stream, *Mon. Wea. Rev.*, **109**, 1042–1052.
- [34] Thum, N., and coauthors, 2002: Air Sea Heat Exchange along the Northern Sea Surface Temperature Front in the Eastern Tropical Pacific, *J. Climate*, **15**, 3361–3378.
- [35] Tomas, R. A., J. R. Holton, P. J. Webster, 1999: The influence of cross-equatorial pressure gradients on the location of near-equatorial convection, *Quart. J. Roy. Meteor. Soc.*, **556**, 1107–1127.

- [36] Wallace, J. M., T. P. Mitchell, and C. Deser, 1989: The influence of sea surface temperature on surface wind in the eastern equatorial Pacific: Seasonal and interannual variability, *J. Climate*, **2**, 1492–1499.
- [37] Wang, W., D. Barker, C. Bruyère, J. Dudhia, D. Gill, and J. Michalakes, 2004: WRF Version 2 modeling system users guide, available at http://box.mmm.ucar.edu/wrf/users/docs/user_guide/ARWUsersGuide.pdf
- [38] Wicker, L. J., and W. C. Skamarock, 2002: Time splitting methods for elastic models using forward time schemes, *Mon. Wea. Rev.*, **130**, 2088–2097.
- [39] Xie, S. P., and coauthors, 1998: Coupled ocean-atmospheric waves on the equatorial front. *Geophys. Res. Lett.*, **25**, 3863–3866.

APPENDICES

APPENDIX A. WRF-model η -levels and nominal heights

- η :

1.0000 0.9967 0.9932 0.9896 0.9858 0.9820 0.9779 0.9738 0.9694 0.9649 0.9603
 0.9554 0.9504 0.9452 0.9398 0.9342 0.9284 0.9224 0.9161 0.9096 0.9029 0.8959
 0.8886 0.8811 0.8733 0.8652 0.8568 0.8481 0.8391 0.8297 0.8200 0.8099 0.7994
 0.7886 0.7773 0.7656 0.7535 0.7409 0.7279 0.7143 0.7003 0.6857 0.6706 0.6549
 0.6386 0.6217 0.6042 0.5860 0.5672 0.5476 0.5273 0.5063 0.4845 0.4618 0.4383
 0.4139 0.3886 0.3624 0.3351 0.3069 0.2776 0.2472 0.2157 0.1829 0.1490 0.1138
 0.0772 0.0393 0.0000

- Heights in m

12.00 34.66 57.36 82.11 107.59 134.14 161.76 190.46 220.59 251.48 283.83
 317.60 352.52 388.94 426.85 466.27 507.23 550.08 594.86 641.23 689.58 740.28
 793.02 847.83 905.11 964.90 1027.24 1092.20 1160.18 1231.25 1305.49 1383.32
 1464.46 1549.37 1638.54 1731.68 1829.29 1931.51 2038.88 2151.56 2269.7
 2394.00 2524.58 2662.14 2806.97 2959.36 3120.10 3289.58 3468.71 3658.46
 3858.93 4071.27 4297.24 4537.74 4793.81 5067.17 5359.21 5672.74 6009.72
 6372.49 6765.15 7191.25 7656.76 8167.61 8731.80 9362.85 10076.89 10900.07

APPENDIX B. Solution to the Diagnostic Model Appendix

$$\varphi_\theta = -\frac{k}{ar_\theta} \quad (\text{A.1})$$

$$A_\theta = \frac{a}{\sqrt{k^2 + a^2 r_\theta^2}} \quad (\text{A.2})$$

$$\varphi_u = \frac{ar_\theta((fHl + C_\circ k r_v)(r_u r_v C_\circ^2 + f^2 H^2) - H^2 k^2(fHl - C_\circ k r_u)U^2) - Hk^2 U(H^2 U^2 l^3 - f^2 H^2 k + C_\circ^2 r_v^2 k + C_\circ fHl(r_u + r_v))}{k(f^3 l H^3 + f^2 k(C_\circ r_v - aHr_\theta U)H^2 + fl(r_u r_v C_\circ^2 + aHr_\theta(r_u + r_v)UC_\circ - H^2 k^2 U^2)H + k(C_\circ r_u + aHr_\theta U)(C_\circ^2 r_v^2 + H^2 k^2 U^2))} \quad (\text{A.3})$$

$$A_u = aH\Gamma \left(\frac{H^2 U^2 k^4 + (fHl + C_\circ k r_v)^2}{(k^2 + a^2 r_\theta^2)(H^4 k^4 U^4 - H^2 k^2(2f^2 H^2 - C_\circ^2(r_u^2 + r_v^2))U^2 + (r_u r_v C_\circ^2 + f^2 H^2)^2)} \right)^{1/2} \quad (\text{A.4})$$

$$\varphi_v = \frac{HU(k^2 l U^2 H^2 - f^2 l H^2 - C_\circ f k(r_u + r_v)H + C_\circ^2 l r_u^2)k^2 + ar_\theta((fHk - C_\circ l r_u)(r_u r_v C_\circ^2 + f^2 H^2) - H^2 k^2(fHk + C_\circ l r_v)U^2)}{k(f^3 k H^3 + f^2 l(aHr_\theta U - C_\circ r_u)H^2 + f k(r_u r_v C_\circ^2 + aHr_\theta(r_u + r_v)UC_\circ - H^2 k^2 U^2)H - l(C_\circ r_v + aHr_\theta U)(C_\circ^2 r_u^2 + H^2 k^2 U^2))} \quad (\text{A.5})$$

$$A_v = aH\Gamma \left(\frac{H^2 k^2 l^2 U^2 + (fHk - C_\circ l r_u)^2}{(k^2 + a^2 r_\theta^2)(H^4 k^4 U^4 - H^2 k^2(2f^2 H^2 - C_\circ^2(r_u^2 + r_v^2))U^2 + (r_u r_v C_\circ^2 + f^2 H^2)^2)} \right)^{1/2} \quad (\text{A.6})$$

$$(\text{A.7})$$

$$\theta(x, y) = \frac{a\tilde{\theta}_{\text{sf}}(ar_{\theta} \cos(kx) + k \sin(kx)) \sin(ly)}{k^2 + a^2 r_{\theta}^2} \quad (\text{A.8})$$

$$\begin{aligned} u(x, y) = & \left[aH\tilde{\theta}_{\text{sf}}\Gamma(fHl \cos(ly)) ((ar_{\theta}(r_u r_v C_{\circ}^2 + H^2(f - kU)(f + kU)) - C_{\circ}Hk^2(r_u + r_v)U) \cos(kx) \right. \\ & + k(r_u r_v C_{\circ}^2 + H(aC_{\circ}r_{\theta}(r_u + r_v)U + H(f - kU)(f + kU))) \sin(kx)) \\ & + k(k(r_u r_v^2 C_{\circ}^3 + aHr_{\theta}r_v^2 U C_{\circ}^2 + H^2(r_v f^2 + k^2 r_u U^2) C_{\circ} + aH^3 r_{\theta} U(k^2 U^2 - f^2)) \cos(kx) \\ & - (aC_{\circ}r_{\theta}(k^2 r_u U^2 H^2 + f^2 r_v H^2 + C_{\circ}^2 r_u r_v^2) - Hk^2 U((k^2 U^2 - f^2) H^2 + C_{\circ}^2 r_v^2)) \sin(kx)) \sin(ly)) \Big] / \\ & \left[(k^2 + a^2 r_{\theta}^2) \left(H^4 k^4 U^4 - H^2 k^2 (2f^2 H^2 - C_{\circ}^2 (r_u^2 + r_v^2)) U^2 + (r_u r_v C_{\circ}^2 + f^2 H^2)^2 \right) \right] \end{aligned} \quad (\text{A.9})$$

$$\begin{aligned} v(x, y) = & \left[aH\tilde{\theta}_{\text{sf}}\Gamma(l \cos(ly)) ((aC_{\circ}r_{\theta}(k^2 r_v U^2 H^2 + f^2 r_u H^2 + C_{\circ}^2 r_u^2 r_v) - Hk^2 U((k^2 U^2 - f^2) H^2 + C_{\circ}^2 r_u^2)) \cos(kx) \right. \\ & + k(r_u^2 r_v C_{\circ}^3 + aHr_{\theta}r_u^2 U C_{\circ}^2 + H^2(r_u f^2 + k^2 r_v U^2) C_{\circ} + aH^3 r_{\theta} U(k^2 U^2 - f^2)) \sin(kx)) \\ & - fHk(k(r_u r_v C_{\circ}^2 + H(aC_{\circ}r_{\theta}(r_u + r_v)U + H(f - kU)(f + kU))) \cos(kx) \\ & + (C_{\circ}Hk^2(r_u + r_v)U - ar_{\theta}(r_u r_v C_{\circ}^2 + H^2(f - kU)(f + kU)) \sin(kx)) \sin(ly)) \Big] / \\ & \left[(k^2 + a^2 r_{\theta}^2) \left(H^4 k^4 U^4 - H^2 k^2 (2f^2 H^2 - C_{\circ}^2 (r_u^2 + r_v^2)) U^2 + (r_u r_v C_{\circ}^2 + f^2 H^2)^2 \right) \right] \end{aligned} \quad (\text{A.10})$$

